NASA Contractor Report 3432

Influence of Nonequilibrium Radiation and Shape Change on Aerothermal Environment of a Jovian Entry Body

S. N. Tiwari and S. V. Subramanian

NASA

NASA Contractor Report 3432

Influence of Nonequilibrium Radiation and Shape Change on Aerothermal Environment of a Jovian Entry Body

S. N. Tiwari and S. V. Subramanian
Old Dominion University Research Foundation
Norfolk, Virginia

NASA

National Aeronautics
and Space Administration

Scientific and Technical
Information Branch

1981

TABLE OF CONTENTS

LIST OF TABLES

LIST OF FIGURES

LIST OF FIGURES (concluded).

SUMMARY

The influence of nonequilibrium radiative energy transfer and the
effect of probe configuration changes on the flow phenomena around a
Jovian entry body is investigated. The radiating shock-layer flow is
assumed to be axisymmetric, viscous, laminar and in chemical equili-
brium. The radiative transfer equations are derived under nonequili-
brium conditions which include multilevel energy transitions. The
equilibrium radiative transfer analysis is performed with an existing
nongray radiation model which accounts for molecular band, atomic line,
and continuum transitions. The nonequilibrium results are obtained
with and without ablation injection in the shock layer. The nonequi-
librium results are found to be greatly influenced by the temperature
distribution in the shock layer. In the absence of ablative products,
the convective and radiative heating to the entry body are reduced
significantly under nonequilibrium conditions. The influence of
nonequilibrium is found to be greater at higher entry altitudes. With
coupled ablation and carbon phenolic injection, 16 chemical species are
used in the ablation layer for radiation absorption. Equilibrium and
nonequilibrium results are compared under peak heating conditions. For
the study of the probe shape change effects, the initial body shapes
considered are 45-degree sphere cone, 35-degree hyperboloid, and 45-
degree ellipsoid. In all three cases, the results indicate that the
shock-layer flow field and heat transfer to the body are influenced
significantly by the probe shape change. The effect of shape change
on radiative heating of the afterbodies is found to be considerably
larger for the sphere cone and ellipsoid than for the hyperboloid.

INTRODUCTION

During the exploratory missions to the planetary atmospheres, the entry spacecraft is subjected to various flow environments and heating conditions. The type and intensiveness of this heating mainly depends on the atmospheric composition of the planet and the trajectory of the entry vehicle. At hypersonic entry conditions, radiation plays a very important role in the analysis of the flow phenomena around the planetary entry body. The radiative energy transferred to the body from the high-temperature shock-layer gas exceeds the convective and aerodynamic heating rates. The problem of radiative heating of planetary entry bodies has been investigated extensively in the literature (refs. 1 - 4). One such situation where the radiative heating constitutes the major portion of the heat transferred to the probe is the case of Jovian entry heating (refs. 5 - 8). In order to study the composition and structure of Jupiter's atmosphere, the National Aeronautics and Space Administration has scheduled a Jovian mission for a probe space-craft in 1985. At times, the entry velocity of the Jupiter probe is expected to exceed 40 km/sec. The probe has to survive the intense radiative heating during this high-speed entry mission. For this purpose, the probe is normally coated with ablative heat shield materi-als. As the probe advances through the Jovian atmosphere the heat shield ablates and forms a protective layer of cool gases around the probe, and these are mainly responsible for absorbing the incoming radiation. For the Jovian entry probe, it has been estimated that the heat shield weight for thermal protection will be as much as 45 percent of the total weight of the probe. Since experimental facilities cannot adequately simulate the conditions expected during a Jovian entry mission, most of the required information must be obtained from theoretical studies. This is particularly true for investigating the extent of radiative heating to the entry body.

In order to assess the magnitude of radiative heating to the Jovian entry body (and its influence on convective heating and other flow phenomena), it is essential to employ meaningful radiative transport

models in analyzing the shock-layer flow phenomena. In formulating the transfer equations for radiating gases, it is normally assumed that the gas is in local thermodynamic equilibrium (LTE). With this assumption, the transfer equation is simplified significantly as the populations of the various atomic and molecular states are given by the equilibrium (Boltzmann) distribution. For a wide range of conditions encountered in high-speed gas dynamics, the transitions to or from the excited energy states are primarily due to atomic and molecular collisional processes (rather than radiative emission and absorption processes). Under these conditions, the assumption of LTE is usually justified. There are situations, however, where this assumption cannot be justified and conditions of nonlocal thermodynamic equilibrium (NLTE) may exist. In a very strict sense, NLTE corresponds to the conditions where population densities of various energy levels deviate from the equilibrium (Boltzmann) distribution. Quite often it has been speculated that use of an LTE radiative transport model may not be justified in a shock-heated plasma. This is because, for the combined conditions of high velocities, high temperatures and low densities, the probability of a radiative transition becomes comparable with the probability of corresponding collisional transitions (ref. 9). Unless the gas is optically thick, the emission of a photon is a process that is not balanced by its inverse. Consequently, the population distribution among the energy levels departs from that predicted by the Boltzmann equation. Only one transition in one atom, molecule or ion need be unbalanced in this way to invalidate the LTE assumption.

Most analyses available on the NLTE radiative heat transfer are limited to vibrationally excited, infrared active diatomic and triatomic molecules (refs. 10 - 13). This situation is encountered in some engineering and upper atmospheric studies. The radiative processes associated with the Jovian entry conditions, however, correspond to ultraviolet radiation and involve electronic transitions. Furthermore, the shock-layer gas consists of molecules and atoms as well as charged particles. Hence, the studies available on the NLTE radiative heat transfer are not particularly suitable for Jovian entry conditions.

4

One particular study by Horton (ref. 14) estimates the importance of nonequilibrium radiation during a hypersonic entry into Jupiter's atmosphere. It is concluded, in this study, that the NLTE effect depletes the ablation-layer thickness. This leaves the ablative products more transparent, and the absorption of radiation by these species is less than the equilibrium value. As a result, the net radiative heat flux to the probe surface is more under NLTE conditions. Although this conclusion is in general agreement with the kind of behavior expected in an ablation-contaminated, nonequilibrium, boundary-layer flow, the analysis is not complete. It is important to remember that the NLTE phenomenon is among the gas particles themselves rather than between the gas and the radiation field. Thus, essentially no study is available that treats the problem of NLTE radiative transfer under planetary entry conditions in a systematic manner.

Under NLTE, there are more particles in the higher energy levels than normally predicted by the equilibrium theory. This is because the particles take considerably longer time to establish a deexcitation collision in a nonequilibrium field. The overpopulation of the excited energy levels leaves the unexcited levels underpopulated. As a direct consequence of this, the absorption pattern of the particles is not the same as the equilibrium absorption behavior (since a particle in an unexcited state is capable of absorbing more radiation than the one in an excited state). Hence, a more detailed analysis of the absorption cross section of these particles has to be made under both LTE and NLTE conditions. The frequency-dependent absorption coefficient for a non-gray gas analysis may be treated either in detail or by a "step model." There are several methods available in the literature for detailed computation of the equilibrium absorption coefficient (refs. 15 - 17). In a step model, the frequency dependence is broken into a number of discrete steps. Sutton (see Zoby et al., ref. 18) developed a 58-step model for the hydrogen and helium mixture. For this case, a 30-step model developed by Tiwari and Subramanian simplifies the analysis even further, and the results compare well with the other 2 models (ref. 19). In general, the nonequilibrium absorption coefficient is obtained by

multiplying the equilibrium values by a nonequilibrium factor. This factor is a function of the intensity of the incident radiation, collisional relaxation time of the particle under investigation, and the radiative lifetime of the excited state. It is, therefore, important to find an appropriate relation for this nonequilibrium factor for the Jovian entry conditions.

After evaluation of the spectral absorption coefficient, the next step is to develop an appropriate expression for spectral and total radiative heat fluxes. The expression for the total radiative transport involves integration over both the frequency spectrum and the physical space. In general, the problem of radiative exchange is a complex three-dimensional phenomenon. The inclusion of nonequilibrium formulation adds to this complexity with different chemical species at different energy levels. Hence, reasonable assumptions are required in order to obtain meaningful solutions of the transfer equation. In many physically realistic problems, the complexity of the three-dimensional radiative transfer can be reduced by introduction of the "tangent slab approximation." This approximation treats the gas layer as a one-dimensional slab in calculation of the radiative transport. Radiation in directions other than normal to either the body or shock is neglected. The methods for calculating the divergence of the radiative flux and other conservation equations are available in references 20 to 22.

Another problem which arises directly from the radiative heating rates is the effect of shape change and mass loss on the flow field of a Jovian entry body. For exploratory missions to planets such as Mars and Venus, the levels of heating to the entry probe are not severe enough to significantly change the mass and shape of the probe. In contrast, the large radiative heating rates associated with the Jovian entry result in massive ablation of the protective heat shield material as the probe advances through the atmosphere (ref. 23). This, in turn, results in different probe configurations at different stations along the entry trajectory. This change of shape can significantly affect

6

the flow pattern and the heating rate distribution around the probe. Sutton et al. (refs. 24 - 26) have presented an inviscid flow-field analysis for investigating the effects of the recession of the heat shield caused by radiative heating to the Jupiter probe. The initial probe configurations considered were hyperboloids and sphere cones Important studies available on the effects of mass loss, shape change, and real-gas aerodynamics of a Jovian atmospheric probe are discussed in a survey article by Walberg et al. (ref. 27). It is clear from the review of this article that further studies are needed to investigate the effects of the shape changes on heating of the forebody and after-body of different Jovian entry probes.

From the literature survey, it is clear that no work is available which considers the influence of nonlocal thermodynamic equilibrium radiative heating flow phenomena around a Jovian entry body. A few available studies are either inappropriate or provide very little information for nonequilibrium analysis under Jovian entry conditions. The presence of different ablative species further complicates the nonequilibrium analysis. For a correct NLTE analysis, it is essential to consider the various excitation and deexcitation probablities of all important species in the shock layer. It is important to realize that, through an entirely different temperature distribution, the NLTE radiative transfer influences significantly the convective heating rate as well as other flow properties in the shock layer. Since an accurate determination of the total heating rate is essential for the design of the heat shield and for assessing the survival of the entry probe, it is necessary to investigate the extent of NLTE influence on the entire shock-layer flow phenomena in a systematic manner.

The primary objectives of this study, therefore, are twofold: first to investigate the influence of NLTE radiative transfer, and then to determine the effects of changes in the probe configurations on the entire shock-layer flow phenomena. To accomplish this in a systematic manner, the present study is divided into four major areas: (1) significance of radiation models on the flow-field solutions, (2) influence

of NLTE radiation without ablation injection, (3) importance of NLTE radiation with ablation injection, and (4) effect of probe shape change on the flow phenomena.

The basic formulation of the entire problem considered for the present study is given in the section titled "Basic Formulation." Discussions on the radiative transfer equations, radiation absorption models, and radiative flux equations (for both the LTE and NLTE conditions) are presented under "Radiative Transport Models." Information on collisional relaxation times and radiative lifetimes of different species (in their appropriate states) are presented next ("Radiative Lifetimes and Collisional Processes for the Shock-Layer Gases"). Thermodynamic and transport properties for each species considered in the shock layer are then given ("Thermodynamic and Transport Properties"), followed by solution procedures for the NLTE radiative flux equations and other shock-layer equations in "Method of Solution." The entire results of the study are summarized in "Results and Discussion," followed by "Conclusions."

LIST OF SYMBOLS

A_{nm} Einstein coefficient for spontaneous emission

$A'\pi_u$ lower electronic energy level for the C_2-Freymark transition

$a^3\pi_u$ lower electronic energy level for the C_2-Swan transition

B_{mn} Einstein coefficient for absorption

B_{nm} Einstein coefficient for stimulated emission

B_ν Planck function

c speed of light

C_{10} collisional deexcitation rate coefficient

C_i mass fraction of species i in the shock layer, ρ_i/ρ

C_p equilibrium specific heat of mixture, $\Sigma \, C_i \, C_{p,i}$

$C_{p,i}$ specific heat of species i, $C^*_{p,i}/C_{p,\infty}$

D_{ij} binary diffusion coefficient

$D'\Sigma^+_u$ upper electronic energy level for the C_2-Mulliken transition

$d^3\pi_g$ upper energy level for the C_2-Swan transition

$E'\Sigma^+_g$ upper energy level for the C_2-Freymark transition

h specific enthalpy, h^*/V_∞^{*2} (also Planck constant)

H_T total enthalpy, $h + (u^2 + v^2)/2$

I_ν intensity of radiation

$\overline{I}_\nu$ mean radiation intensity averaged over the spectral interval $\Delta\nu$

J_ν NLTE source function

J_i mass diffusion flux of species i, $J^*_i \, R_N/\mu^*_{ref}$

k thermal conductivity of mixture, $k^*/\mu^*_{ref} \, C^*_{p,\infty}$ (also Boltzmann constant)

Le Lewis number, $\rho^* \, D^*_{ij} \, C^*_p/k^*$

M^* molecular weight of mixture

m_1 net weight of a H_2 molecule, gm/molecule

m_a ablation mass loss rate, kg m^2 sec^{-1}

$\overline{m}$ principal quantum number of the lower level

N_{H_2} number density of H_2

N_m number density of particles in the mth level

N_n number density of particles in the nth level

n coordinate normal to the body surface

$\overline{n}$ principal quantum number of the upper level

P pressure, $P^*/(\rho_\infty^* V_\infty^{*2})$

Pr Prandtl number, $\mu^* C_p^*/k^*$

$q_{c,w}$ convective heat flux to the body

q_R net radiative heat flux, $q_R^*/(\rho_\infty^* V_\infty^{*3})$

$q_{R,w}$ radiative heat flux to the body

R_N^* body nose radius

R^* universal gas constant

R_b^* radius of the body

r radius measured from axis of symmetry to a point on the body surface, r^*/R^*

r_s radius measured from axis of symmetry to a point on the bow shock, r_s^*/R_N^*

$|R_e/ea_o|$ electronic transition moment

S spin quantum number

Sc Schmidt number

s coordinate along the bow shock, s^*/R_N^*

T temperature, T^*/T_{ref}^*

T^* dimensional temperature

T_{ref}^* reference temperature, $V_\infty^*/C_{p,\infty}^*$

u	velocity tangent to body surface, u^*/V_∞^*
v	velocity normal to body surface, v^*/V_∞^*
V_∞^*	free-stream velocity, km/sec
$\bar{v}$	mean speed of the colliding species, cm sec^{-2}
$x'\Sigma_g^+$	lower energy level for the C_2-Mulliken transition
Z	entry altitude, km
α	shock angle, defined in figure 1
Γ	quantity defined as $\Gamma = 1 + \kappa n = 1 + \kappa\delta\eta$
δ	shock-layer thickness (same as n_s), $f(\xi,t)$
ϵ	gray surface emittance
ϵ_1	surface emittance of the body
ϵ_2	surface emittance of the shock
Θ	body angle defined in figure 1
η	transformed n coordinate, $n/n_s = n/\delta$
η_c	collisional relaxation time
η_r	radiative lifetime
κ	body curvature ($= - d\Theta/ds$), $\kappa^* R_N^*$
κ_ν	spectral absorption coefficient
ξ	coordinate along the body surface, $\xi = s$
μ	viscosity of mixture, μ^*/μ_{ref}^*
μ_{ref}^*	reference viscosity, $\mu^*(T_{ref}^*)$
ρ	density of mixture, ρ^*/ρ_∞^*
σ	Stefan Boltzmann constant
τ	optical coordinate
τ_o	optical thickness

Subscripts

i	ith species
s	shock value
w	wall value
∞	free-stream condition
ν	radiation frequency
k,o	lower state of the energy level
j,1	upper state of the energy level

Superscripts

"	lower state of the energy level
'	upper state of the energy level
*	dimensional quantity

BASIC FORMULATION

Introduction

The physical model and coordinate system for a Jovian entry body are shown in figure 1. In this figure, s is the distance measured along the body surface and n is the distance normal to the body surface. The flow in the shock layer is considered to be axisymmetric, steady, radiating and in chemical equilibrium. Both inviscid as well as viscous shock-layer analyses are considered in the present study. The basic governing equations (along with the appropriate boundary conditions) are presented in this section.

Inviscid Flow Equations

For the physical model considered, the governing equations for inviscid flow are expressed as (refs. 28, 29):

Continuity:

$$(\partial/\partial s) \; [(r + n \cos \theta)\rho u] + (\partial/\partial n) \; (\Gamma \zeta \rho v) = 0 \tag{1}$$

s-momentum:

$$(u/\Gamma) \; (\partial u/\partial s) + v(\partial u/\partial n) + (uv\kappa/\Gamma) + (1/\rho\Gamma) \; (\partial p/\partial s) = 0 \tag{2}$$

n-momentum:

$$(u/\Gamma) \; (\partial v/\partial s) + v(\partial v/\partial n) - (u^2\kappa/\Gamma) + \rho^{-1}(\partial p/\partial n) = 0 \tag{3}$$

Energy:

$$(u/\Gamma) \; (\partial H/\partial s) + v(\partial H/\partial n) - (u/\rho\Gamma) \; (\partial p/\partial s)$$

$$- (v/\rho) \; (\partial p/\partial n) + (1/\rho) \; (\text{div } q_R) = 0 \tag{4}$$

where

$$\Gamma = 1 + n\kappa$$

$$\text{div } q_R = (\partial q_R/\partial n) + q_R[(\kappa/\Gamma) + (\cos \theta/r)]$$
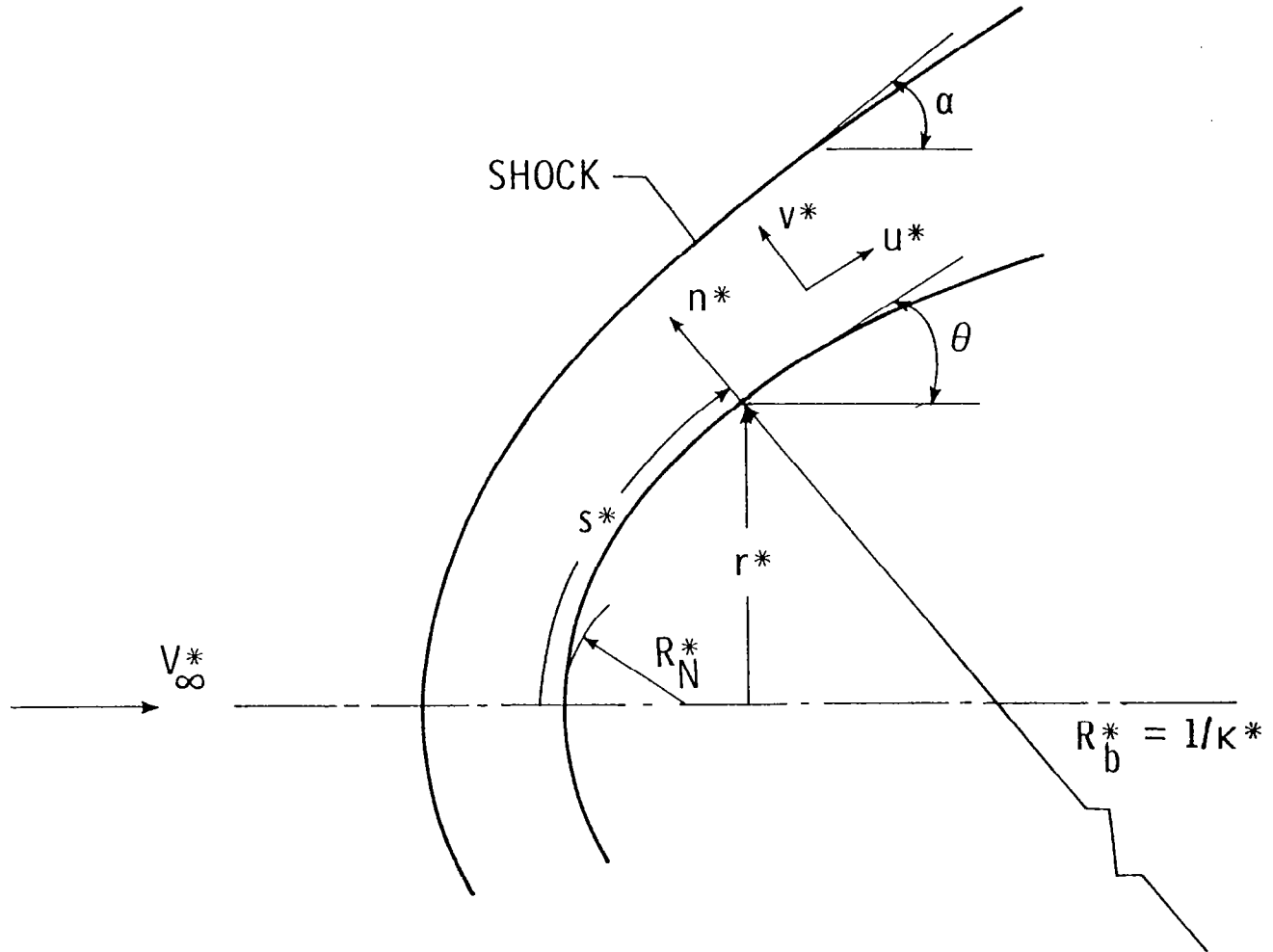
Figure 1. Physical model and coordinate system.

It should be noted that the above equations are written in nondimensional form. The quantities used to nondimensionalize these equations are defined as:

$$s = s^*/R_N^* \qquad n = n^*/R_N^* \qquad u = u^*/V_\infty^*$$

$$\rho = \rho^*/\rho_\infty^* \qquad p = p^*/(\rho_\infty^* V_\infty^{*2}) \qquad h = h^*/V_\infty^{*2}$$

$$r = r^*/R_N^* \qquad q_R = q_R^*/(\rho_\infty^* V_\infty^{*3}) \qquad \kappa = \kappa^*/R_N^* \qquad (5)$$

Viscous Flow Equations

Basic governing equations for viscous shock layer are obtained from the steady-state Navier-Stokes equations by keeping terms up to second order in the inverse square root of the Reynolds number, ε, as (refs. 5, 30):

Continuity:

$$(\partial/\partial s) [(r + n \cos \theta)\rho u] + (\partial/\partial n) (\Gamma \zeta \rho v) = 0 \qquad (6)$$

s-momentum:

$$\rho [(u/\Gamma) (\partial u/\partial s) + v(\partial u/\partial n) + (uv\kappa/\Gamma)] + \Gamma^{-1}(\partial p/\partial s)$$

$$= \varepsilon^2 \{(\partial/\partial n) (\mu \psi) + \mu[(2\kappa/\Gamma) + (\cos \theta/\zeta)]\psi\} \qquad (7)$$

n-momentum:

$$\rho [(u/\Gamma) (\partial v/\partial s) + v(\partial v/\partial n) - (u^2\kappa/\Gamma)] + (\partial p/\partial n) = 0 \qquad (8)$$

Energy:

$$\rho [(u/\Gamma) (\partial H/\partial s) + v(\partial H/\partial n)] - v(\partial p/\partial n) + \rho u^2 (v\kappa/\Gamma)$$

$$= \varepsilon^2 [(\partial/\partial n)\Phi_1 + \Phi_2] - \{ (\partial q_R/\partial n) + q_R[(\kappa/\Gamma) + (\cos \theta/r)]\} \qquad (9a)$$

where

$$\Psi = (\partial u/\partial n) - (u\kappa/\Gamma)$$

$$\Phi_1 = (\mu/Pr)(\partial H/\partial n) - (\mu/Pr)\sum_{i=1}^{N_S} h_i (\partial c_i/\partial n) - \sum_{i=1}^{N_S} h_i J_i$$

$$+ (\mu/Pr)(Pr - 1) u(\partial u/\partial n) - (\mu\kappa u^2/\Gamma) \tag{9b}$$

$$\Phi_2 = [(\kappa/\Gamma) + (\cos\theta/\zeta)]\Phi_1 \tag{9c}$$

In the preceding equations, the total enthalpy $H = [(u^2 + v^2)/2] + h$ and J_i is the mass flux relative to the mass velocity and is given by (refs. 31, 32):

$$J_i = (\mu/Pr) Le(\partial c_i/\partial n) \tag{10}$$

In equation (10), Le represents the multicomponent Lewis number and, in the present analysis, is taken to be a constant for all species as 1.10. In addition to the quantities given in equation (5), the terms used to nondimensionalize the above set of viscous equations are

$$Pr = \mu^* C_p^*/k^* \qquad Le = \rho^* C_p^* D_{ij}^*/k^* \qquad \mu = \mu^*/\mu_{Ref}^*$$

$$k = k^*/(\mu_{Ref}^* C_{p,\infty}^*) \qquad C_p = C_p^*/C_{p,\infty}^* \qquad \mu_{Ref}^* = \bar{\mu}^*(V_\infty^*/C_{p,\infty}^*)$$

$$J_i = J_i^* R_N^*/\mu_{Ref}^* \qquad \varepsilon = [\mu_{Ref}^*/(\rho^* V_\infty^* R_N^*)]^{1/2} \tag{11}$$

In addition to the preceding set of equations for the inviscid and viscous shock-layer flow, the species continuity equation and equation of state are needed to complete the set of equations. The species continuity is given by the expression

$$\rho[(u/\Gamma)(\partial C_i/\partial s) + v(\partial C_i/\partial n)] = (\varepsilon^2/\Gamma\zeta)[(\partial/\partial n)(\Gamma\zeta J_i)] \tag{12a}$$

where

$$\zeta = r + n \cos \theta \qquad (12b)$$

The equation of state for the gas, in general, can be expressed as

$$p = \rho T(R^*/M^* C_{p,\infty}) \qquad (13)$$

where $C_{p,\infty}$ represents the specific heat of the gas at the free-stream conditions. The expression for the equation of state for a hydrogen/helium mixture is given by Zoby et al. (ref. 33) as:

$$T^* = C_T[(p^*/1013250)^{\ell}/(\rho^*/0.001292)^{k}] \qquad (14a)$$

$$H^* = C_H[(p^*/1013250)^{m}/(\rho^*/0.001292)^{n}] \quad (R^* T_o^*/M^*) \qquad (14b)$$

where

$$k = 0.65206 - 0.04407 \, \ell n(X_{H2})$$

$$\ell = 0.67389 - 0.04637 \, \ell n(X_{H2})$$

$$m = 0.95252 - 0.1447 \, \ell n(X_{H2})$$

$$n = 0.97556 - 0.16149 \, \ell n(X_{H2})$$

$$U_t = V_\infty \sin \theta [1 + 0.7476(1 - X_{H2})]$$

$$CTU = -545.37 + 61.608 \, U_t - 22459 \, U_t^2 + 0.039922 \, U_t^3$$
$$- 0.00035148 \, U_t^4 + 0.0000012361 \, U_t^5$$

$$CHU = 5.6611 - 0.52661 \, U_t^2 + 0.020376 \, U_t - 0.00037861 \, U_t^3$$
$$+ 0.0000034265 \, U_t^4 - 0.000000012206 \, U_t^5$$

$$C_T = CTU + 61.2 \, (1-X_{H2})$$

$$C_H = CHU - 0.3167 (1-X_{H2})$$

and X_{H2} represents the mole fraction of H_2.

Free-Stream and Boundary Conditions

The Jupiter atmosphere mainly consists of hydrogen and helium gases. In the past, the nominal composition of the atmosphere was assumed to be 85 percent hydrogen and 15 percent helium (ref. 34). For different entry times and altitudes, the free-stream conditions are different. The values used in the present study at different altitudes are given in table 1.

Table 1. Free-stream conditions for Jovian entry

Altitude Z, km	Velocity V_∞^*, km/sec	Density ρ_∞^*, kg/m^3	Pressure ρ_∞^*, N/m^2	Temperature T_∞^*, K
109	35.207	7.197E-4	443.02	163.72
116	39.09	4.360E-4	245.00	166.91
138	44.04	2.127E-4	132.00	167.02

The free-stream enthalpy can be calculated by the relation (ref. 35):

$$H_\infty = 1.527 \, RT_\infty \qquad (15)$$

where R = 8.135 Joules/K-mole is the universal gas constant. The number density of hydrogen can be calculated by the ideal gas law and the relation can be given as

$$N_{H_2} = (7.243117 \times 10^{22}) \, (P_\infty/T_\infty) \, X_{H_2} \qquad (16)$$

where X_{H_2} is the mole fraction of H_2.

In order to solve the set of governing equations [eqs. (1) to (14)], it is essential to specify appropriate boundary conditions at the body surface and shock interface. In all cases, the boundary conditions immediately behind the shock wave are calculated by using the Rankine-Hugoniot relations. In the viscous analysis, the no-slip and no-temperature-jump boundary conditions are used. Consequently, the velocities at the surface are

$$u(o,n) = u_w = 0 \tag{17}$$

$$v(o,n) = v_w = 0 \tag{18}$$

The boundary condition given by equation (18) is valid only for the case with no mass injection. For this case, the temperature at the wall is usually specified as

$$T_w = \text{const.} \tag{19}$$

For the case of ablation mass injection, the wall temperature is either specified or calculated. For the calculated wall temperature conditions, the wall temperature is the sublimation temperature of the ablator surface. Moreover, the ablation process is assumed to be quasi-steady. With these assumptions, the expressions for the coupled mass injection rate and the sublimation temperature (for the carbon-phenolic heat shield material considered in this study) are given by

$$\dot{m} = \left\{ (-q_{c,w}^* - q_{R,w}^*) / \left[\sum_{i=1}^{N_s} (C_i \, h_i^*)_w - h_A^* \right] \right\} / (\rho_\infty^* \, V_\infty^*) \tag{20}$$

$$T_{Sub}^* = \sum_{j=1}^{5} \lambda_{1,j} \, C_A^{j-1} + \log p_w^* \sum_{j=1}^{5} \lambda_{2,j} \, C_A^{j-1}$$

$$+ \log p_w^* \sum_{j=1}^{5} \lambda_{3,j} \, C_A^{j-1} \tag{21}$$

where p_w^* is the wall pressure in atmospheres and C_A is the ablator mass fraction at the wall. The $\lambda_{i,j}$ coefficients whose values are given in references 5, 30, and 36 to 39 are applicable for a free-stream gas composition of 89 percent hydrogen and 11 percent helium by mole fraction and for ablator mass fractions of 0.4 to 1.0. If the ablator mass fraction at the wall is unity, then these coefficients are valid for any free-stream gas mixture. For ablation injection, the elemental concentrations at the wall are governed by convection and diffusion and are given by

$$(\partial c_i/\partial n)_w - (1/\varepsilon^2)(\dot{m} Sc/\mu)_w [(c_i)_w - (c_i)_-] = 0 \qquad (22)$$

where Sc is the Schmidt number (Sc = Pr/Le) and $(c_i)_-$ is the elemental mass fraction of the solid ablator material at the surface.

The heat transferred to the wall due to conduction and mass diffusion is referred to as the convective heat flux and is given by the expression

$$-q_{c,w} = \varepsilon^2 [(k \partial T/\partial n) + (\mu/Sc) \sum_{i=1}^{N_s} h_i (\partial c_i/\partial n)]_w \qquad (23)$$

The radiative flux emitted from the wall is given by the relation

$$q_R^+(0) = q_{R,w}^+ = \varepsilon_w \sigma T^{*4} \qquad (24)$$

A value of surface emittance $\varepsilon_w = 0.8$ is used in this study.

RADIATIVE TRANSPORT MODELS

Introduction

An appropriate expression for the radiative flux q_R is needed
for the solution of the energy equation presented in the previous
section. This requires a suitable radiative transport model and a
meaningful spectral model for variation of the absorption coefficient
of the gas. In this section appropriate expressions for the spectral
and total radiative flux are given, and a detailed discussion of
models for the spectral absorption by the hydrogen-helium gas and
other important ablative species in the shock layer is presented.

Radiative Flux Equations

The equations for radiative transport, in general, are integral
equations which involve integration over both frequency spectrum and
physical coordinates. In many physically realistic problems, the
complexity of the three-dimensional radiative transfer can be reduced
by introduction of the "tangent slab approximation." This approximation
treats the gas layer as a one-dimensional slab in calculation of the
radiative transport. Radiation in directions other than normal to
either the body or shock is neglected in comparison. Discussions on
the validity of this approximation for planetary entry conditions are
given in references 40 to 43. The tangent slab approximation is
employed in this study. It should be pointed out here that this
approximation is used only for the radiative transport calculations
and not for other flow variables.

<u>LTE radiative flux equations</u>. - For the present study, the
equations of radiative transport are obtained for a gas confined
between two infinite, parallel boundaries, the shock wave and the
body. This is shown in figure 2. For one-dimensional radiation,
the equations of transfer for a nonscattering medium in local
thermodynamic equilibrium (refs. 20, 21) are given by

$$\mu(dI_\nu^+/d\tau_\nu) = B_\nu(\tau_\nu) - I_\nu^+ \tag{25a}$$

$$\mu(dI_\nu^-/d\tau_\nu) = B_\nu(\tau_\nu) - I_\nu^- \tag{25b}$$

where

$$\mu = \cos\theta \tag{26a}$$

$$\tau_\nu = \int_0^n \kappa_\nu(n)\ dn \tag{26b}$$

$$\tau_{o\nu} = \int_0^{n_s} \kappa_\nu(n)\ dn \tag{26c}$$

In the above equations, κ_ν and B_ν represent the frequency-dependent linear absorption coefficient and Planck function, respectively. Furthermore, it should be noted that I_ν^+ and I_ν^- correspond to positive and negative values of μ, respectively. The boundary conditions for equations (25a) and (25b) can be expressed as

$$I_\nu^+(\tau_\nu,\mu) = I_\nu^+(0,\mu),\ \tau_\nu = 0 \tag{27a}$$

$$I_\nu^-(\tau_\nu,\mu) = I_\mu^-(\tau_{o\nu},\mu),\ \tau_\nu = \tau_{o\nu} \tag{27b}$$

By employing the above conditions, integration of equations (25a) and (25b) results in

$$I_\nu^+(\tau_\nu,\mu) = I_\nu^+(0,\mu)\ \exp(-\tau_\nu'/\mu) + \int_0^{\tau_\nu} B(t)$$

$$\times \exp[-(\tau_\nu - t)/\mu]\mu^{-1}dt \tag{28a}$$

$$I_\nu^-(\tau_\nu,\mu) = I_\nu^-(\tau_{o\nu},\mu)\ \exp[-(\tau_{o\nu} - \tau_\nu)/\mu]$$

$$-\int_{\tau_\nu}^{\tau_{o\nu}} B_\nu(t)\ \exp[-(t - \tau_\nu)/\mu]\mu^{-1}\ dt \tag{28b}$$

22
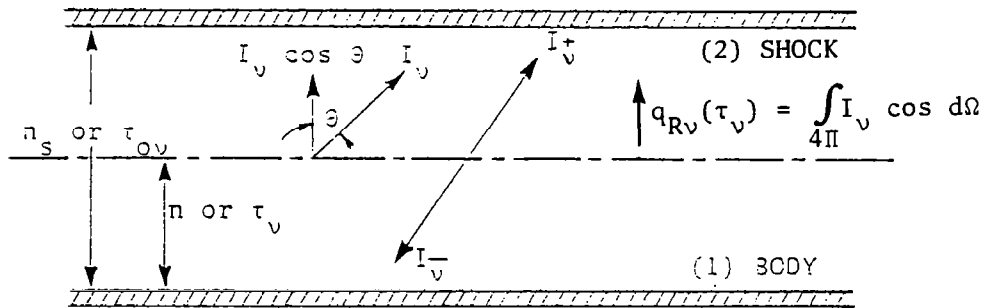
Figure 2. Physical model and coordinate system for the radiation field.

Equations (28a) and (28b) describe the radiation field in terms of the temperature field within the medium. The temperature field is expressed by the Planck function. The term $I_\nu^+(0,\mu) \exp(-\tau_\nu/\mu)$ in equation (28a) represents the radiant energy that originated at the body surface which has been attenuated by the factor $\exp(-\tau_\nu/\mu)$ as a result of absorption. The integral term represents the augmentation of I_ν^+ due to gaseous emission. A similar explanation goes for equation (28b), with respect to the shock surface.

Referring to figure 2, the spectral radiative flux is expressed in terms of intensity of radiation (ref. 21) as

$$q_{R\nu}(\tau_\nu) = \int_{4\pi} I_\nu \cos\theta \, d\Omega = 2\pi \int_{-1}^{1} I_\nu(\tau_\nu, \mu)\mu \, d\mu \tag{29}$$

By noting that I_ν^+ and I_ν^- correspond to positive and negative values of μ, equation (29) can be expressed as

$$q_{R\nu}(\tau_\nu) = 2\pi \int_{0}^{1} I_\nu^+ \mu \, d\mu - 2\pi \int_{0}^{-1} I_\nu^- \mu \, d\mu \tag{30}$$

The substitution of values for I_ν^+ and I_ν^- from equations (28a) and (28b) into equation (30) results in the one-dimensional expression for spectral radiative flux (ref. 21) as

$$q_{R\nu}(\tau_\nu) = 2\pi \left\{ \int_0^1 I^+(0,\mu) e^{-\tau_\nu/\mu} + \int_0^{\tau_\nu} B_\nu(t) E_2(\tau_\nu - t) dt \right.$$

$$- \left[\int_0^1 I_\nu^-(\tau_{o\nu}, -\mu) e^{-(\tau_{o\nu} - \tau_\nu)/\mu} \mu \, d\mu \right.$$

$$\left. \left. + \int_{\tau_\nu}^{\tau_{o\nu}} B_\nu(t) E_2(t - \tau_\nu) \, dt \right] \right\} \tag{31}$$

24

where $E_n(t)$ is the exponential integral function defined by

$$E_n(t) = \int_0^1 \mu^{n-2} e^{-t/\mu} d\mu \tag{32}$$

The expression for the net radiative flux at any location is given by

$$q_R(n) = \int_0^\infty q_{R\nu}(\tau_\nu) \, d\nu \tag{33}$$

Often, it is desirable to obtain separate relations for total radiative flux going towards the body and the bow shock. Upon denoting the radiative flux towards the shock by q_R^+ and towards the body by q_R^-, equation (33) can be written as

$$q_R(n) = q_R^+(n) - q_R^-(n) = \int_0^\infty q_{R\nu}^+(\tau_\nu) \, d\nu - \int_0^\infty q_{R\nu}^-(\tau_\nu) \, d\nu \tag{34}$$

where

$$q_R^+ = 2\pi \int_0^\infty \left[\int_0^1 I_\nu^+(0,\mu) e^{-\tau_\nu/\mu} \mu \, d\mu + \int_0^{\tau_\nu} B_\nu(t) \right.$$

$$\left. \cdot E_2(\tau_\nu - t) \, dt \right] d\nu \tag{35a}$$

$$q_R^- = 2\pi \int_0^\infty \left[\int_0^1 I_\nu^-(\tau_{o\nu}, -\mu) e^{-(\tau_{o\nu} - \tau_\nu)/\mu} \mu \, d\mu \right.$$

$$\left. + \int_{\tau_\nu}^{\tau_{o\nu}} B_\nu(t) E_2(t - \tau_\nu) \, dt \right] d\nu \tag{35b}$$

For diffuse surfaces, $I_\nu^+(0,\mu)$ and $I_\nu^-(\tau_{o\nu}, \mu)$ are independent of direction (i.e., independent of μ) and may be expressed in terms of surface radiosities $B_{1\nu}$ and $B_{2\nu}$ as

$$\pi I_\nu^+(o,\mu) = B_{1\nu}, \quad \pi I_\nu^-(\tau_{o\nu},\mu) = B_{2\nu}$$

Hence, equations (35a) and (35b) are expressed as

$$q_\nu^+(n) = 2 \int_0^\infty \left[B_{1\nu} E_3(\tau_\nu) + \pi \int_0^{\tau_\nu} B_\nu(t) E_2(\tau_\nu - t) \, dt \right] d\nu \tag{36}$$

$$q_R^-(n) = 2 \int_0^\infty \left[B_{2\nu} E_3(\tau_{o\nu} - \tau_\nu) + \pi \int_{\tau_\nu}^{\tau_{o\nu}} B_\nu(t) E_2(t - \tau_\nu) \, dt \right] d\nu \tag{37}$$

The expressions for surface radiosities appearing in this equation (ref. 21) are given by

$$B_{1\nu} = \varepsilon_{1\nu}[\pi B_\nu(T_w)] + 2 \rho_{1\nu}\left[B_{2\nu} E_3(\tau_{o\nu}) + \int_0^{\tau_{o\nu}} \pi B_\nu(t) E_2(t) \, dt \right] \tag{38a}$$

$$B_{2\nu} = \varepsilon_{2\nu}[\pi B_\nu(T_s)] + 2 \rho_{2\nu}\left[B_{1\nu} E_3(\tau_{o\nu}) + \int_0^{\tau_{o\nu}} \pi B_\nu(t) \right.$$

$$\left. E_2(\tau_{o\nu} - t) \, dt \right] \tag{38b}$$

where $\rho_{1\nu}$ and $\rho_{2\nu}$ represent the surface reflectance of the body and the shock respectively. For nonreflecting surfaces, $\rho_{1\nu} = \rho_{2\nu} = 0$, and equations (38a) and (38b) reduce to

$$B_{1\nu} = \pi \varepsilon_{1\nu} B_\nu(T_w), \quad B_{2\nu} = \pi \varepsilon_{2\nu} B_\nu(T_s) \tag{39}$$

Sometimes it is convenient to express the radiative flux equations in terms of gas emissivities, defined by

$$\varepsilon_\nu^+ = 1 - 2E_3(\tau_\nu - t), \quad \varepsilon_\nu^- = 1 - 2E_3(t - \tau_\nu) \tag{40}$$

By noting that

$$d\epsilon_\nu^+ = -2E_2(\tau_\nu - t)\, dt, \quad d\epsilon_\nu^- = 2E_2(t - \tau_\nu)\, dt$$

$$\epsilon_\nu^+(t = 0) = 1 - 2E_3(\tau_\nu) = \epsilon_b^+ = \epsilon_w^+$$

$$\epsilon_\nu^+(t = \tau_\nu) = 1 - 2E_3(0) = 1 - 2(1/2) = 0 = \epsilon_\nu^-(t = \tau_\nu)$$

$$\epsilon_\nu^-(t = \tau_{o\nu}) = 1 - 2E_3(\tau_{o\nu} - \tau_\nu) = \epsilon_b^- = \epsilon_s^-$$

equations (36) and (37) can be written as

$$q_R^+(n) = \int_0^\infty \left[2B_{1\nu}\, E_3(\tau_\nu) + \pi \int_0^{\epsilon_w^+} B_\nu(\epsilon_\nu^+)\, d\epsilon_\nu^+ \right] d\nu \tag{41a}$$

$$q_R^-(n) = \int_0^\infty \left[2B_{2\nu}\, E_3(\tau_{o\nu} - \tau_\nu) + \pi \int_0^{\epsilon_s^-} B_\nu(\epsilon_\nu^-)\, d\epsilon_\nu^- \right] d\nu \tag{41b}$$

If the radiative flux into the slab at the boundaries is neglected, then the first right-hand term in equations (41a) and (41b) vanishes and the net radiative flux is given by

$$q_R(n) = \pi \int_0^\infty \left[\int_0^{\epsilon_w^+} B_\nu(\epsilon_\nu^+)\, d\epsilon_\nu^+ - \int_0^{\epsilon_s^-} B_\nu(\epsilon_\nu^-)\, d\epsilon_\nu^- \right] d\nu \tag{42}$$

Depending upon the particular assumptions made in a physical problem, use is made of either equations (36) and (37), (41a) and (41b), or (42) in obtaining the net radiative heat flux.

For mathematical convenience, exponential integrals often are approximated by appropriate exponential functions. There are a few standard procedures for doing this, and these are discussed in

references 20 and 21. It has been demonstrated (e.g. ref. 21) that when the exponential integral of third order is approximated by

$$2E_3(z) = \exp(-2z) \tag{43}$$

the radiative transport solutions are exact in the optically thin limit, and of satisfactory accuracy in the optically thick limit. By using equation (43), approximate expressions for the gas emissivities are obtained from equation (40) as

$$\varepsilon_\nu^- = 1 - \exp[2(t - \tau_\nu)] \tag{44a}$$

$$\varepsilon_\nu^+ = 1 - \exp[2(\tau_\nu - t)] \tag{44b}$$

Since $E_n(z) = -E_{n-1}(z)$, one could obtain the relation for the exponential integral of second order by differentiating equation (43) as

$$E_2(z) = \exp(-2z) \tag{45}$$

Use of equations (43) and (45) could be made directly in equations (34), (35a) and (35b) to obtain appropriate relations for the radiative heat flux.

In this study, use of the exponential kernel approximation, as given by equations (43) and (45), is made for the radiative transport in the shock layer. Furthermore, the bow shock is considered transparent, and the free stream is considered cold and transparent. For the evaluation of the equilibrium spectral radiative flux, equations (36) and (37) are used in the present analysis.

NLTE radiative flux equations. - In the previous subsection, the transfer equation and the resulting radiative flux equations were obtained under the condition of local thermodynamic equilibrium. For this situation, molecular distribution in the various energy

levels is collision dominated, and the emission process depends on the local equilibrium temperature alone. The treatment outlined in obtaining these equations is of a macroscopic nature. The NLTE situation, on the other hand, involves a study of the individual molecules of the radiating system since these particles do not obey the equilibrium Boltzmann distribution. The derivation of the NLTE transfer equation employs a quantum mechanics treatment. The equation of radiative transfer, in general, may be expressed in terms of Einstein coefficients A_{nm}, B_{nm}, and B_{mn} (refs. 20, 44) as

$$dI_{\nu}/dn = \rho \overline{\kappa}_{\nu} [1 - (N_n/N_m)(B_{nm}/B_{mn})]$$
$$\times A_{nm} \left[B_{mn} \left\{ (N_m/N_n)(B_{mn}/B_{nm}) - 1 \right\} - I_{\nu} \right] \tag{46}$$

where N_n represents the number density of the nth level, B_{mn} is the Einstein coefficient for absorption, B_{nm} is the Einstein coefficient for stimulated emission, and A_{nm} is the Einstein coefficient for spontaneous emission. The above equation can be written in a simplified form as

$$dI_{\nu}/dn = \rho \kappa_{\nu} (J_{\nu} - I_{\nu}) \tag{47}$$

where J_{ν} is the NLTE source function and κ_{ν} is the reduced absorption coefficient which includes the effect of induced emission (negative absorption) in the medium and is defined as

$$\kappa_{\nu} = \overline{\kappa}_{\nu} [1 - (N_n/N_m)(B_{nm}/B_{mn})] \tag{48}$$

In this equation $\overline{\kappa}_{\nu}$ is the equilibrium absorption coefficient. The NLTE source function is given in terms of the population ratio as

$$J_\nu = A_{nm} / \left\{ B_{nm} \left[(N_m/N_n) \ (B_{mn}/B_{nm}) \ -1 \right] \right\} \qquad (49)$$

By making use of the relations between the Einstein coefficients, the source function can be expressed (refs. 14, 20, 44, 45) as

$$J_\nu = (2h\nu^3/c^2)/[(N_m/N_n) \ (g_n/g_m) - 1] \qquad (50)$$

where

$$A_{nm} = (2h\nu^3/c^2) \ B_{nm} \qquad (51a)$$

$$B_{nm} = (g_m/g_n) \ B_{mn} \qquad (51b)$$

In this equation h represents the Planck constant and g_m and g_n are corresponding statistical weight factors for the lower and upper energy levels (different for different species), which are assumed to be unity in the present analysis.

From equations (48) and (50), it is evident that the state population ratio N_m/N_n has to be known in order to evaluate the nonequilibrium absorption coefficient and NLTE source function. This is achieved by the method of detailed balancing of various transition processes. The three processes involved in the steady-state detailed balancing are the induced absorption, induced emission, and spontaneous (stimulated) emission. In the induced absorption process, a quantum of radiation of appropriate energy and frequency is absorbed, and this results in exciting an atom (or molecule). In the induced emission, a quantum of radiation interacts with an excited particle to give emission of another quantum of the same energy, and thereby the particle reverts to the lower energy state. In the spontaneous emission case, an excited particle spontaneously emits a quantum of radiation of the appropriate frequency and reverts to a lower energy state. These processes may be expressed as

$$M + h\nu \rightarrow M^*$$

$$M^* + h\nu \rightarrow M + 2h\nu$$

$$M^* \rightarrow M + h\nu \qquad (52)$$
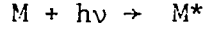
where M^* denotes the excited state of the species M. The statistical steady-state equation for a particular electronic state is given by

$$dN_1/dt = 0$$

This implies that the sums of the radiative and collisional rates into and out of the state 1 must be equal. By employing this criterion, the state population ratio for any two levels in a multilevel system consisting of k levels is expressed (ref. 10) as

$$N_m/N_n = \left[\sum_k P_{nk} Q_{km,n} \Big/ \sum_k P_{mk} Q_{kn,m} \right] \qquad (53)$$

where P_{nk} is the sum of the radiative term A_{nk} and the collision term C_{nk}. The quantity $Q_{km,n}$ is the probability for all transitions from level k to m not involving n such that for k = m, $Q_{kk,n} = 1$.

Upon combining equations (50) and (53), the source function for the transition between levels n and m (containing k intermediate levels)(ref. 46) is given by

$$J_\nu = [\int_{\Delta\nu} I_\nu^* \phi_\nu \, d\nu + \epsilon^* + \theta^*]/(1 + \epsilon^* + \eta^* - \delta\theta) \qquad (54)$$

where

$$\theta = \left(1/B_{mn}\right) \sum_{\substack{\ell=1 \\ \ell \neq n,m}}^{k} P_{m\ell} \, Q_{\ell n,m} \tag{55a}$$

$$\eta^* = \left(1/A_{nm}\right) \sum_{\substack{\ell=1 \\ \ell \neq n,m}}^{k} P_{n\ell} \, Q_{\ell m,n} \tag{55b}$$

$$\varepsilon^* = C_{nm} / \left[B_{mn} \, B_\nu(T)\right] \tag{55c}$$

$$\delta = c^2/2h\nu^3, \quad I_\nu^* = I_\nu/B_\nu(T), \quad \theta^* = \theta/B_\nu(T) \tag{56}$$

Equations (53) and (54) simplify considerably if the level of transitions involved is lower. For example, in a three-level transition the relation for the population ratio N_o/N_1 is obtained from equation (53) as

$$N_o/N_1 = [A_{10} + B_{10}\overline{I}_{\Delta\nu} + C_{10} + C_{20}(B_{12}\overline{I}_{\Delta\nu} + C_{12})]/Q_T$$

$$\cdot \left\{ [B_{01}I_{\Delta\nu} + C_{01} + C_{02}(A_{21} + C_{21} + B_{21}\overline{I}_{\Delta\nu})]/Q_T \right\}^{-1} \tag{57}$$

In this equation, Q_T represents the total probability for transitions from level 2 (i.e., from the third level) and is given by

$$Q_T = A_{21} + B_{21} \, \overline{I}_{\Delta\nu} + C_{21} + C_{20} \tag{58}$$

32

It can be shown easily that, under equilibrium conditions, equation (57) reduces to the Boltzmann distribution as

$$N_0/N_1 = \exp(\Delta E/kT) \tag{59}$$

where $\Delta E = E_1 - E_0$ is the difference of energy (in eV) between levels 1 and 0.

Upon combining equations (50) and (57), a simplified expression for the source function (ref. 46) is obtained as

$$J_\nu = \left\{ (2h\nu^3/c^2)/[\exp(h\nu/kT) - 1] \right\}$$

$$\times [1 + \eta(\overline{I}_{\Delta\nu}/\overline{B}_{\Delta\nu}) + \delta_1]/(1 + \eta + \delta_2) \tag{60}$$

where

$$\overline{B}_{\Delta\nu} = 4\pi \int_{\Delta\nu} B_\nu \, d\nu \tag{61}$$

$$\delta_1 = C_{02}(A_{21} + C_{21} + B_{21} \overline{I}_{\Delta\nu})/(B_{01} Q_T) \tag{62a}$$

$$\delta_2 = [C_{20}(B_{12} \overline{I}_{\Delta\nu} + C_{12}) - C_{02}(A_{21} + C_{21} + B_{21} \overline{I}_{\Delta\nu})]/(A_{10} Q_T) \tag{62b}$$

In the preceding equations, $\eta = A_{10}/C_{10}$ represents the ratio of the collisional deactivation (or relaxation) time and radiative lifetime of the first excited state, and quantities δ_1 and δ_2 are the influence factors in the NLTE source function arising from the higher level energy transitions.

For a two-level transition, the expression for the source function, as given by equation (60), further simplifies (refs. 12, 47) as

$$J_\nu = B_\nu - \left\{ \eta[\int_{\Delta\nu}(dq_R/dy)d\nu]/4\pi \int_{\Delta\nu} \kappa\nu \, d\nu \right\} \tag{63}$$

It is evident from the equation (63) as well as from equation (60) that the degree of NLTE depends upon the magnitude of the quantities η, δ_1 and δ_2. Since values of δ_1 and δ_2 are always lower than η for all particles involving multilevel energy transitions, the extent of nonequilibrium is characterized essentially by the parameter η. This implies that the major contribution to the source function comes from the transitions (collisional as well as radiative) involving the ground state and the first excited state. Consequently, for $\eta \ll 1$, the source function becomes the Planck function, and the assumption of LTE is justified. In this case, the collisional process is sufficiently fast to deexcite the particles to the lower state before deexcitation takes place by the emission of radiation. On the other hand, the condition of radiative equilibrium is reached for $\eta \gg 1$, and in this case the entire process of excitation and deexcitation is radiatively controlled. The NLTE radiation becomes important for conditions where $\eta = O(1)$. By theoretical considerations, Jefferies (ref. 10) has established that the value of $\delta_{1,2}/\eta$ is approximately 0.1 for most gases involving multilevel energy transitions. Equation (60) is used in evaluating the nonequilibrium source function when no ablation mass injection is considered in the study. With ablation injection in the shock layer, equation (63) is used for the evaluation of J_ν to simplify the analysis.

To find the expression for the NLTE spectral radiative flux, the procedure outlined in the previous subsection under the LTE conditions [eqs. (29) to (42)] are applicable in general. However, in this case the NLTE transfer equation, given by equation (47), is integrated between the two parallel boundaries (the body and the shock). The formal solution of equation (47)(ref. 21) is given by

$$q_{R\nu}(\tau_\nu) = 2 \left\{ B_{1\nu} E_3(\tau_\nu) + \int_0^{\tau_\nu} J_\nu(t) \, E_2(\tau_\nu - t) \, dt \right.$$

$$\left. - [B_{2\nu} E_3(\tau_{o\nu} - \tau_\nu) + \pi \int_{\tau_\nu}^{\tau_{o\nu}} J_\nu(t) \, E_2(t - \tau_\nu) dt] \right\} \tag{64}$$

where τ_ν is the nonequilibrium optical thickness and is given in terms of the nonequilibrium absorption coefficient κ_ν^* as

$$\tau_\nu = \int_0^n \kappa_\nu^*(n) \, dn \tag{65}$$

Following equation (34), the total radiative flux may be divided into two components as q_R^+ going towards the shock and q_R^- going towards the body. Thus equation (64) is rewritten as

$$q_R^+(n) = 2 \int_0^\infty [B_{1\nu} E_3(\tau_\nu) + \pi \int_0^{\tau_\nu} J_\nu(t) E_2(\tau_\nu - t) \, dt] \, d\nu \tag{66a}$$

$$q_R^-(n) = 2 \int_0^\infty [B_{2\nu} E_3(\tau_{o\nu} - \tau_\nu) + \pi \int_{\tau_\nu}^{\tau_{o\nu}} J_\nu(t) E_2(t - \tau_\nu) \, dt] \, d\nu \tag{66b}$$

Since NLTE parameter η is the property of the absorbing/emitting species, the NLTE source function appears only in the terms which are attenuated by absorption of radiation by the gaseous species. Equations (64), (66a), and (66b) are used for evaluating the NLTE radiative flux.

Spectral Model for Gaseous Absorption

Appropriate spectral models for gaseous absorption are needed for the solution of the radiative flux equations [eqs. (37) and (66a)] derived under equilibrium and nonequilibrium conditions, respectively. The absorption model considered in this study is for a nongray gas with molecular band, continuum, and atomic line transitions. In general, the spectral absorption coefficient for continuum and line transitions may be expressed as

$$\kappa_{\nu} = \Sigma \ \kappa_i^C(\nu) \ + \ \Sigma \ \kappa_j^L(\nu) \qquad (67)$$

The summations in equation (67) extend over all continuum and line transitions, respectively. In the present analysis, only the transitions of the species H_2, H, and H^+ are considered for the no ablation case. For the case with carbon phenolic ablation injection, the additional chemical species C_2, C_3, C, C^+, C^-, CO, O, O_2, e^-, and O^+ are considered for the radiative transport.

The absorption coefficients for line transitions depend on the plasma conditions both through the population of the absorption levels and the shape of the spectral lines. For heavy atomic species at high temperatures, the dominant mechanism for the line broadening is the Stark broadening by electron impacts. Following Armstrong et al. (ref. 48), the lines can be treated as having the Lorentz shape, for which the shape factor is given by

$$b_k(\nu) = (\gamma_k^S/\pi)/[(\nu - \nu_k)^2 + (\gamma_k^S)^2] \qquad (68)$$

where ν_k is the frequency of the kth line center and γ_k^S is the Stark half-width of the line. In calculating the absorption co-efficients due to atomic line transitions, a line grouping technique is used. In this technique, line transitions near a specified frequency value are grouped together, and the spectral absorption is given as that from the line group. However, each line within the group is treated individually.

The continuum contribution depends mainly on the plasma state through the population of absorbing levels. The spectral absorption coefficient due to continuum transitions is given by

$$\kappa_i^C(\nu) = \Sigma \ N_{ij} \ \sigma_{ij}^C(\nu) \qquad (69)$$

where N_{ij} is the number density of the absorbing level and σ_{ij}^{C} is its cross section. The number density of the particular particle is obtained from thermodynamic state calculations.

By employing the detailed information on line and continuum absorption, Nicolet developed a fairly sophisticated radiative transport model for applications to planetary entry environment (refs. 17, 49, 50). For calculation of the equilibrium radiative transport properties in the ablation contaminated boundary layers, the method given in reference 49 is used. An approximate model for the frequency-dependent absorption coefficient is also developed by Sutton (see Zoby et al., ref. 18). In this model, the frequency dependence of the absorption coefficient is represented by a step-function with 58 steps of fixed (but not necessarily equal) widths. In this model, the absorption of helium species is neglected. In step-function models, the total absorption coefficient of the jth step is a summation of the average absorption coefficient for the ith transition in the jth step, given by

$$\kappa_j(\omega) = \sum_i \kappa_{ij}(\omega) \qquad (70a)$$

$$\kappa_{ij}(\omega) = (1/\Delta\nu_j) \int_{\nu_j}^{\nu_j+\Delta\nu_j} \kappa_i(\omega) \, d\nu \qquad (70b)$$

$$\kappa_i = f(T, N_i, \nu) \qquad (70c)$$

Once again κ is the equilibrium absorption coefficient, ν the frequency in eV, T is the temperature in degrees, and N_i is the number density in cm^{-3}. In this model, the absorption coefficients for the free-free and bound-free transitions of atomic hydrogen are expressed by

$$\kappa_{ff}^{H} = (2.61 \times 10^{-35} N_e N_{H^+})/(T^{1/2} \nu^3) \qquad (71)$$

$$\kappa_{bf}^{H} = [(1.99 \times 10^{-14} \, N_H)/\nu^3] \sum_{n_\ell=1}^{4} (1/n_\ell^3)$$

$$\cdot \exp\left\{(-157780/T) \, [1 - (1/n_\ell^2)]\right\} \qquad (72)$$

for $1 \leq n_\ell \leq 4$

and

$$\kappa_{bf}^{H} = [6.31 \times 10^{-20} \, (T/\nu^3) \, N_H] \, \exp(A) \, [\exp(B) - 1] \qquad (73)$$

for $4 < N_\ell \leq N_{\ell max}$

where

$$A = (-157880/T) \, [1 - (\delta/13.6)]$$

$$B = (157780/T) \, [(1/25) - (\delta/13.6)]$$

The reduction in the ionization potential δ is calculated by

$$\delta = (1.79 \times 10^{-5} \, N_e^{2/7})/(T^{1/7}) \qquad (74)$$

For bound-bound transition of hydrogen molecules and atoms

$$\kappa_{bb}^{H} = S \, b_k(\nu) \qquad (75)$$

where the line strength S is given by

$$S = (1.10 \times 10^{16} \, f \, n_\ell^2 \, N_H) \, \exp\left\{(-157780/T) \, [1 - (1/n_\ell^2)]\right\} \qquad (76)$$

38

The line-shape factor $b_K(\nu)$ is given by equation (68). Using the expressions given above, the absorptions due to continuum and line transitions over each step are calculated individually. The total absorption over each individual step is a strong function of temperature, and this model is valid for a wide range of temperatures. Further information on the 58-step model is available in reference 18. This model is used in evaluating the equilibrium absorption coefficient for the no ablation injection case.

At high temperatures, the frequency dependence of the absorption coefficient is more orderly because of the relative importance of continuum transitions over line transitions. Under such conditions, it is possible to represent the spectral absorption of the gas by a relatively fewer number of steps. A spectral model consisting of 30 steps is introduced in this study to represent the absorption by the hydrogen species in the spectral range of 0 to 20 eV. The absorption by the helium species is also neglected in this study. The procedure for developing this model is to calculate the spectral absorption coefficient first by employing Nicolet's detailed model. The 30-step model is illustrated in figure 3. Further details on this 30-step model are given in reference 19. Some results obtained using the various models are presented under "Results and Discussion" for comparative purposes.

The methods outlined thus far to evaluate the equilibrium absorption coefficients are applicable for hydrogen atoms and molecules. This is quite sufficient if no ablation mass injection is considered in the analysis. However, with ablation products in the shock layer, appropriate relations are needed to evaluate the continuum and line contributions to the absorption coefficient by these species. Information for obtaining the absorption cross section for the electronic band systems belonging to diatomic molecules is available in references 51 and 52. According to these references, the equilibrium absorption coefficient for a transition from level 0 to level 1 (higher level) is given by
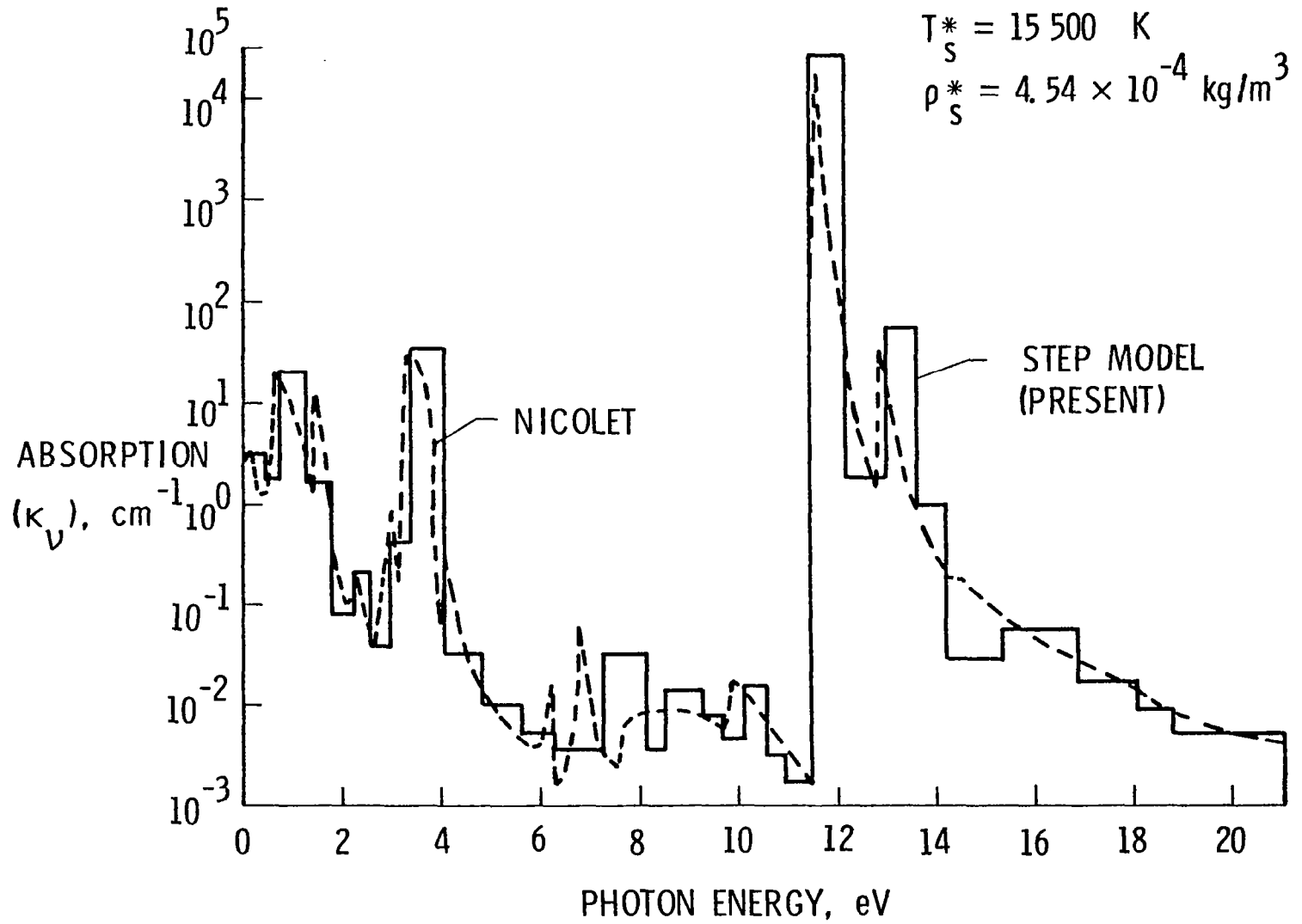
Figure 3. A 30-step model to approximate the absorption by Nicolet's detailed model (T_s = 15,500 K).

$$\kappa_\nu(0,1) = \sigma_\nu(0,1)\, n_o \tag{77}$$

where n_o is the number density of the absorbing species in level 0 and $\sigma_\nu(0,1)$ is the absorption cross section. This equilibrium absorption coefficient has to be corrected for the NLTE transition. The NLTE absorption coefficient is given by reference 47.

$$\kappa_\nu^*(\text{NLTE}) = \kappa_\nu \left\{ 1 - [(I_{\Delta\nu} B_{10} + A_{10} + C_{10})/(C_{01} + B_{01})] \right\} \tag{78}$$

where κ_ν is the frequency-dependent equilibrium absorption coefficient. By noting that

$$A_{10} = (2h\nu^3/c^2)\, B_{10} \tag{79a}$$

$$B_{10} = (g_0/g_1)\, B_{01} \tag{79b}$$

$$C_{10} = (B_{10}/B_{01})\, C_{01} \exp(h\nu/kT) \tag{79c}$$

$$\eta_c = 1/C_{10}, \quad \eta_r = 1/A_{10} \tag{79d}$$

equation (78) becomes

$$\kappa_\nu^*(\text{NLTE}) = \kappa_\nu \left\{ 1 - \left[1 + \eta\,(\eta/\delta) \int_{\Delta\nu} q_{R\nu}\, d\nu \,\right] \right.$$
$$\left. \cdot [(\eta/\delta) + \exp(-h\nu/kT)]^{-1} \right\} \tag{80}$$

This equation is used in evaluating the nonequilibrium absorption coefficients.

It is seen from equations (60), (63), and (80) that, for the evaluation of the nonequilibrium absorption coefficients and source function (and hence the nonequilibrium spectral radiative heat flux),

one must have information on the collisional relaxation time and the radiative lifetime of the excited states. The procedure for obtaining these is discussed in the next section.

RADIATIVE LIFETIMES AND COLLISIONAL PROCESSES FOR THE SHOCK-LAYER GASES

Introduction

For a gaseous medium in local thermodynamic equilibrium, information on the collisions between the various particles and their radiative lifetimes in the excited states is of little importance. To analyze the nonequilibrium phenomena, however, a quantitative study of collisions between various particles is necessary. This study need be extended only to those species whose collisional transition rates (under a given set of physical conditions) are comparable to their radiative transition rates. Nonequilibrium phenomena are important only under these conditions.

For Jovian entry conditions and for the case with no ablation from the probe surface, the NLTE effects are considered only for the hydrogen species in the shock layer. However, for the case of carbon-phenolic ablation injection, the C_2 molecules play a very important role in the radiation blockage. For this case, therefore, contributions of the C_2 molecules are also included in the NLTE analysis. A discussion of the radiative lifetimes and collisional relaxation times of various species considered for the NLTE analysis (in the shock-layer gas) is presented in this section.

Radiative Lifetimes of Excited States

The radiative lifetime η_r of an excited state is the inverse of the Einstein coefficient for spontaneous emission A_{10}, and this is given (refs. 53, 54) by

$$\eta_r = 1/A_{10} = (c^2/8\pi h\nu^3)/B_{01} \tag{81}$$

where B_{01} is the Einstein coefficient for absorption. By using the statistical relation for B_{01}, equation (81) is written as

$$\eta_r^{-1} = (8\pi\nu^2/c^3) \int_{\Delta\nu} \kappa_\nu \, d\nu \tag{82}$$

For the present study it is more appropriate to use the radiative lifetime in a different form. For a fully allowed electronic transition in the visible or near-ultraviolet region of the spectrum, the radiative lifetime is expressed in terms of the half-width of the spectral line (ref. 55) as

$$\eta_r = h/(2\pi b) \tag{83}$$

Upon inserting the numerical value for the Planck constant h (and converting from ergs to cm^{-1}), the value of η_r is found to be

$$\eta_r = (5.3 \times 10^{-12})/b \tag{84}$$

For a Stark-broadened hydrogen line of Lorentz shape, the value of the radiative lifetime is found to be 0.52×10^{-7} sec (ref 55). This value is used in the present study. It should be noted that the radiative lifetime is a function of frequency and, therefore, varies according to the various levels of energy transitions. Considering all radiative transition probabilities between different energy levels, it is found that the above-mentioned value of η_r corresponds to the shortest time between the ground level (with principal quantum number 2). Since the maximum nonequilibrium effect would correspond to this value of η_r, its use is justified in the present study.

There are eight known C_2-band systems in the 0.1- to 7.0-eV (0.2- to 1.2-μ) spectral region. The Swan band system, whose electronic transition is represented by $d^3\pi_g - a^3\pi_u$ (following the notation of ref. 55), is the strongest radiating system of the C_2 molecules. The Freymark band ($E'\Sigma_g^+ - A'\pi_u$) and the Mulliken band ($D'\Sigma_u^+ - x'\Sigma_g^+$) are the next important radiating systems of the C_2

molecules. Hence, the radiative lifetime of these band systems has to be determined first in order to evaluate their respective NLTE cross sections. For a molecule with an electronic transition, the radiative lifetime is related to the wavelength-dependent electronic F-number, the electronic transition moment, and the Einstein coefficient for spontaneous emission $A_{n'n''}$. The measured value for the electronic transition moment is available for the C_2 band systems (ref. 56). The electronic F-number is given in terms of the square of the transition moment $|R_e/ea_0|^2$ as

$$F_{el}(\lambda) = [(8\pi^2 m_e c/3he^2\lambda) \ \Sigma |R_e/ea_0|^2] \ /A \tag{85}$$

where

$$A = (2 - \sigma_{0,\Lambda''}) \ (2S'' + 1)$$

In the above discussions and relations, the superscript ' denotes the upper state and " the lower state, and S" represents the spin quantum number of the lower state. The quantity $\sigma_{0,\Lambda} = 1$ for $\Lambda = 0$ and $\sigma_{0,\Lambda} = 0$ for $\Lambda \neq 0$, and Λ is the resultant angular momentum of electrons. The electronic F-number is related to the band oscillator strength by

$$F_{v'v''} = F_{el} \ q_{v'v''} \tag{86}$$

where $q_{v'v''}$ is the Franck-Condon factor. Now, the radiative lifetime of the v' state can be expressed as

$$(\eta_r)^{-1} = A_{v'v''} = F_{v'v''} \ [(6.67 \times 10^{15})/\lambda^2] \ (g''/g') \tag{87}$$

Here, g' and g" are the degeneracies of the upper and lower levels respectively and g"/g' = 1. The value of $F_{v'v''}$ measured for the C_2-Swan (0,0) band is 6.5×10^{-3} (ref. 57). Upon substituting this

value of $F_{v'v''}$ and using equation (87), the radiative lifetime of the C_2-Swan $3\pi_g$ ($v' = 0$) state is found to be 8.0×10^{-7} sec. No measured value of the band oscillator strength $F_{v'v''}$ is available for the Freymark and Mulliken band system. However the values of the electronic transition moment are available for these bands; and, since $F_{v'v''}$ is directly proportional to the electronic transition moment, the radiative lifetime of the $E'\Sigma_g^+$ state of the Freymark (0,1) band is 1.5×10^{-6} sec and the $D'\Sigma_u^+$ of the Mulliken (0,0) band is 6.95×10^{-6} sec. These values are used in the majority of cases investigated in the present study. However, another set of values for the radiative lifetime of different bands is suggested in the literature (ref. 56). These are η_r(Swan) $= 1.25 \times 10^{-7}$ sec, η_r(Freymark) $= 4.67 \times 10^{-8}$ sec, and η_r(Mulliken) $= 8.77 \times 10^{-9}$ sec. These values are significantly different from those mentioned earlier. Because of this discrepancy, it is essential to investigate the influence of a different set of radiative lifetimes on the NLTE results. The following format, therefore, will be adapted for calculating the NLTE results in the presence of the **ablative** products in the shock layer:

NLTE (I):   based on η_r(Swan) $= 8 \times 10^{-7}$ sec

NLTE (II):   based on η_r(Swan) $= 1.25 \times 10^{-7}$ sec

NLTE (III):   based on the combined contributions of η_r(Swan) $= 8 \times 10^{-7}$, η_r(Freymark) $= 1.5 \times 10^{-6}$, and η_r(Mulliken) $= 6.95 \times 10^{-6}$ sec

NLTE (IV):   based on the combined contributions of η_r(Swan) $= 1.25 \times 10^{-7}$, η_r(Freymark) $= 4.67 \times 10^{-8}$, and η_r(Mulliken) $= 8.77 \times 10^{-9}$ sec

Collisional Relaxation Time

The collisional relaxation time is a strong function of temperature and pressure. At very high temperatures (associated with the ionization mechanism of hydrogen atoms), it is reasonable to assume that most of the NLTE transfer of radiation takes place before the ionization of the hydrogen atom. Hence, for the case with no ablation from the probe surface, it is quite sufficient to consider only the collisional process between H_2, and H and H^+. Collisions between two atoms or molecules may be of the first or second kind. In collisions of the first kind, the kinetic energy (KE) of translation goes into excitation energy according to the process

$$A + B + KE \rightarrow A + B^* \tag{88}$$

where A and B are two different (or same) species in the ground state and B^* is the species B in an excited state. Collisions of the second kind are more important for the NLTE analysis at high temperatures. This process is described by

$$A + B^* \rightarrow A + B + KE \tag{89}$$

Here, an atom or molecule gives up excitation energy by colliding with another partner. The time taken by a particle to reach the ground state from an excited state is the collisional relaxation time (ref. 58).

The collisional relaxation time for collisions between neutral particles (such as atoms and molecules) is given, in general, by the relation

$$\eta_c = 1/f_c = (n\Omega v)^{-1} \tag{90}$$

where f_c is the frequency of collisions (sec^{-1}), n is the number density of the colliding particles (cm^{-3}), Ω is the collisional cross section of the colliding particles (cm^2), and v is the most probable velocity of the particles (cm-sec^{-1}). By making use of the gas kinetic relations, the relaxation time (in sec) is expressed in terms of temperature as

$$\eta_c = 4\sqrt{2}\ \Omega\ (\pi m/8RT)^{1/2}\ (1/n) \tag{91}$$

where m is the mass of the colliding particles. Information on the collisional cross section for different colliding particles is available in references 9 and 59.

For an extensive study of the NLTE process, a detailed study of the various collisional processes between the particles (present in the radiation field) is necessary. All collisions which are effective in deactivating the excited particles must be considered in the analysis. Relaxation times for the case of collisions between neutral particles of the same kind (i.e. for H_2-H_2, C_2-C_2, H-H collisions) can be calculated using equation (91) with the appropriate values for collisional cross section and mass. On the other hand, the collisions between unlike particles with different masses and cross sections may be equally effective in removing the electronic excitation energy from these particles. In such cases, the effective collisional frequency is calculated by the method explained below. The collisions between H and H_2 are taken as an illustrative example; the procedure is the same for other combinations of molecules and atoms. The number of deactivation collisions made per second between H and H_2 is given by

$$Z(H - H_2) = 2n_{H_2}\ \Omega_E\ [2kT(m_{H_2} + m_H)/(\pi m_{H_2}\ m_H)]^{1/2} \tag{92}$$

where n_{H_2} is the number density of H_2 and m_{H_2} and m_H are the masses of a hydrogen molecule and atom respectively. The quantity Ω_E is the effective collisional cross section and is given by the expression

$$\Omega_E = [(\Omega_{H_2} + \Omega_H)/4] + [(\Omega_{H_2} \, \Omega_H)^{1/2}/2\pi] \qquad (93)$$

where Ω_{H_2} and Ω_H are the cross sections of H_2 and H respectively. Hence, the relaxation time (in sec) for H_2-H collisions is the reciprocal of the collisional frequency Z (H_2-H).

The combined relaxation time for self-collisions and collisions of different kind is given by reference 60.

$$1/n_c(COM) = X/[n_c(H-H)] + (1-X)/[n_c(H_2-H)] \qquad (94)$$

where X represents the mole fraction of hydrogen atoms. In the present study, collisions between H-H and H_2-H are considered in evaluating the combined relaxation time with no ablation injection in the shock-layer. Collisions between H_2-H_2 are neglected because the number density of H_2 is small compared to the number density of atomic hydrogen. Various collisional relaxation times obtained for different collisional processes (between the shock-layer species without ablative products) are shown in figure 4 as a function of temperature. With the ablation injection, the important species influencing the collisional deactivation process of the C_2 molecules are H_2, H, H^+, C_3, C, and e^-. The relaxation times obtained by using equations (91) to (94) for the C_2-C_2, H-H and combined collisions are shown in figure 5 as a function of temperature. The C_2-C_2, C_2-C, C_2-H, and H-H collisions represent the combined collisional process. The radiative lifetimes of the Swan (0,0), Freymark (0,1) and Mulliken (0,0) bands, corresponding to the case of n_r (III), are also shown in this figure.
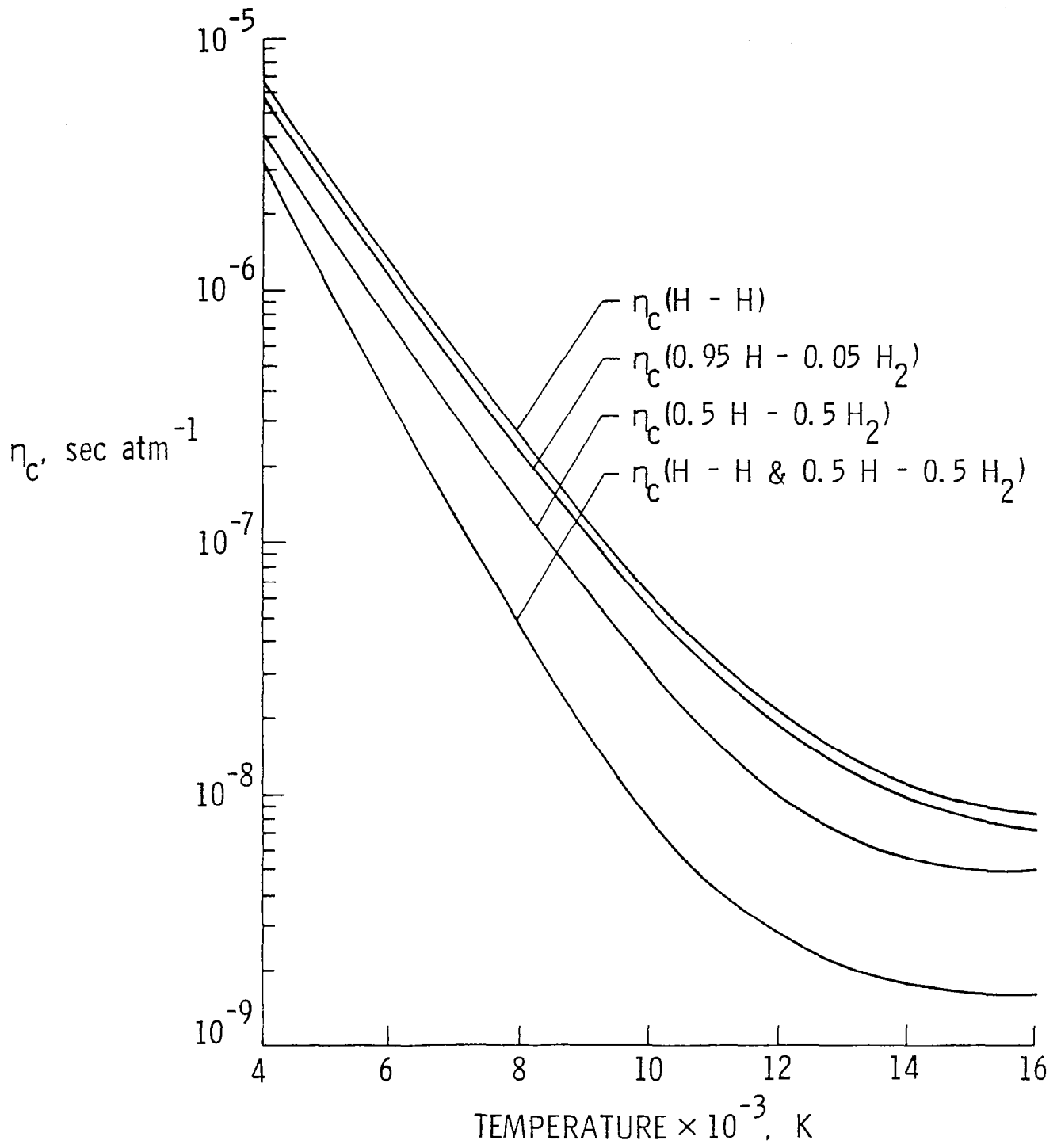
Figure 4. Collisional relaxation time for atomic and molecular hydrogen species.
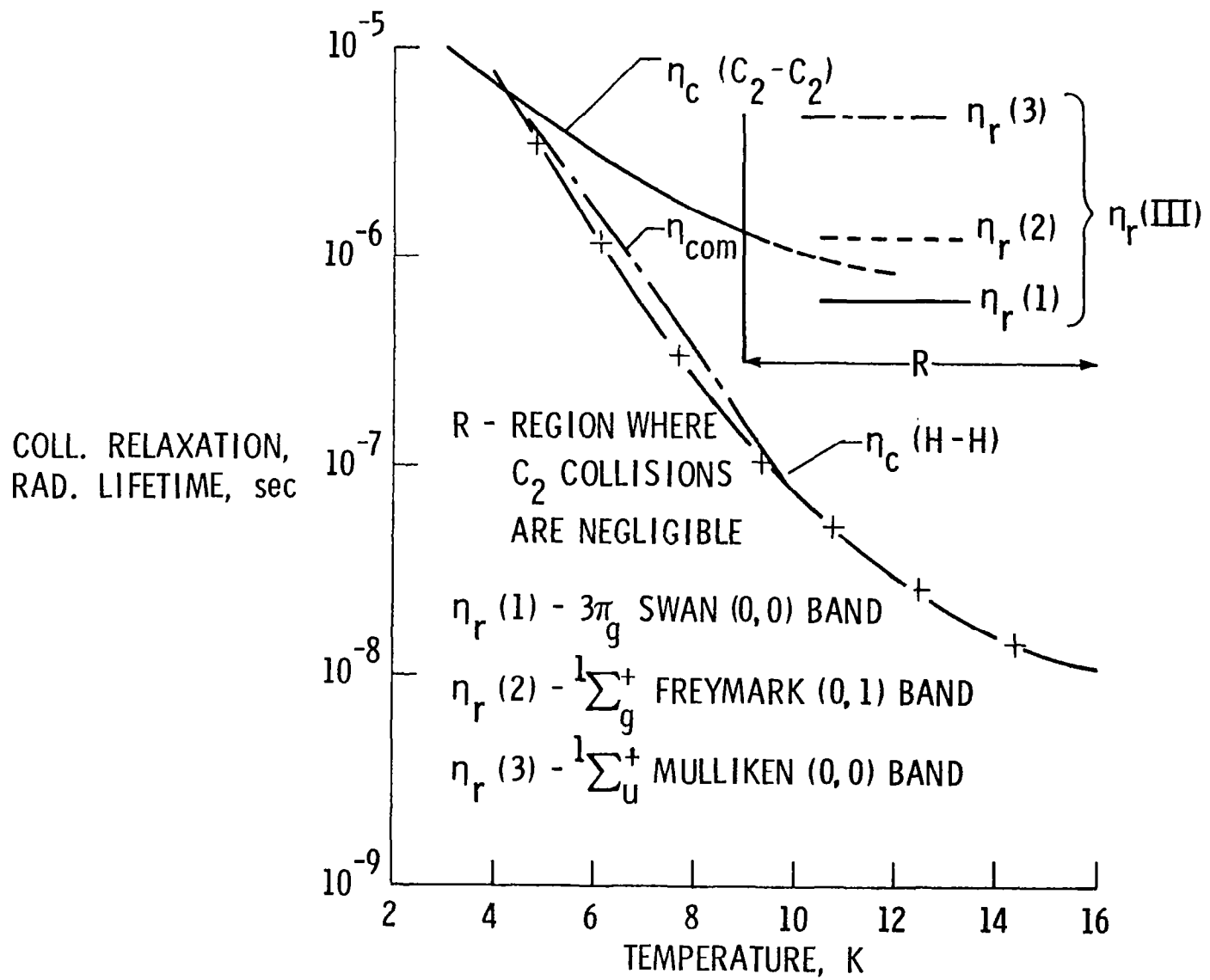
Figure 5. Variation of collisional relaxation time with temperature.

The rate of electronic deexcitation from an upper state to a lower state (by electron impact in a molecule) is given by

$$C_{nm} = [A(T/10{,}000)^r g_k]/(\overline{m}^5 \ \overline{n}^5)[(1/\overline{m}^2) - (1/\overline{n}^2)] \tag{95}$$

where $\overline{m}$ and $\overline{n}$ are the principal quantum numbers of the lower and upper states, respectively, and A is the excitation rate constant (different for different molecules). Due to the absence of e^- close to the wall, where the NLTE effect is more pronounced, deexcitation by electronic collisions is not considered. Here, only the collisional deactivation of C_2 by heavy particles is considered.

The collisional relaxation time for a hydrogen ion is given (ref. 61) by the relation:

$$\eta_c(H^+) = [m_i^{1/2}(3kT)^{3/2}]/(17.94 \ n_i e^4 Z^4 \ \ln\Lambda) \tag{96}$$

where m_i represents mass of the ions, n_i is the number density of ions, and Λ is a parameter which is expressed as a function of temperature by

$$\Lambda = (k^3 T^3/\pi n_i)^{1/2} \tag{97}$$

For hydrogen ions, equation (96) may be simplified further as

$$\eta_c(H^+) = (22.8 \ T^{3/2})/(n_i \ \ln\Lambda) \tag{98}$$

where T is the heavy particle temperature in K. The collisional relaxation times for the hydrogen ions are shown in figure 6 for different number densities and temperature values.
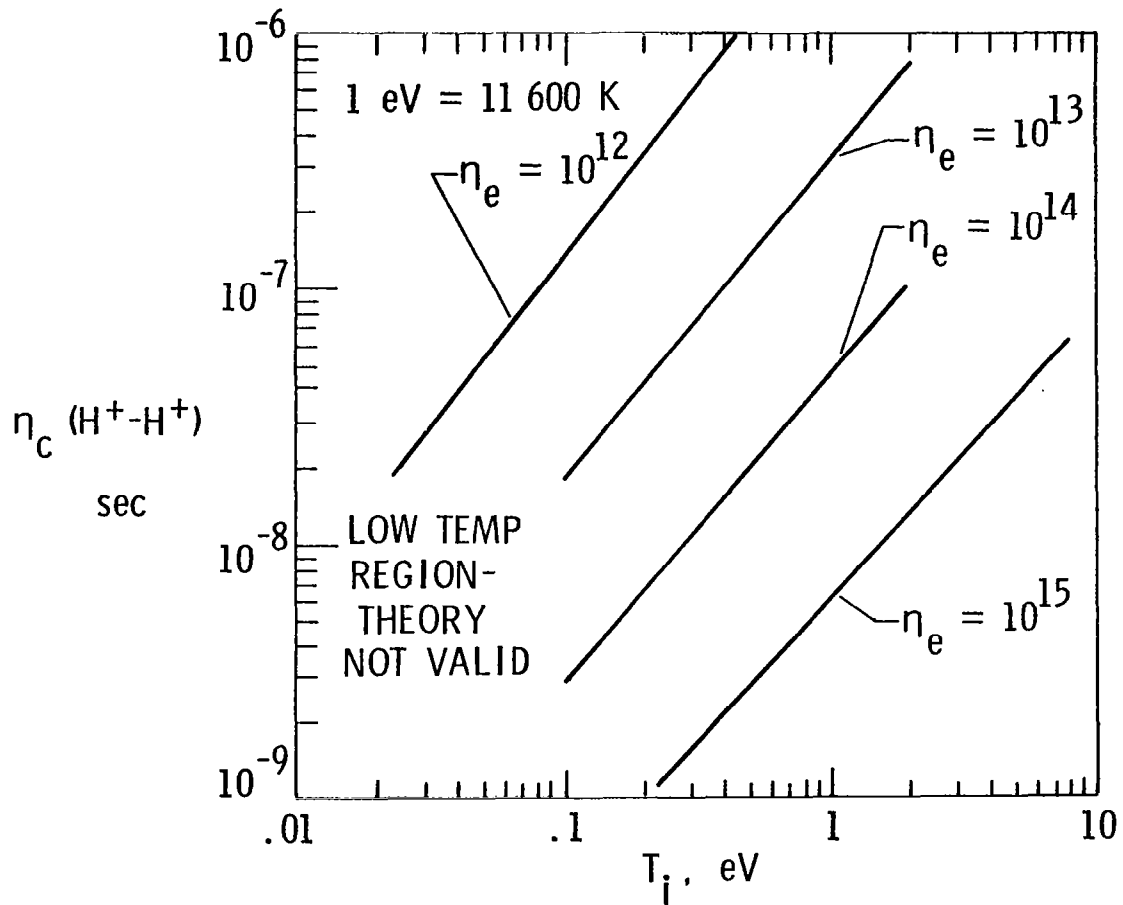
Figure 6. Collisional relaxation time for hydrogen ions.

THERMODYNAMIC AND TRANSPORT PROPERTIES

Thermodynamic properties for specific heat, enthalpy, and free energy, and transport properties for viscosity and thermal conductivity are required for each species considered in the shock layer. The general expressions for total enthalpy, specific enthalpy, and specific heat at constant pressure are given respectively by

$$H_T = h + (u^2 + v^2)/2 \tag{99}$$

$$h = \Sigma C_i \, h_i \tag{100}$$

$$C_p = \Sigma C_i \, C_{pi} \tag{101}$$

In the present study, values for the thermodynamic and transport properties are obtained by using polynomial curve fits. The expressions for h_i and C_{pi} are given (refs. 62, 63) by

$$h_i = RT \, [A + (B/2)T + (C/3)T^2 + (D/4)T^3 + (E/5)T^4$$

$$+ (F/6)T^5 + (G/7)T^6] \tag{102}$$

$$C_{pi} = R \, [A + BT + CT^2 + DT^3 + ET^4 + FT^5 + GT^6] \tag{103}$$

where R is the universal gas constant and T is the equilibrium fluid temperature in the shock layer. For different species i under the present investigation, the polynomial coefficients A, B, . . . G are given in tables 2 and 3. Equations (99) to (101) are used to calculate the enthalpy variation in the shock layer.

Table 2. Coefficients for evaluation of the specific heat at
constant pressure for hydrogen/helium species.

Species[*]	Coefficients						
	A	B	C	D	E	F	G
H	.2500E+01[1]					.2547E+05	-.4601E+00
	.2500E+01[2]					.2547E+05	-.4601E+00
	.2475E+01[3]	.7366E-04	-.2537E-07	.2386E-11	-.4551E-16	.2523E+05	-.3749E+00
H_2	.3057E+01[1]	.2676E-02	-.5809E-05	.5521E-08	-.1812E-11	-.9889E+03	-.2299E+01
	.3100E+01[2]	.5111E-03	.5264E-07	-.3491E-10	.3694E-14	-.8773E+03	-.1962E+01
	.3363E+01[3]	.4656E-03	-.5127E-07	.2802E-11	-.4905E-16	-.1018E+04	-.3716E+01
H^+	.2500E+01[1]					.1840E+06	-.1153E+01
	.2500E+01[2]					.1840E+06	-.1153E+01
	.2500E+01[3]					.1840E+06	-.1153E+01
HE	.2500E+01[1]					-.7453E+03	.9153E+00
	.2500E+01[2]					-.7453E+03	.9153E+00
	.2500E+01[3]	0.0	0.0	0.0	0.0	-.7453E+03	.9153E+00
HE^+	.2500E+01[1]					.2853E+06	.1608E+01
	.2500E+01[2]					.2853E+06	.1608E+01
	.2500E+01[3]					.2853E+06	.1608E+01
E^-	.2500E+01[1]					-.7453E+03	-.1173E+02
	.2500E+01[2]					-.7453E+03	-.1173E+02
	.2508E+01[3]	-.-332E-05	.1364E-08	-.1094E-12	.2934E-17	-.7450E+03	-.1208E+02

[*]Each species has three sets of values valid over three different temperature range; these are

1 > 300 K   2 > 1000 K   3 > 6000 K

Table 3. Coefficients for evaluating the specific heat at
constant pressure for the ablative products.

| Species | Coefficients | | | | | | |
	A	B	C	D	E	F	G
C H $_4$	.4968E+01	.1727E-01	-.2994E-04	.3246E-07	-.1366E-10	.7545E+05	-.8769E+00
	.6531E+01	.6506E-02	-.2251E-05	.3329E-09	-.1721E-13	.7535E+05	-.7446E+01
	.6531E+01	.6506E-02	-.2251E-05	.3329E-09	-.1721E-13	.7535E+05	-.7446E+01
0	.2946E+01	-.1638E-02	.2421E-05	-.1602E-05	-.1602E-12	.3890E-05	.2963E+01
	.2542E+01	-.2755E-04	-.3102E-08	.4551E-11	-.4368E-15	.2923E+05	.4920E+01
	.2546E+01	-.5952E-04	.2471E-07	-.2798E-11	.9380E-16	.2915E+05	.5049E+01
0 $_2$	.3526E+01	-.1878E-02	.7055E-05	-.6764E-08	.2155E-11	-.1047E+04	.4305E+01
	.3621E+01	.7361E-03	-.1965E-06	.3620E-10	-.2894E-14	-.1201E+04	.3615E+01
	.3721E+01	.4254E-03	-.2835E-07	.6050E-12	-.5186E-17	-.1044E+04	.3254E+01
0 $^+$	.2498E+01	.1141E-04	-.2976E-07	.3224E-10	-.1237E-13	.1879E+06	.4386E+01
	.2506E+01	-.1446E-04	.1244E-07	-.4685E-11	.6554E-15	.1879E+06	.4347E+01
	.2944E+01	-.4108E-03	.9156E-07	-.5848E-11	.1190E-15	.1879E+06	.1750E+01
CO	.3790E+01	-.1619E-02	.3692E-05	-.2031E-08	.2395E-12	-.1435E+05	.2955E+01
	.2984E+01	.1489E-02	-.5789E-06	.1036E-09	-.6935E-14	-.1424E+05	.6347E+01
	.3366E+01	.8027E-03	-.1968E-06	.1940E-10	-.5549E-15	-.1434E+05	.4263E+01
CO $_2$	.2400E+01	.8735E-02	-.6607E-05	.2002E-08	.6327E-15	-.4837E+05	.9695E+01
	.4460E+01	.3098E-02	-.1239E-05	.2274E-09	-.1552E-13	-.4986E+05	-.9863E+00
	.4413E+01	.3192E-02	-.1298E-05	.2415E-09	-.1674E-13	-.4894E+05	-.7288E+00

Table 3. (concluded).

Species	A	B	C	D	E	F	G
C	.2532E+01	-.1588E-03	.3068E-06	-.2677E-09	.8748E-13	.8524E+05	.4606E+01
	.2581E+01	-.1469E-03	.7438E-07	-.7948E-11	.5890E-16	.8521E+05	.4312E+01
	.2141E+01	.3219E-03	-.5498E-07	.3604E-11	-.5564E-16	.8542E+05	.6874E+01
C_2	.7451E+01	-.1014E-01	.8587E-05	.8732E-09	-.2442E-11	.9891E+05	-.1584E+02
	.4043E+01	.2057E-03	.1090E-06	-.3642E-10	.3412E-14	.9970E+05	.1277E+01
	.4026E+01	.4857E-03	-.7026E-07	.4666E-11	-.1142E-15	.9787E+05	.1090E+01
C_3	.5564E+01	-.4687E-02	.1533E-04	-.1509E-07	.5100E-11	.9926E+05	-.2000E+01
	.4394E+01	.2964E-02	-.1541E-05	.3796E-09	-.3010E-13	.9926E+05	.2970E+01
	.2213E+02	-.1759E-01	.5565E-05	-.6758E-09	.2925E-13	.9423E+05	-.1021E+03
C^+	.2593E+01	-.4068E-03	.6892E-06	-.5266E-09	.1508E-12	.2166E+06	.3895E+01
	.2511E+01	-.1735E-04	.9504E-08	-.2218E-11	.1862E-15	.2166E+06	.4286E+01
	.2528E+01	.4869E-05	-.7026E-08	.1134E-11	-.3476E-16	.2168E+06	.4139E+01
C_2H	.2649E+01	.8491E-02	-.9816E-05	.6537E-08	-.1735E-11	.5627E+05	.7689E+01
	.4420E+01	.2211E-02	-.5929E-06	.9419E-10	-.6852E-14	.5583E+05	-.1158E+01
	.5307E+01	.8966E-03	-.1378E-06	.9251E-11	-.2278E-15	.5809E+05	-.5288E+01
C_2H_2	.1410E+01	.1905E-01	-.2450E-04	.1539E-07	-.4134E-11	.2618E+05	.1139E+02
	.4575E+01	.5123E-02	-.1745E-05	.2867E-09	-.1795E-13	.2560E+05	-.3573E+01
	.6789E+01	.1503E-02	-.2295E-06	.1534E-10	-.3763E-15	.2590E+05	-.1539E+02
C_3H	.3344E+01	.1068E-01	-.1331E-04	.1338E-07	-.5698E-11	.6258E+05	.6000E+01
	.3877E+01	.6724E-02	-.2605E-05	.4416E-09	-.2708E-13	.6256E+05	.3826E+01
	.3877E+01	.6724E-02	-.2605E-05	.4416E-09	-.2708E-13	.6256E+05	.3826E+01

1 > 300 K   2 > 1000 K   3 > 6000 K

For the shock-layer gas, the mixture viscosity and thermal conductivity are obtained by using the semi-empirical formulas of Wilke (ref. 64) as;

$$\mu = \sum_{i=1}^{N} [x_i \mu_i / (\sum_{j=1}^{N} x_j \phi_{ij})] \tag{104}$$

$$K = \sum_{i=1}^{N} [x_i K_i / (\sum_{j=1}^{N} x_j \phi_{ij})] \tag{105}$$

where

$$\phi_{ij} = [1 + (\mu_i/\mu_j)^{1/2} (M_j/M_i)^{1/4}]^2 / \{\sqrt{8} [1 + (M_i/M_j)]\}^{1/2} \tag{106}$$

and M_i is the molecular weight of species i. For hydrogen/helium species, specific relations for viscosity and thermal conductivity are given in reference 65. The viscosity of H_2 and He, as a function of temperature, can be obtained from reference 35 as

$$\mu_{H_2} = (0.66 \times 10^{-6})(T)^{3/2}/(T + 70.5), \text{ N sec m}^{-2} \tag{107}$$

$$\mu_{He} = (1.55 \times 10^{-6})(T)^{3/2}/(T + 97.8), \text{ N sec m}^{-2} \tag{108}$$

The specific relations for viscosity of other species are given in reference 35. The general relation for the thermal conductivity, based on equation (105), is given (ref. 66) as

$$K_i = A + BT \tag{109}$$

The coefficients A and B for different species used in this study are given in table 4.

Table 4. Coefficients for thermal conductivity in equation (109).

| | COEFFICIENTS | |
Species	A	B
H	.2496E-04	.5129E-07
H	.3211E-04	.5344E-07
H^+	.2600E-03	
HE	.2038E-04	.3249E-07
HE^+	.2600E-03	
E^-	.2600E-03	
C	.2506E-04	.7479E-08
C	.8590E-05	.6233E-08
C	.6300E-05	.5804E-08
C^+	.2600E-03	
C H	.1126E-04	.7439E-08
C H	.1126E-04	.7439E-08
C H	.6300E-05	.5804E-08
C H	.6300E-05	.5804E-08
O	.1250E-04	.7092E-08
O	.1019E-04	.4901E-08
O^+	.2600E-03	
CO	.8590E-05	.6233E-08
CO	.8590E-05	.6233E-08

The heat transfer to the wall due to conduction and diffusion is referred to here as the convective heat flux and is given in terms of the thermal conductivity and viscosity as

$$q_c = -\varepsilon^2 [K(\partial T/\partial n) + (\mu Le/Pr) \sum_{i=1}^{Ns} (\partial C_i/\partial n)h_i]$$ (110)

The values for the Prandtl number Pr and the Lewis number Le are taken as 0.74 and 1.1, respectively. It should be noted that equation (110) is similar to equation (23).

METHOD OF SOLUTION

The numerical procedures for solving the inviscid and viscous flow equations are discussed in detail in references 5 and 29. Tiwari and Szema applied the method outlined in reference 5 in their study of the effects of precursor heating on chemical and radiative nonequilibrium viscous flow around a Jovian entry body (ref. 8). A modified form of this procedure is used in this study to obtain solutions of the shock-layer equations under both the equilibrium and nonequilibrium radiative heat transfer conditions. In this method, a transformation is applied to the viscous shock-layer equations in order to simplify the numerical computations. In this transformation most of the variables are normalized with their local shock values. The transformed variables are

$$\eta = n/n_s \qquad \overline{p} = P/P_s \qquad \overline{\mu} = \mu/\mu_s$$

$$\xi = s \qquad \rho = \rho/\rho_s \qquad \overline{k} = k/k_s$$

$$\overline{u} = u/u_s \qquad \overline{T} = T/T_s \qquad \overline{C}_p = C_p/C_{ps}$$

$$\overline{v} = v/v_s \qquad \overline{H} = H/H_s \qquad \text{(111)}$$

The transformation relating the differentials are

$$\partial/\partial s \; (\;) = \partial/\partial\xi \; (1/n_s)(dn_s/d\xi)\eta \; \partial/\partial\eta \; (\;) \qquad \text{(112a)}$$

and

$$\partial/\partial n \; (\;) = 1/n_s \; \partial/\partial_\eta(\;), \quad \partial^2/\partial n^2 = 1/n_s^2 \; \partial^2/\partial\eta^2 \; (\;) \qquad \text{(112b)}$$

The transformed equation can be expressed in a general form as

$$(\partial^2 W/\partial \eta^2) + (a_1 \partial W/\partial \eta) \cdot + (a_2 W) + (a_3) + (a_4 \partial W/\partial \xi) = 0 \tag{113}$$

The quantity $\overline{W}$ represents $\overline{u}$ in the x-momentum equation, $\overline{T}$ in the temperature energy equation, $\overline{H}$ in the enthalpy energy equation, and C_i in the species continuity equations. The coefficients a_1 to a_4 are given in reference 5. With radiation included in the study, the coefficient a_3 is different from the expression given in reference 5. The modified value for the a_3 in the enthalpy energy equation is

$$a_3 = \frac{Pr_s \overline{Pr}_s n_s^2}{\mu_s \overline{\mu} H_s} \left[\frac{1}{n_s} \left(\frac{\partial \Psi}{\partial \eta} \right) + \left(\frac{\kappa}{1 + n_s \eta \kappa} + \frac{\cos \theta}{r + n_s \cos \theta} \right) \Psi \right]$$

$$+ \frac{n_s Pr P_s v_s \overline{v}}{\varepsilon^2 \mu_s \overline{\mu} H_s} \left(\frac{\partial p}{\partial \eta} \right) - \frac{n_s \overline{Pr} Pr_s}{\varepsilon^2 \mu_s H_s \overline{\mu}} \left[\frac{1}{n_s} \left(\frac{\partial q_R}{\partial \eta} \right) \right.$$

$$\left. + q_R \left(\frac{\kappa}{1 + n_s \eta \kappa} + \frac{\cos \theta}{r + n_s \cos \theta} \right) \right] \tag{114}$$

where

$$\Psi = \frac{\mu s}{n_s Pr_s} \left[\left(\frac{0.1 \overline{\mu}}{Pr} \right) \sum_{i=1}^{N} h_i \left(\frac{\partial C_i}{\partial \eta} \right) + \frac{u_s^2 \overline{\mu} \overline{u}}{\overline{Pr}} (Pr_s \overline{Pr} - 1) \frac{\partial \overline{\mu}}{\partial \eta} \right]$$

$$- \frac{\mu_s \mu_s^2 \kappa \overline{\mu} u^2}{1 + n_s \eta \kappa} \tag{115}$$

other transformed equations are the same as given in reference 5.

The surface boundary conditions in terms of transferred variables are

$$\overline{\mu} = 0, \quad \overline{v} = 0, \quad \overline{T} = \overline{T}_w \tag{116}$$

62

The transformed shock conditions are found to be

$$\overline{u} = \overline{v} = \overline{T} = \overline{H} = \overline{\rho} = \overline{p} = 1 \tag{117}$$

at $n = 1$.

The second-order partial differential equations as expressed by equation (113), along with the surface boundary and shock conditions, are solved by employing an implicit finite-difference scheme. The procedure is discussed briefly in the Appendix where flow diagrams for specific computations are also provided.

RESULTS AND DISCUSSION

Introduction

The results obtained in the present study extend over a wide
range of free-stream and flow conditions and probe shapes. The
basic shapes considered for the entry probes are sphere cones,
hyperboloids and ellipsoids. Most results have been obtained
for the entry conditions (i.e., the free-stream conditions at dif-
ferent entry altitudes) given in table 1. However, some specific
results have also been obtained for other entry conditions. The
shock-layer gas has been assumed to be in chemical equilibrium for
the entire study. Different spectral models for radiative transfer
in the gas have been considered, and various results obtained by
these models are compared. The NLTE analysis was first carried out
by considering only the hydrogen/helium species in the shock-layer
gas. Later, the contributions of ablative products were also included
in the NLTE analysis. Thus, in accordance with the four areas of
this study, the results are presented in the following four subsections:
(1) significance of radiation models on the flow-field solutions,
(2) influence of NLTE radiation without ablation injection, (3)
importance of NLTE radiation with ablation injection, and (4) effect
of probe shape change on the flow phenomena. The physical model
and flow conditions for which the results were obtained are given
in each subsection.

Significance of Radiation Models on the Flow-Field Solutions

By employing the three different absorption models discussed
under "Radiative Transport Models" (subsection titled "Spectral
Model for Gaseous Absorption") results were obtained for the flow-
field variables and the wall radiative heat flux distribution for
different entry conditions and body configurations. Inviscid as
well as viscous results were obtained for a 55-degree half angle
sphere cone, while only viscous results were obtained for a 50-
degree hyperboloid. Comparison of inviscid and viscous results

is presented for a 55-degree sphere cone entering the Jovian atmosphere at an altitude of Z = 116 km. Next, a series of viscous results is presented for the 55-degree sphere cone at different entry conditions. Finally, viscous results for a 50-degree hyperboloid are presented.

Comparison of inviscid and viscous results.- Inviscid and viscous results obtained by employing the detailed and 30-step radiation models are compared in this subsection. The temperature distribution along the stagnation streamline is illustrated in figure 7(a). The agreement between inviscid and viscous results is seen to be fairly good except near the body, where viscous boundary-layer effects are predominant [see fig. 7(b)]. The difference between the detailed and 30-step model results is lower for the inviscid case than the viscous case. This is due to relatively higher temperature across the shock-layer for the inviscid analysis. As pointed out earlier, the step model is more accurate at higher temperatures.

The shock standoff distance as a function of body location is illustrated in figure 8. The first three curves illustrate the inviscid results for the three different radiation models. The fourth curve, obtained by employing Nicolet's detailed radiation model, is for the viscous case, and is drawn here for comparison. The shock standoff distance is slightly larger for the present 30-step model as compared with the results of the detailed and Sutton's 58-step models. Although the difference between inviscid and viscous results is seen to be quite small, use of the viscous analysis is recommended for more realistic and accurate calculations.

Results of radiative heating along the body are illustrated in figure 9. While inviscid results are seen to be slightly higher at the stagnation point, viscous results are relatively higher at other body locations (up to $s^*/R_N^* = 0.6$). This is a direct consequence of viscous boundary-layer effects. A discussion of viscous results for different radiation models follows.
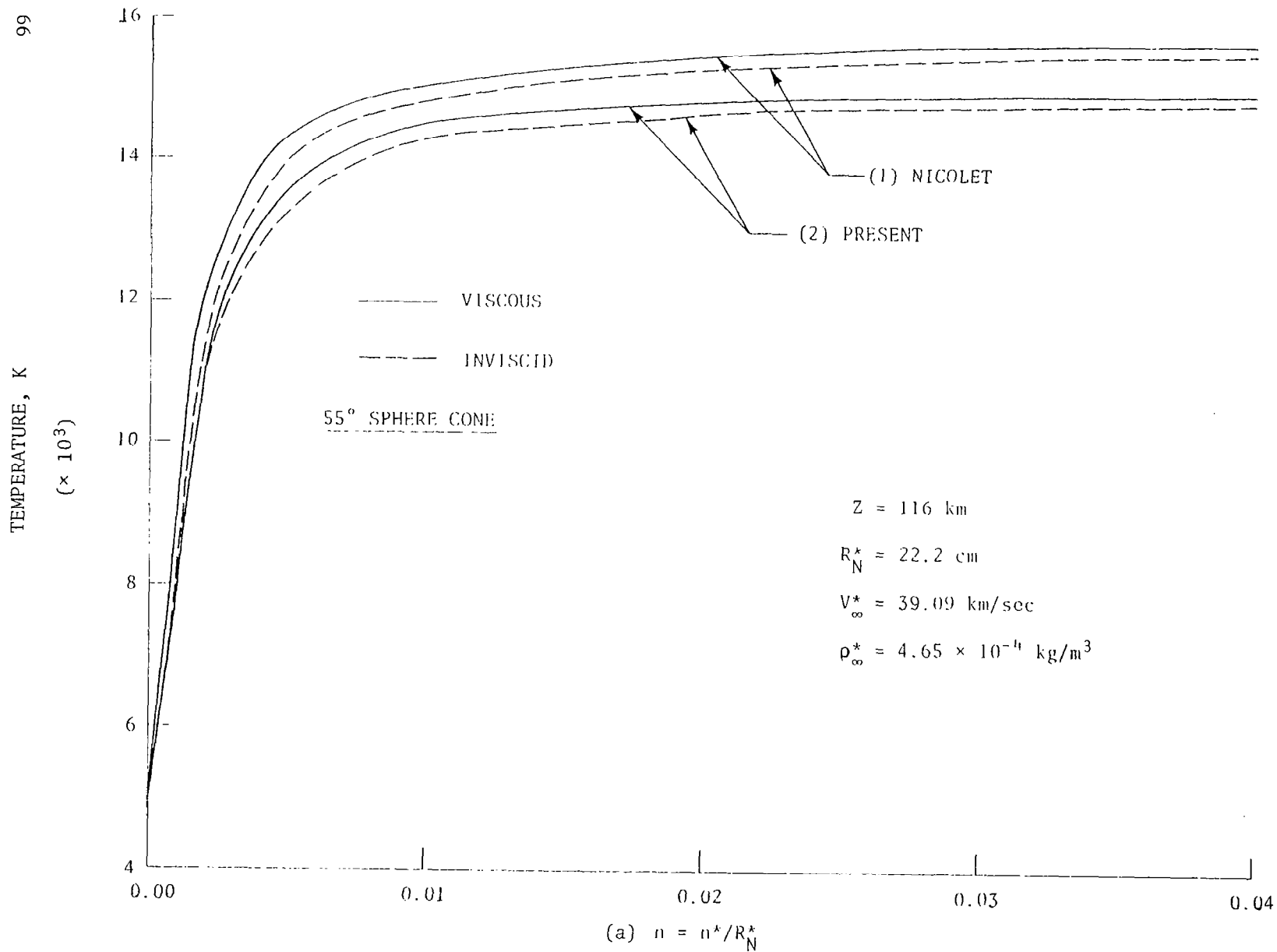
Figure 7.   Temperature distribution along the stagnation streamline for inviscid and viscous
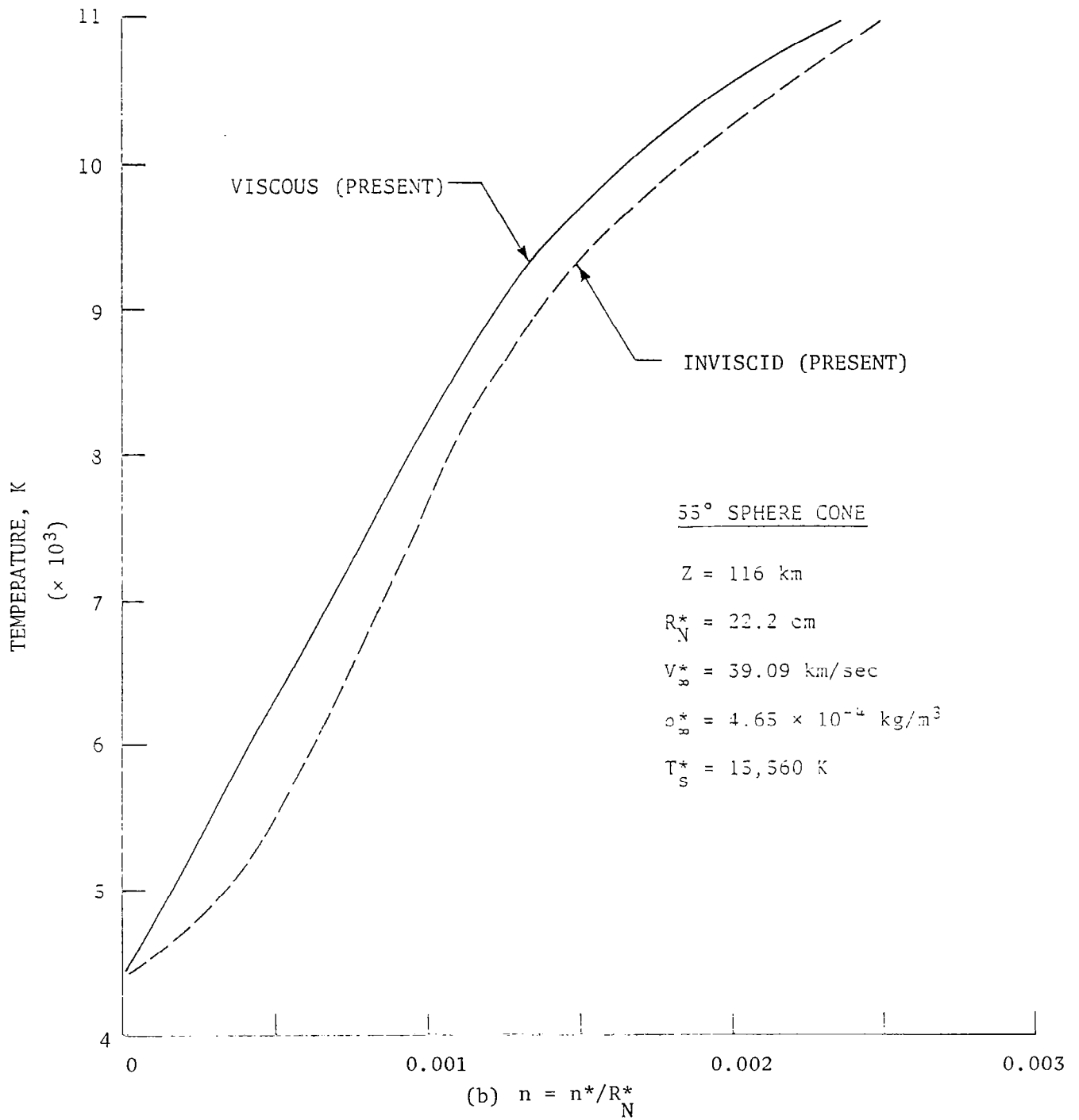analysis (55° sphere cone, Z = 116 km).   (Continued)

Figure 7. (Concluded).

0.20

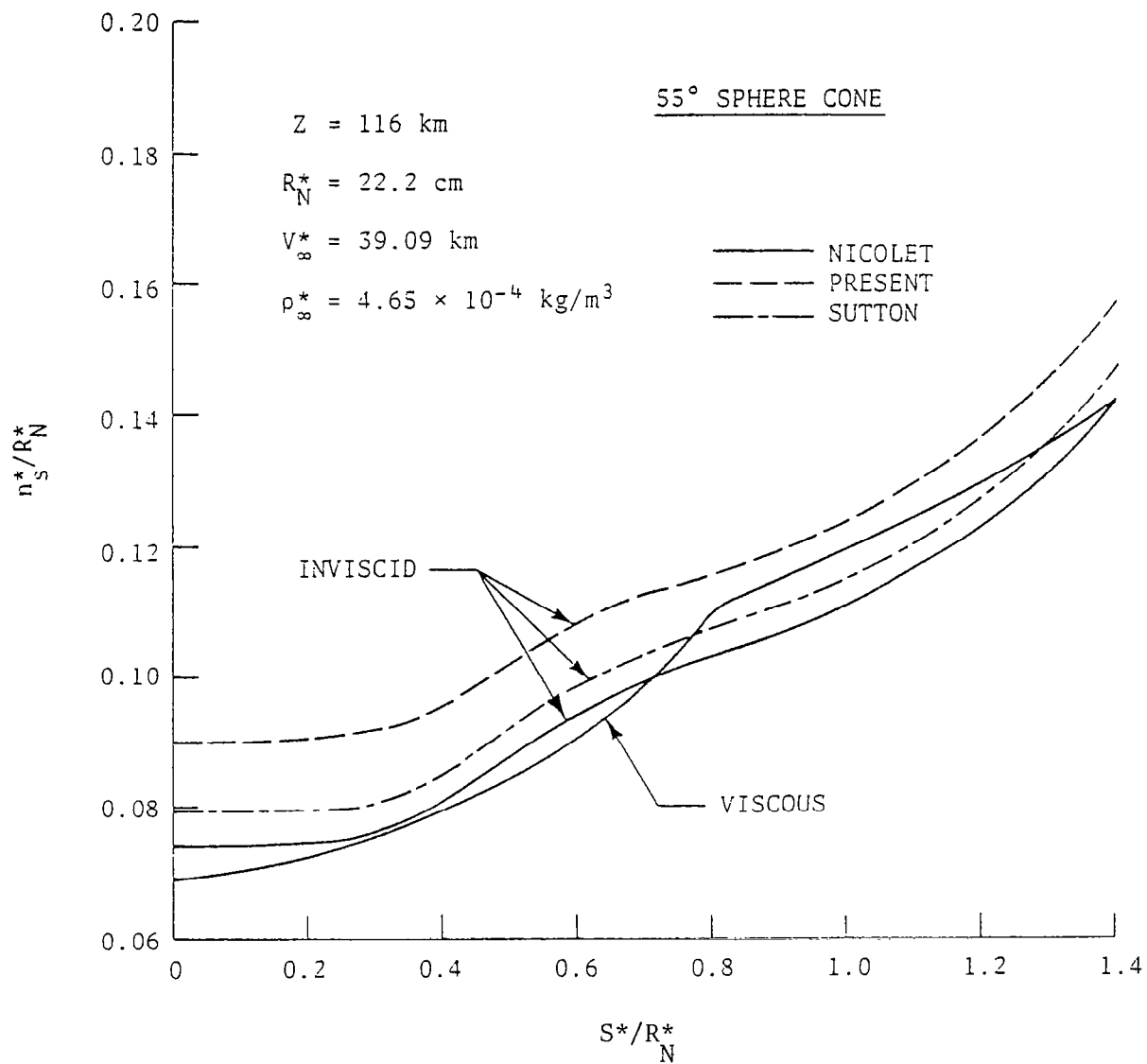0.18

0.16

0.14

0.12

0.10

0.08

0.06

n_S^*/R_N^*

55° SPHERE CONE

Z = 116 km

$R_N^* = 22.2$ cm

$V_\infty^* = 39.09$ km

$\rho_\infty^* = 4.65 \times 10^{-4}$ kg/m^3

——————— NICOLET
— — — — PRESENT
—·—·—·— SUTTON

INVISCID

VISCOUS

0   0.2   0.4   0.6   0.8   1.0   1.2   1.4

S^*/R_N^*

Figure 8.   Shock standoff variation with distance along the
body surface for inviscid and viscous analysis
(55° sphere cone, Z = 116 km).
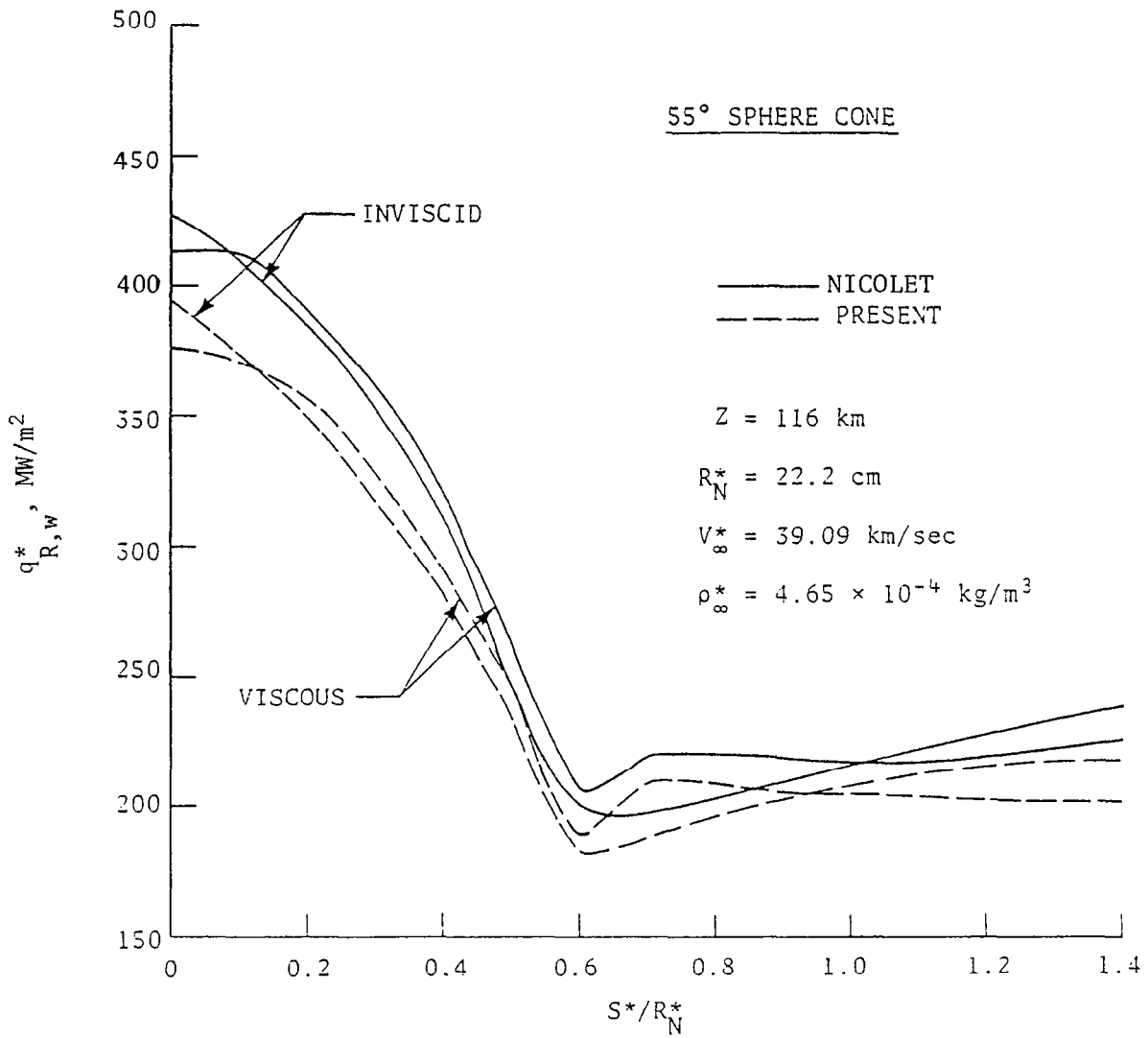
Figure 9.   Radiative heating along the body for inviscid and viscous
analysis (55° sphere cone, Z = 116 km).

Viscous results for a 55-degree sphere cone. - Viscous results
for a 55-degree cone (with a nose radius of 22.2 cm) for different
entry conditions are now presented. Results of various radiation
models are compared in order to establish the validity of the present
30-step radiation model.

In the shock layer, the temperature distribution along the
stagnation streamline is illustrated in figure 10 for two different
free-stream (density) conditions. It is found that the present 30-
step model underpredicts the shock-layer temperature by a maximum
of 11 percent in comparison to Nicolet's detailed model and by about
4.5 percent when compared with Sutton's 58-step model. For free-
stream conditions resulting in higher shock temperature, the agreement
between the results is even better. This is because the higher
temperature absorption spectrum can be approximated accurately
by the present step-model.

From the results presented in figures 7 and 10, it is noted
that there exists a steep temperature gradient in the regions close
to the body. At locations about five times the nose radius (normal
to the body), only a slight variation in the shock-layer temperature
is noticed. This fact was utilized in dividing the shock-layer into
different temperature zones for evaluating the absorption coefficient.
In a preliminary study, two methods were used to account for the
temperature dependence of the absorption coefficient. In the
first method, the absorption coefficient was calculated at the
shock temperature T_s^*. This value was used in analyzing the flow
field in the entire shock layer. Results obtained by this method
are designated here as "present-approximate" results. In the second
method, the shock-layer is divided into three different temperature
zones, two of which are closer to the body (because of the steep
gradient near the body). For each temperature zone, a different
30-step model for absorption is obtained. These are read as input
in the computer program while evaluating the flow variables in the
particular temperature zone. Results obtained by this method are
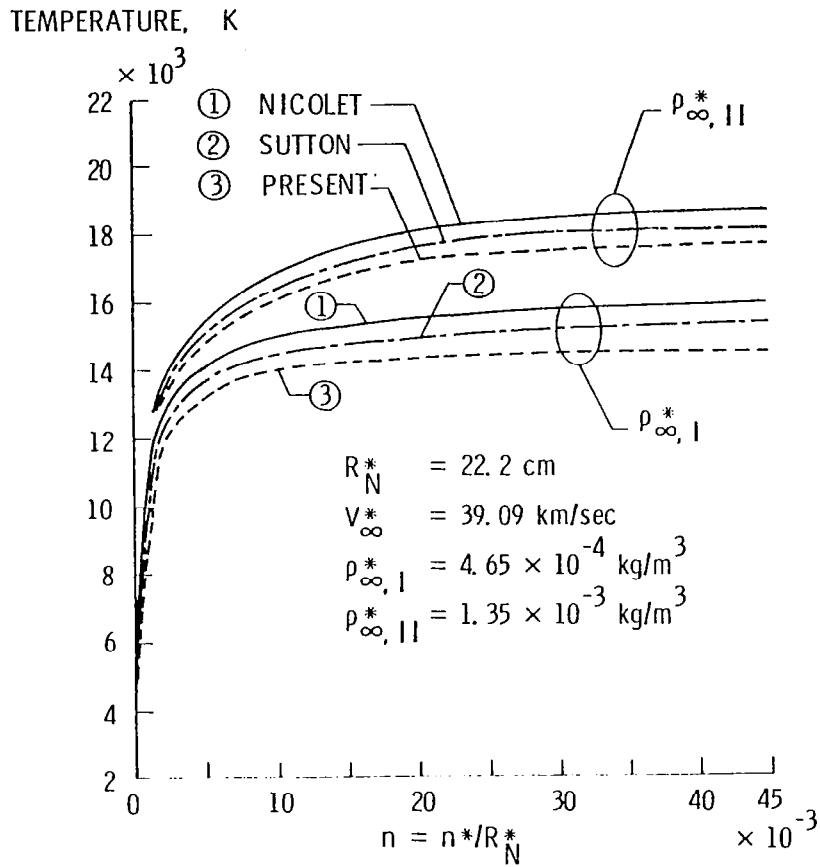denoted here as "present" results.

Figure 10. Temperature distribution along the stagnation streamline for two different free-stream densities (55° sphere cone).

The variation in temperature just behind the shock (at location $n = 0.05$) with distance along the body surface is illustrated in figure 11 for entry conditions at $Z = 116$ km. The results of the present model are found to be about six percent lower than the results of Nicolet's model. This difference is seen to be fairly uniform along the body.

Figure 12 shows the shock standoff variation with distance along the body surface for entry conditions at $Z = 116$ km. Results of Sutton's model are found to be in general agreement with the results of Nicolet's model. The present model is seen to overestimate the results by a maximum of 8.6 percent when compared with the results of Nicolet's model. This is mainly because the present model underpredicts the shock-layer density.

The radiative heating rate along the body surface is illustrated in figures 13 and 14 for different entry conditions. As would be expected, in all cases, the maximum heating occurs at the stagnation point. For $Z = 116$ km, results presented in figure 13 show that the present model underpredicts the heating rate by a maximum of 13.6 percent when compared with Nicolet's model. For the case of higher free-stream density (and hence a higher shock temperature), differences in the results of the present and other models are seen to be smaller. Figure 14 shows the results of radiative heating for 131-km entry conditions. For this higher altitude, the heat transferred to the body is lower because of lower free-stream density and pressure. For this case, differences in the results of the present and Nicolet's model are seen to be slightly higher.

Viscous results for a 50-degree hyperboloid. - Viscous results for a 50-degree hyperboloid (with a nose radius of 22.2 cm) are presented in this subsection for different entry conditions. The temperature distribution in the shock layer (along the stagnation streamline) is illustrated in figure 15 for entry conditions at $Z = 116$ km. The results of the three radiation models are seen to follow the same general trend as for the 55-degree sphere cone. A maximum difference of about 4.5 percent is seen between the
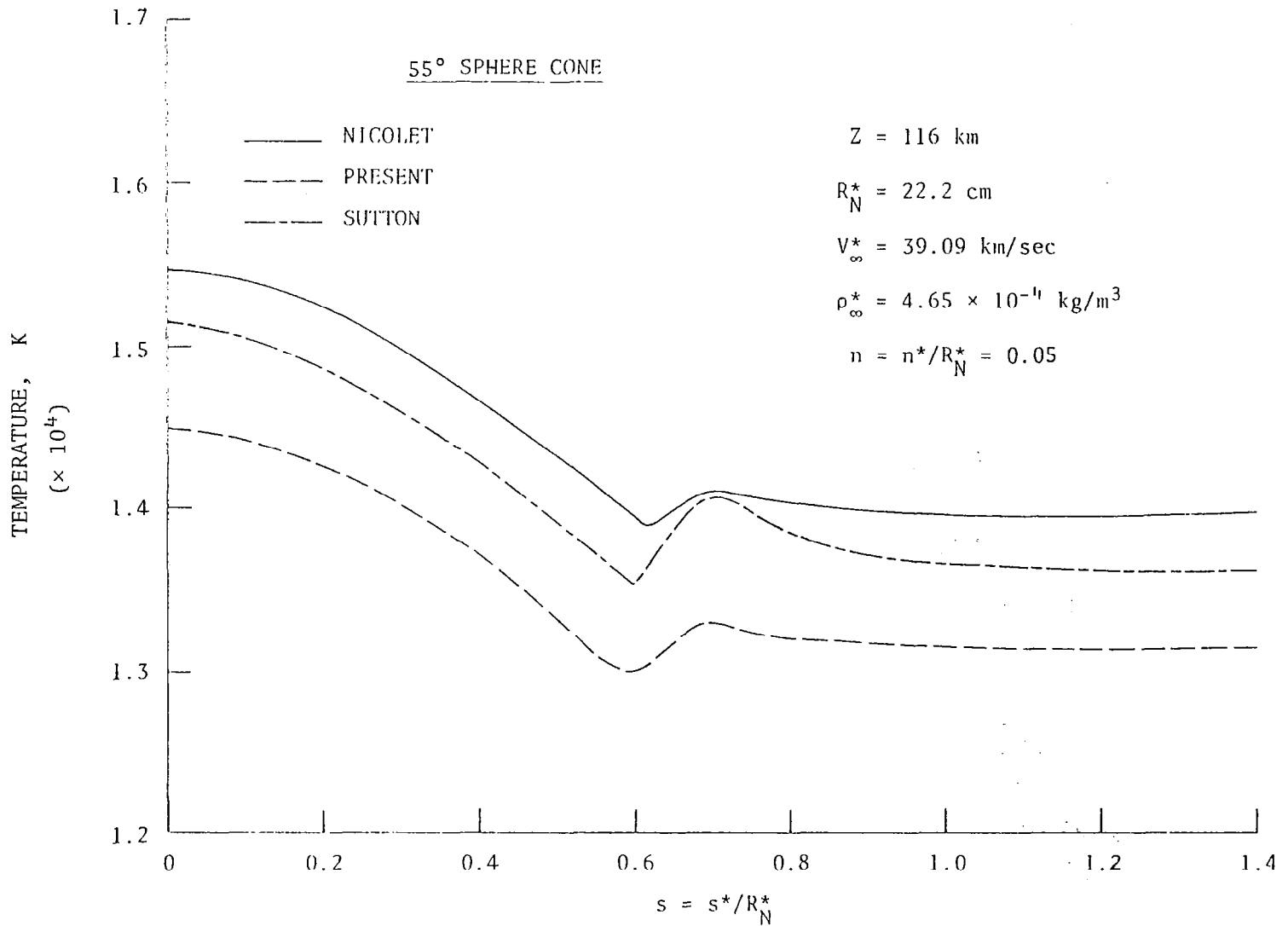
72

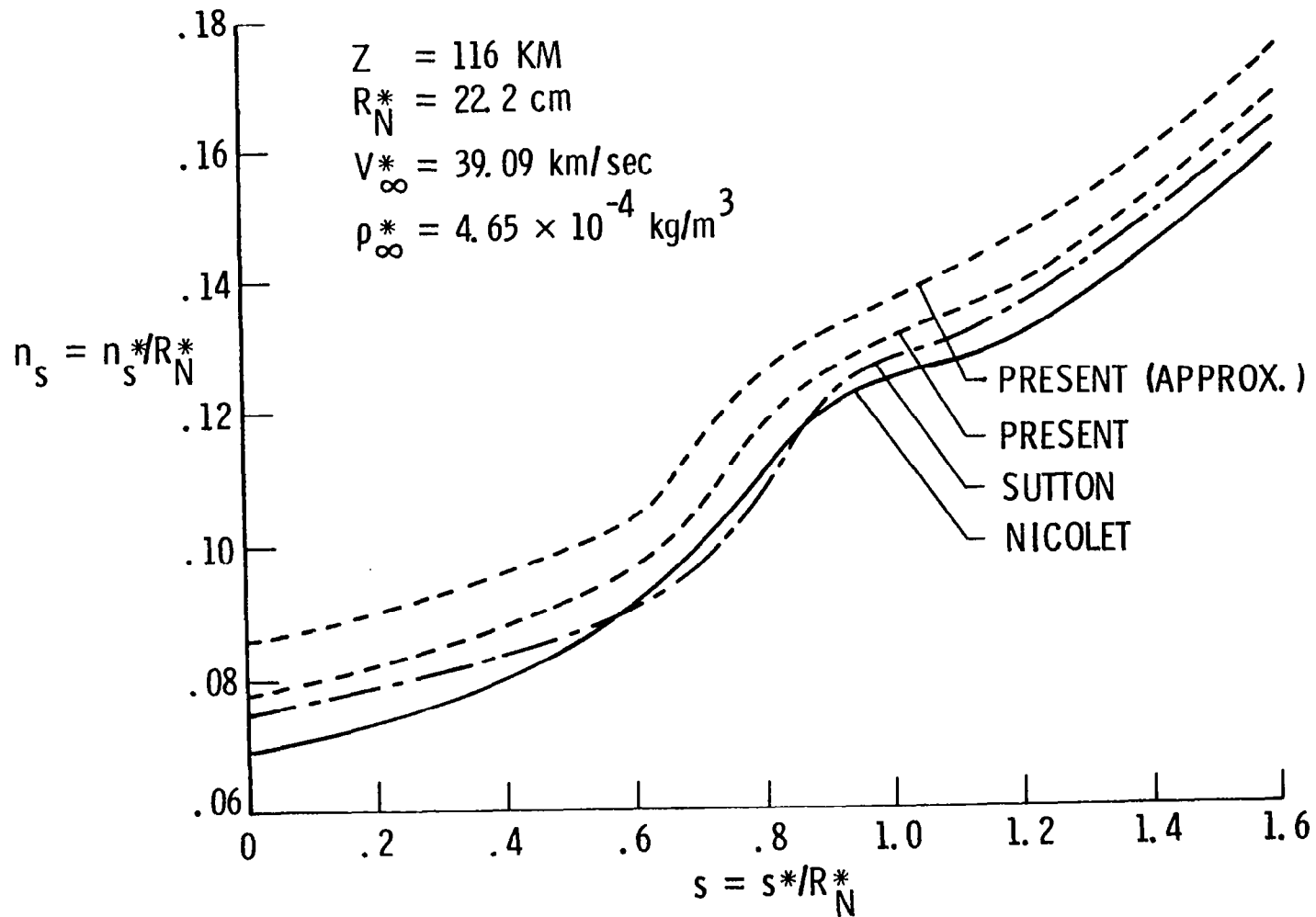Figure 11. Temperature variation just behind the shock (n = 0.05) with distance along the body surface (55° sphere cone, Z = 116 km).

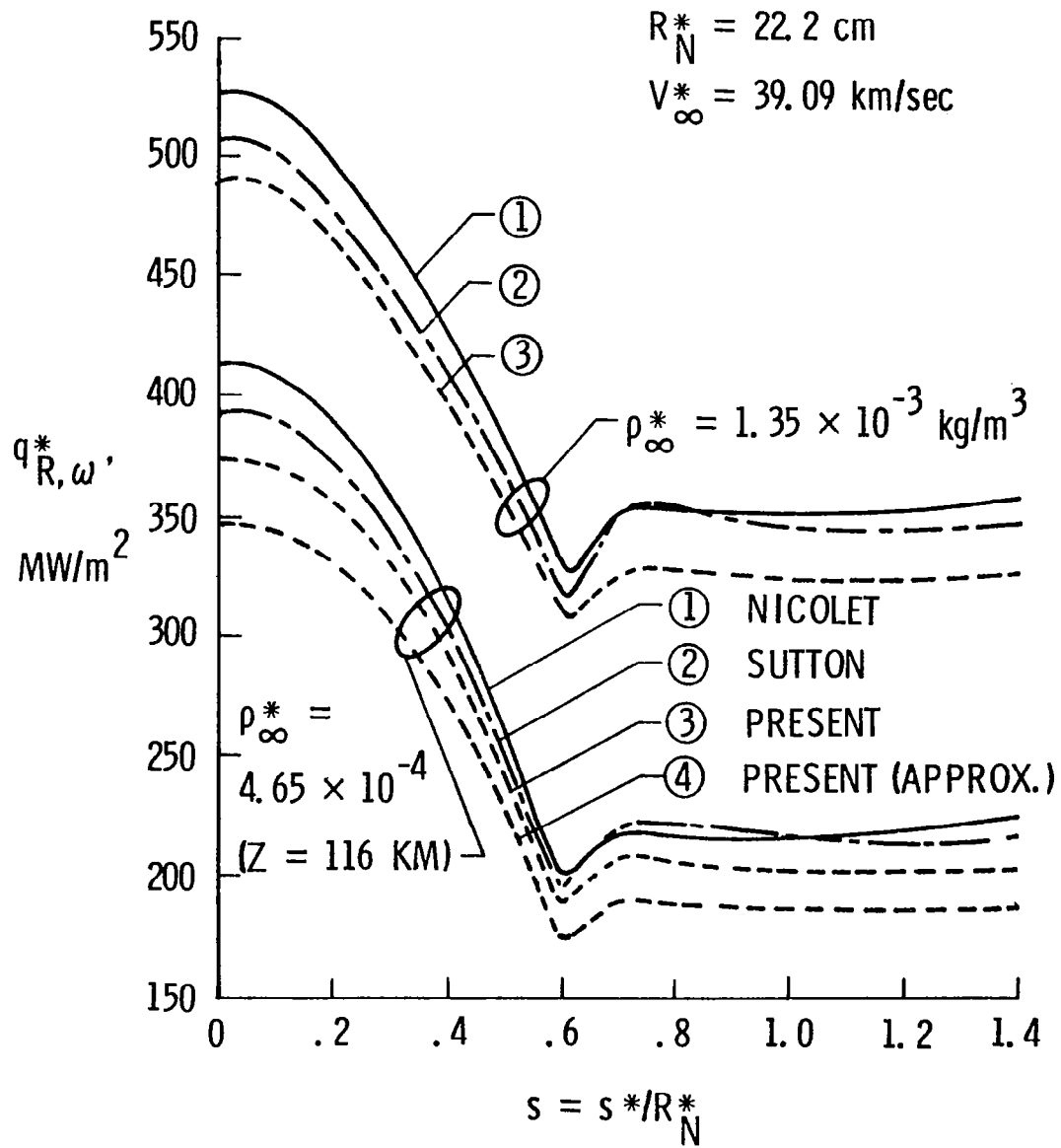Figure 12. Shock standoff variation with distance along the body surface (55° sphere cone, Z = 116 km).

Figure 13. Radiative heating along the body for two different free-stream densities (55° sphere cone).

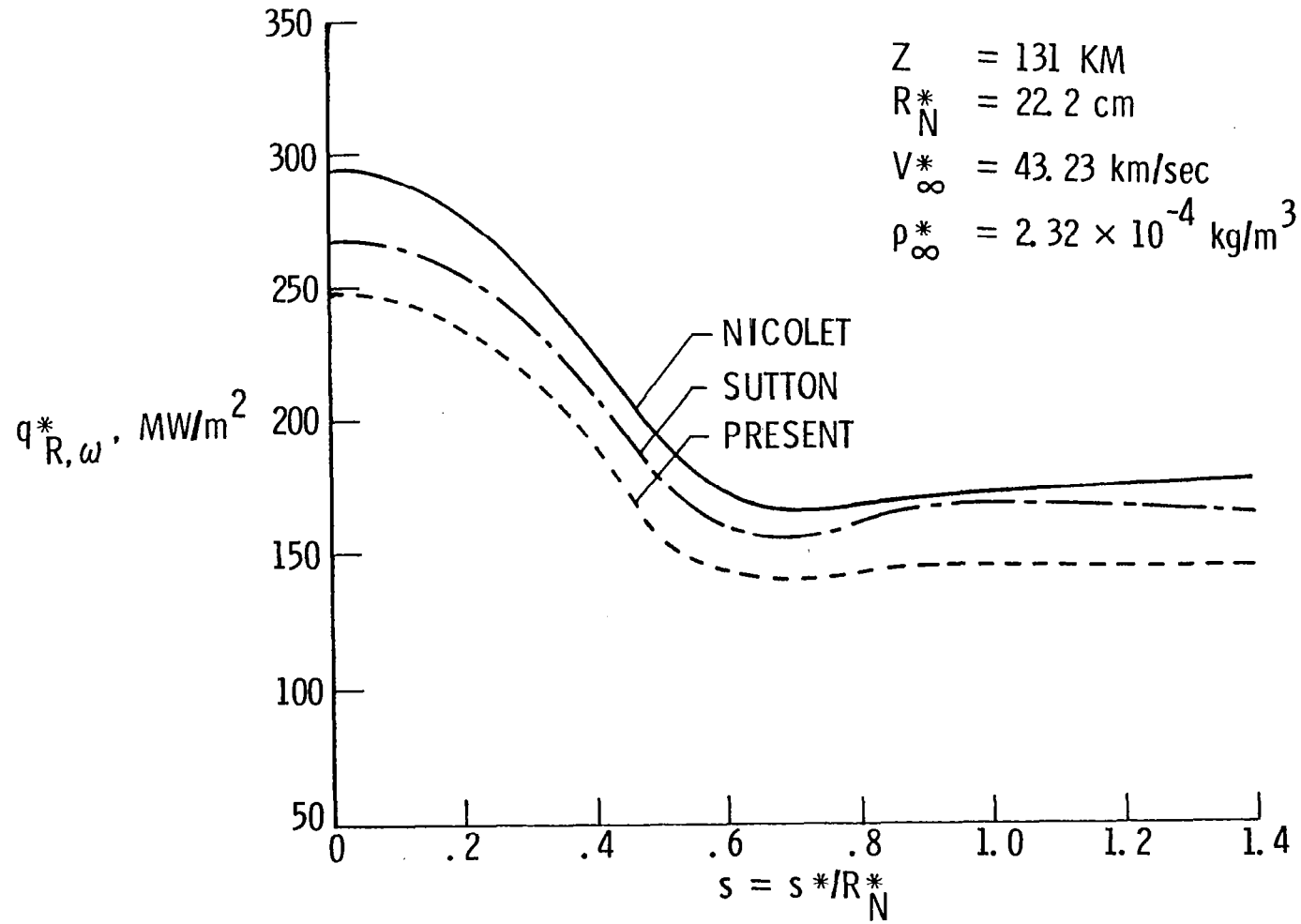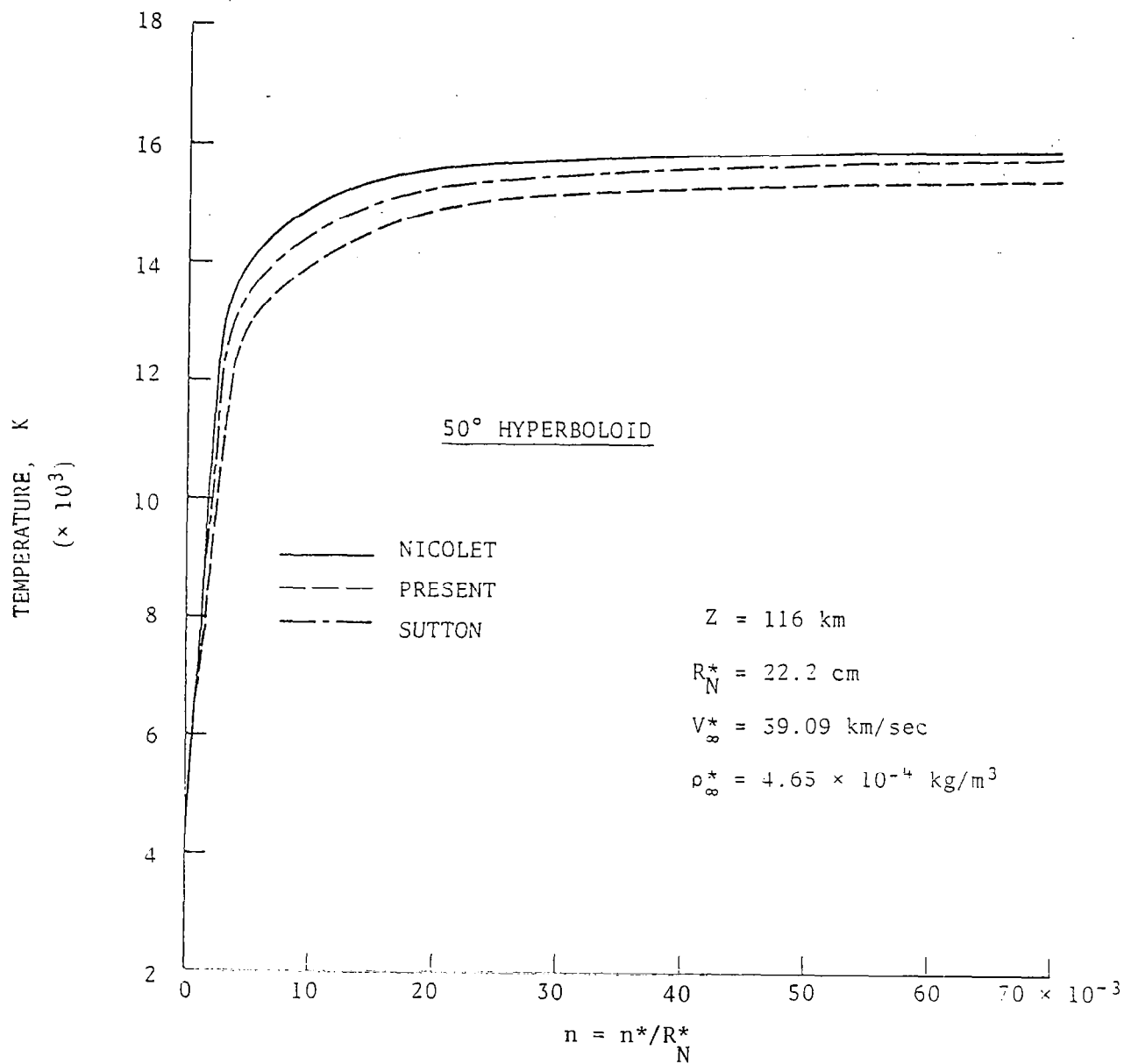Figure 14. Radiative heating along the body for entry conditions at Z = 131 km (55° sphere cone).

Figure 15.   Temperature distribution along the stagnation streamline
(50° hyperboloid, Z = 116 km).

present model and Nicolet's model. This difference is near the body (at n = 0.0095). Agreements between the results are better towards the shock.

The variation in temperature just behind the shock (at location n = 0.07) with distance along the body surface is illustrated in figure 16 for entry conditions at Z = 116 km. The results indicate very good agreement between the three radiation models. The results of the present model are within 1.4 percent of the results of Nicolet's model. As would be expected, maximum difference in results occurs at the stagnation streamline.

The shock standoff variation with distance along the body surface for entry conditions at Z = 116 km is shown in figure 17. As was the case with the 55-degree sphere cone, the present model is seen to overestimate the results in comparison to the other models.

The radiative heating rate along the body surface is illustrated in figures 18 to 20 for different entry conditions. For this body geometry also, the maximum heating occurs at the stagnation point. For Z = 116 km, results presented in figure 18 indicate that the present model underpredicts the heating rate by a maximum of about 13 percent when compared with Nicolet's model. For higher free-stream density, the results presented in figure 19 show smaller differences in the results of various radiation models. For entry conditions at Z = 131 km, results presented in figure 20 indicate that heat transferred to the body is significantly lower. This is because of lower free-stream density and pressure. As was the case with the 55-degree sphere cone at this altitude, the difference between the present and Nicolet's results is relatively higher.

It is found that use of the present model reduces the computational time significantly. The use of this model is recommended for simple parametric study. However, the use of the present model has its limitations. For problems with varying shock-layer compositions and large temperature variations, a suitable empirical correlation has to be developed from the detailed model to make the present model more versatile and accurate.
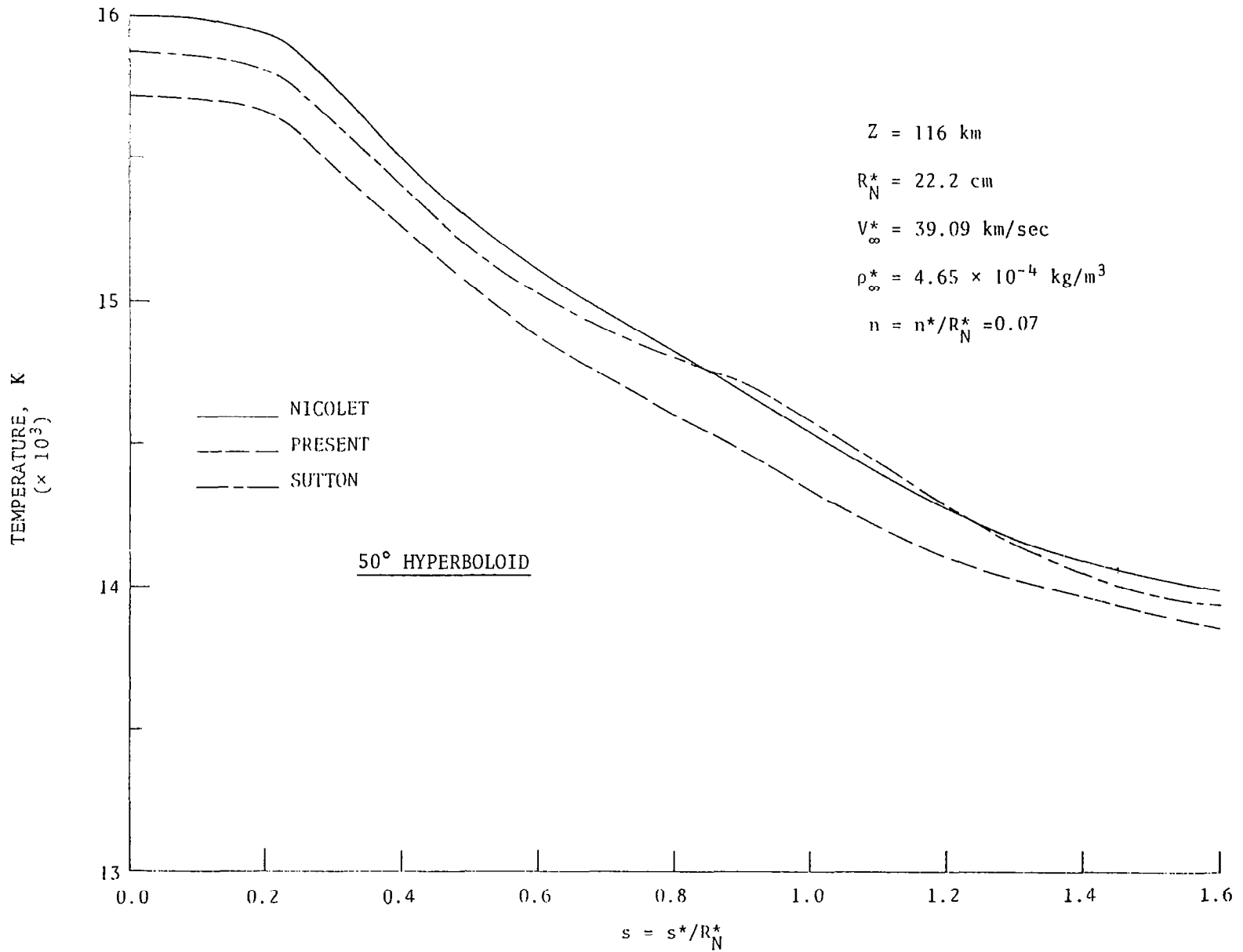
78

Figure 16. Temperature distribution just behind the shock (n = 0.07) with distance along the body surface (50° hyperboloid, Z = 116 km).
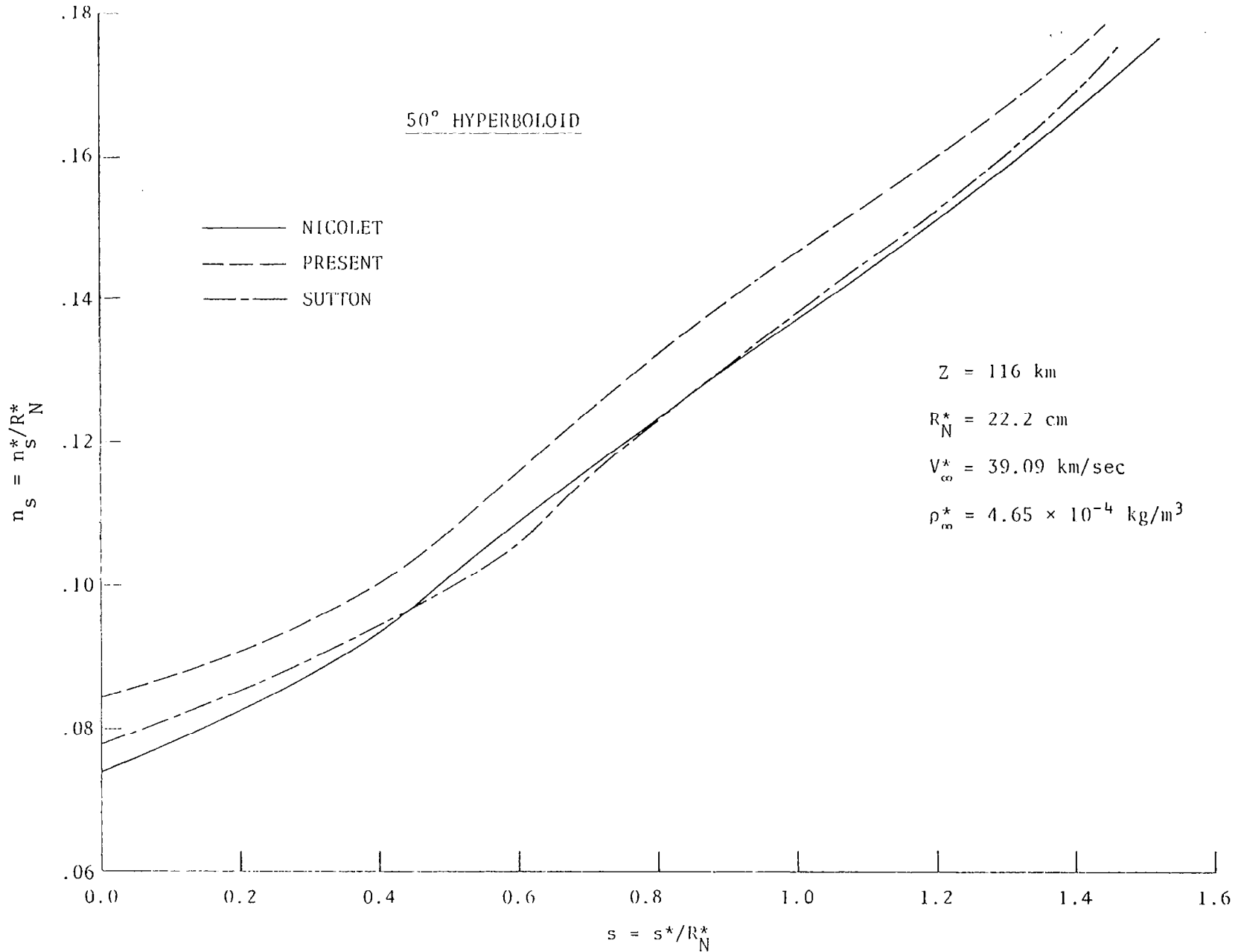
Figure 17. Shock standoff variation with distance along the body surface (50° hyperboloid, Z = 116 km).

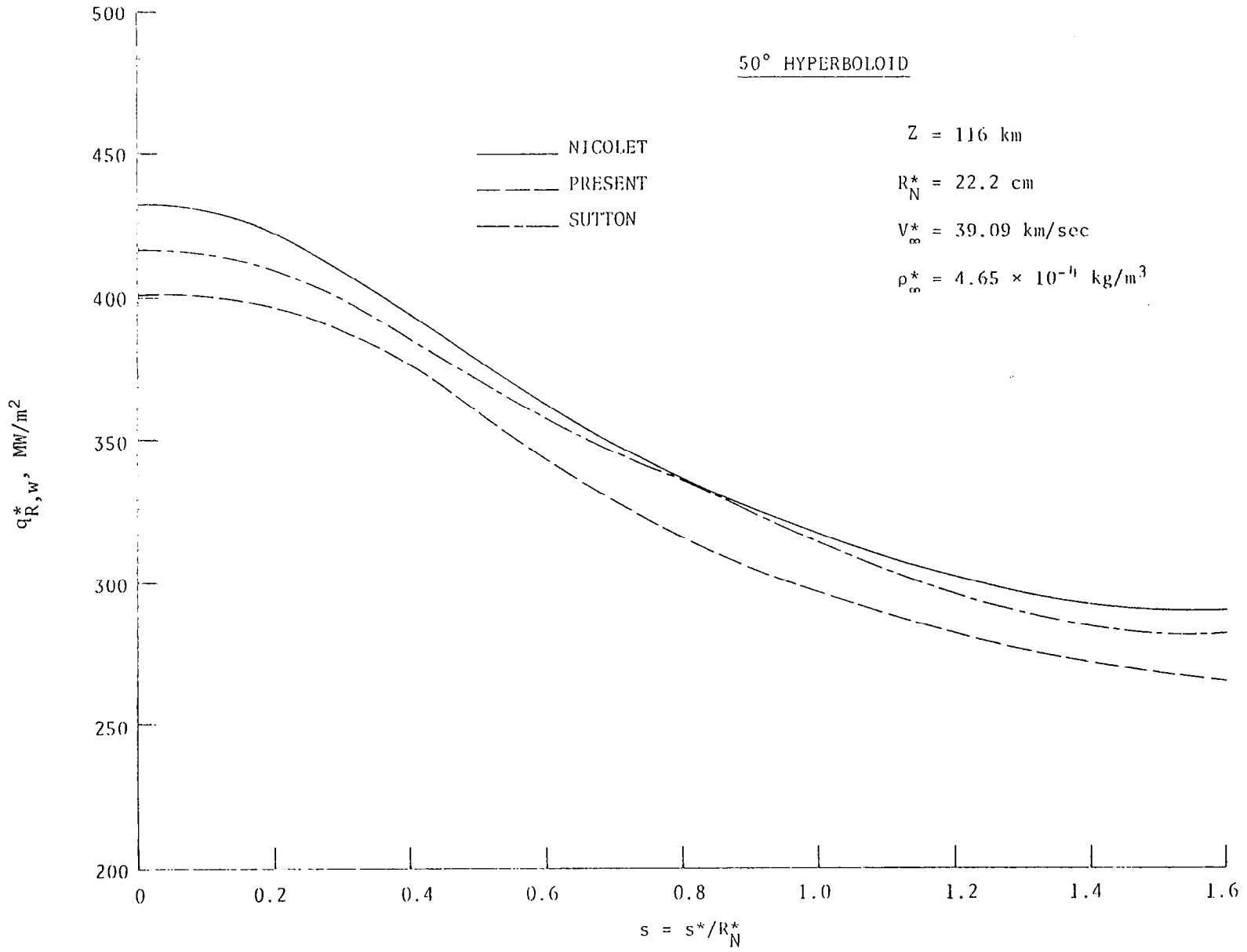Figure 18. Radiative heating along the body for entry conditions at Z = 116 km (50° hyperboloid).

50° HYPERBOLOID

NICOLET
PRESENT
SUTTON

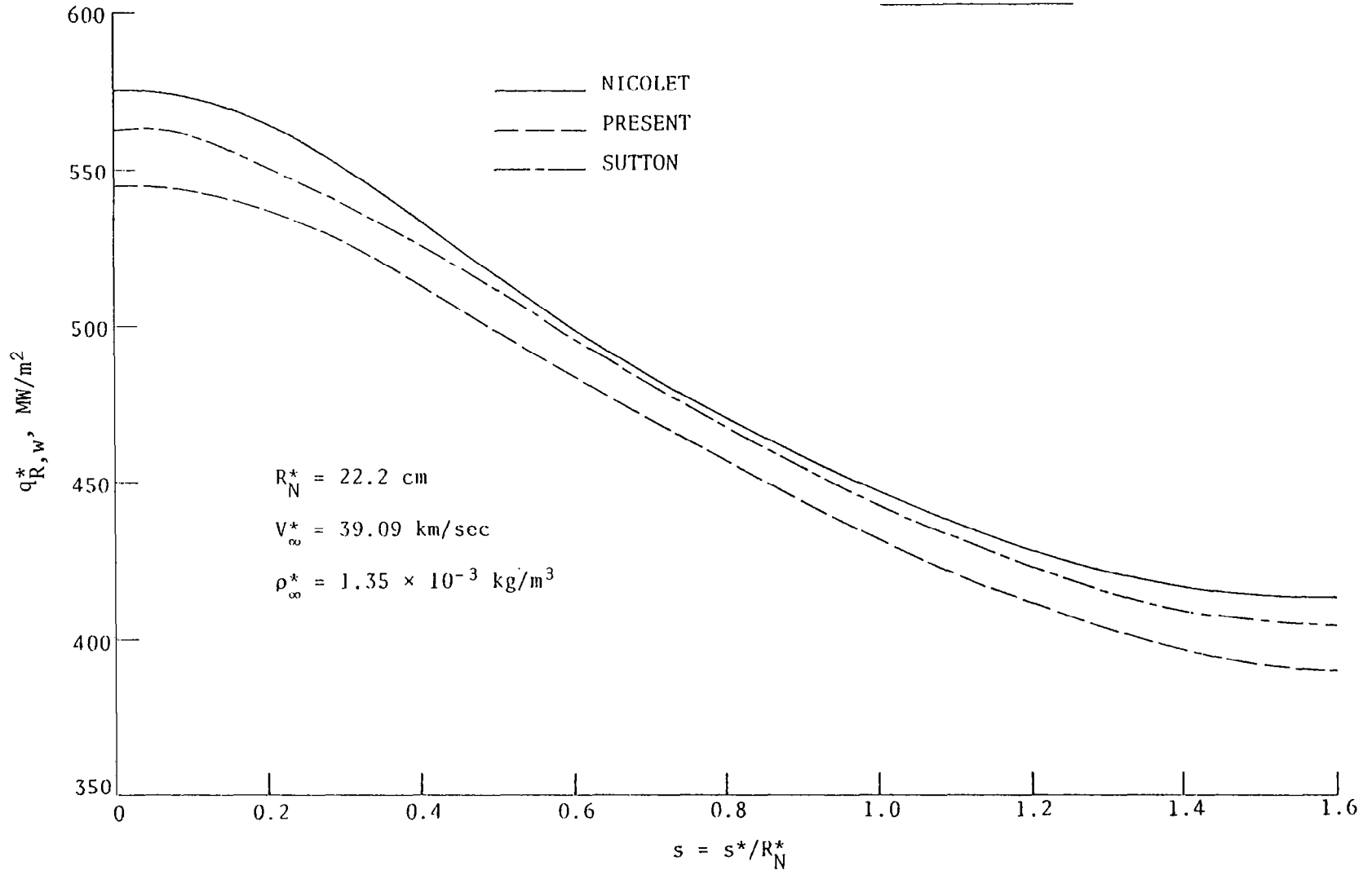$Z = 116$ km

$R_N^* = 22.2$ cm

$V_\infty^* = 39.09$ km/sec

$\rho_\infty^* = 4.65 \times 10^{-4}$ kg/m^3

$s = s^*/R_N^*$

$q_{R,w}^*$, MW/m^2

50° HYPERBOLOID

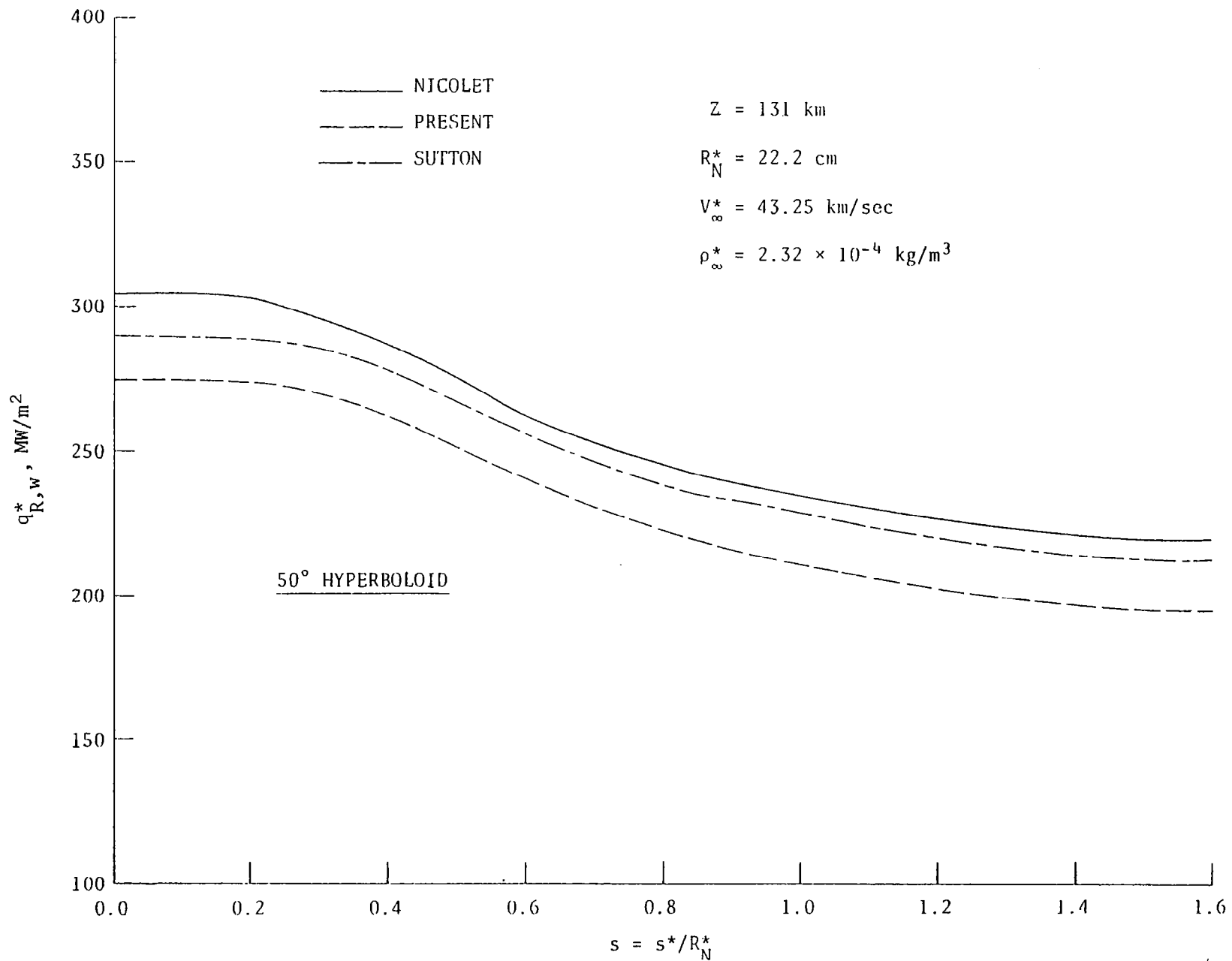Figure 19. Radiative heating along the body for free-stream density higher than at Z = 116 km (50° hyperboloid).

Figure 20. Radiative heating along the body for entry conditions at Z = 131 km (50° hyperboloid).

The chart shows:

Legend:
- NICOLET (solid line)
- PRESENT (dashed line)
- SUTTON (dash-dot line)

Conditions:
$Z = 131$ km

$R_N^* = 22.2$ cm

$V_\infty^* = 43.25$ km/sec

$\rho_\infty^* = 2.32 \times 10^{-4}$ kg/m^3

50° HYPERBOLOID

Y-axis: $q_{R,w}^*$, MW/m^2 (ranging from 100 to 400)

X-axis: $s = s^*/R_N^*$ (ranging from 0.0 to 1.6)

Influence of NLTE Radiation Without Ablation Injection

Specific results obtained by using the NLTE formulation for
the radiative transport, as described by equations (64) to (66),
are presented in this subsection. The governing equations (6) to
(13) were used to solve the shock-layer flow which was considered
to be viscous and in chemical equilibrium. The effect of ablation
mass injection into the flow was neglected. In this subsection,
equilibrium radiative transport solutions are presented along with
the NLTE results for comparative purpose. For this study, the entry
bodies considered are a 50-degree hyperboloid and a 55-degree sphere
cone which enter the Jovian atmosphere at a zero-degree angle of
attack. In both cases, the body nose radius R_N^* is taken to be
22.2 cm. The body surface is assumed to be gray having a surface
emittance of 0.8, and the wall temperature T_w is taken to be
constant at 4,200 K. The variation of the nonequilibrium absorption
coefficient (as compared to the equilibrium values) is shown in
figure 21 at a temperature of 15,950 K. Within the confines of
assumptions made in this study, the equilibrium and nonequilibrium
absorption coefficients are found to be about the same beyond 10 eV.
The shaded portion in the figure represents the decrease in the
absorption coefficient values as a result of an increase in the
population of higher energy levels.

NLTE results for a 50-degree hyperboloid. - The variation of
collisional relaxation time across the shock layer is shown in figures
22(a) to 22(c) for three different entry conditions. Figure 22(a)
shows the results for combined H-H and 0.5 H - 0.5 H_2 collisions,
figure 22(b) for H-H and H^+-H^+ collisions, and figure 22(c) for
0.95 H - 0.05 H_2 and H^+-H^+ collisions. The results indicate that
in all three cases the relaxation time does not vary significantly
across the shock layer except very close to the body. Thus, higher
NLTE effects will be expected in regions closer to the wall where
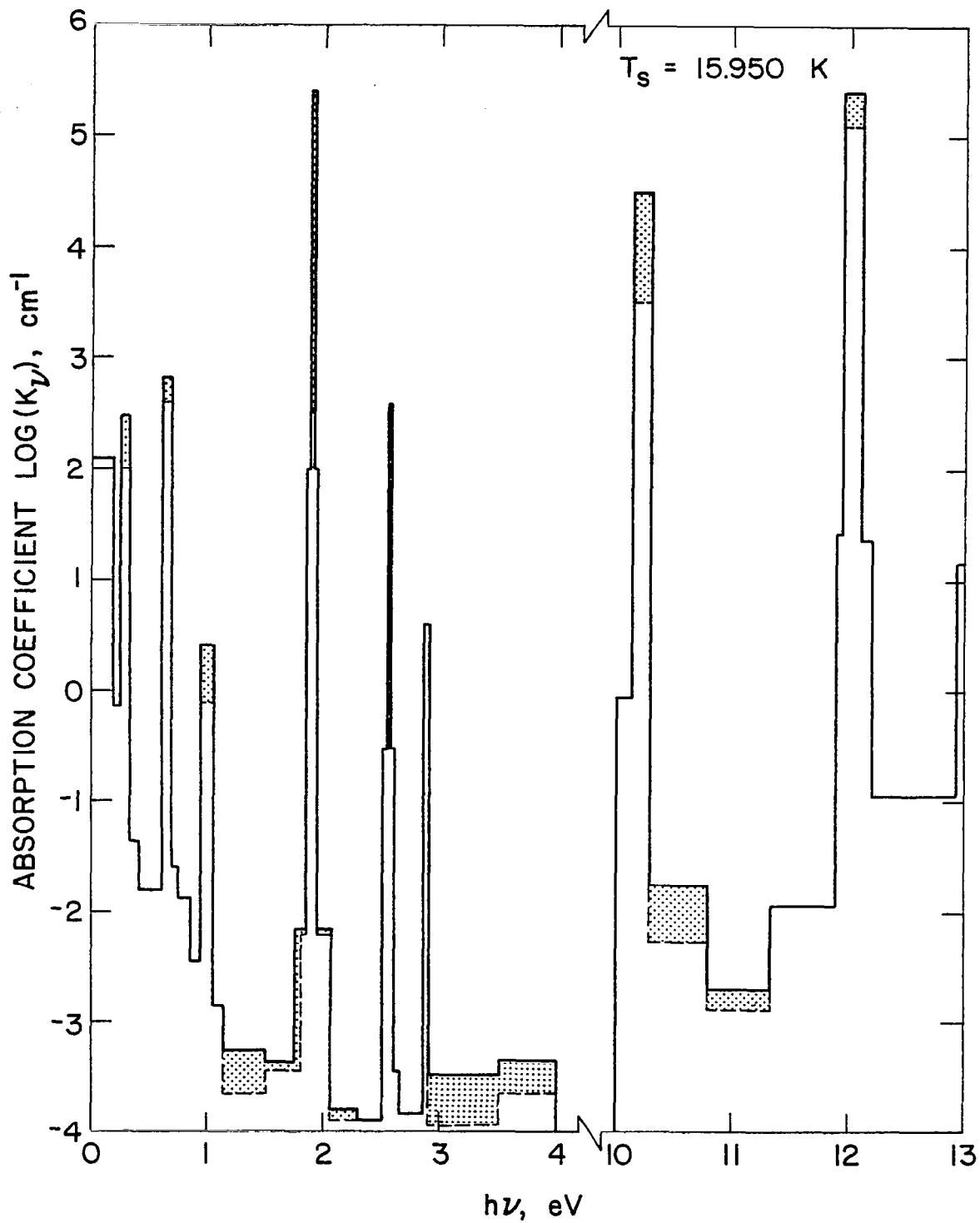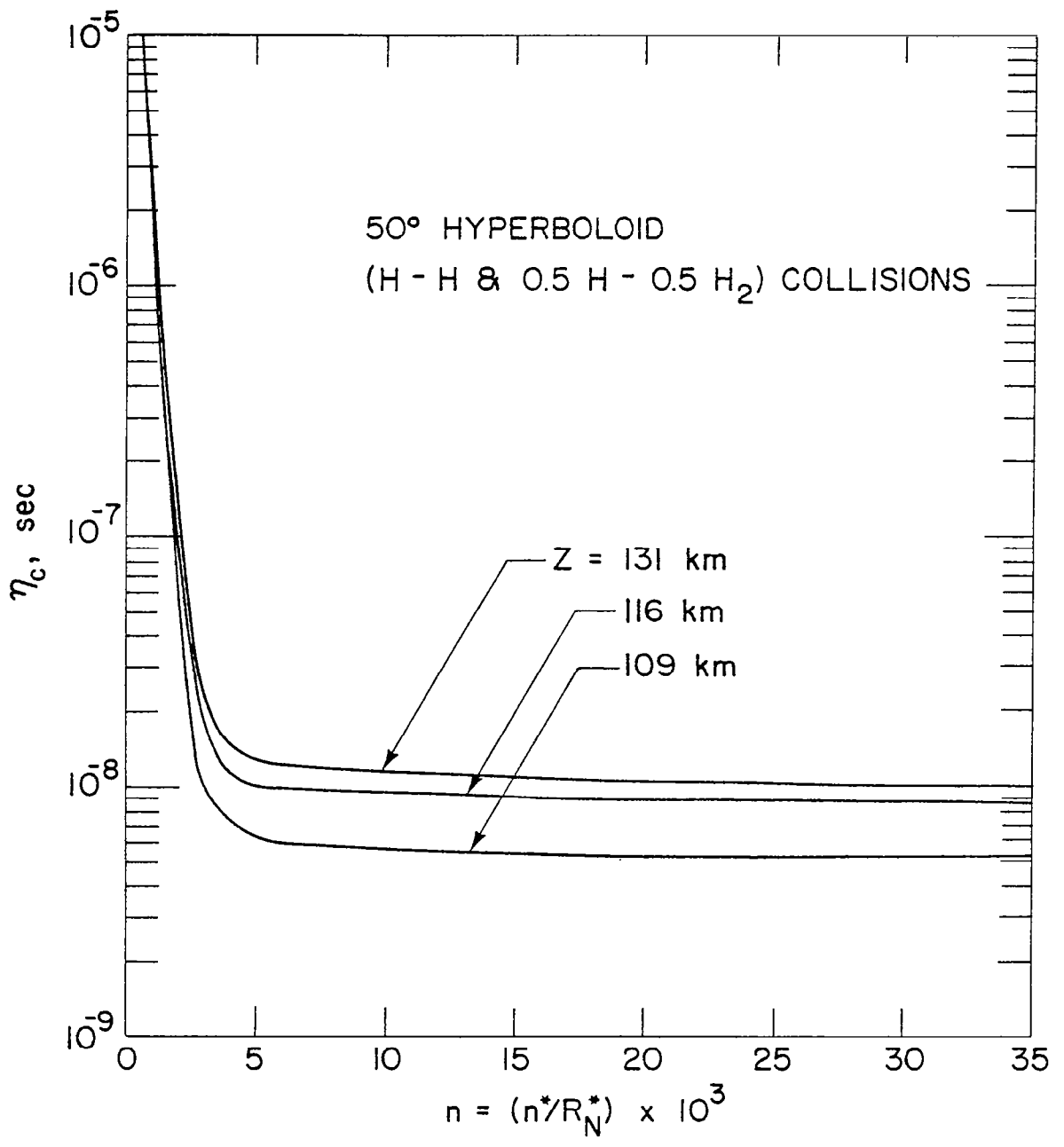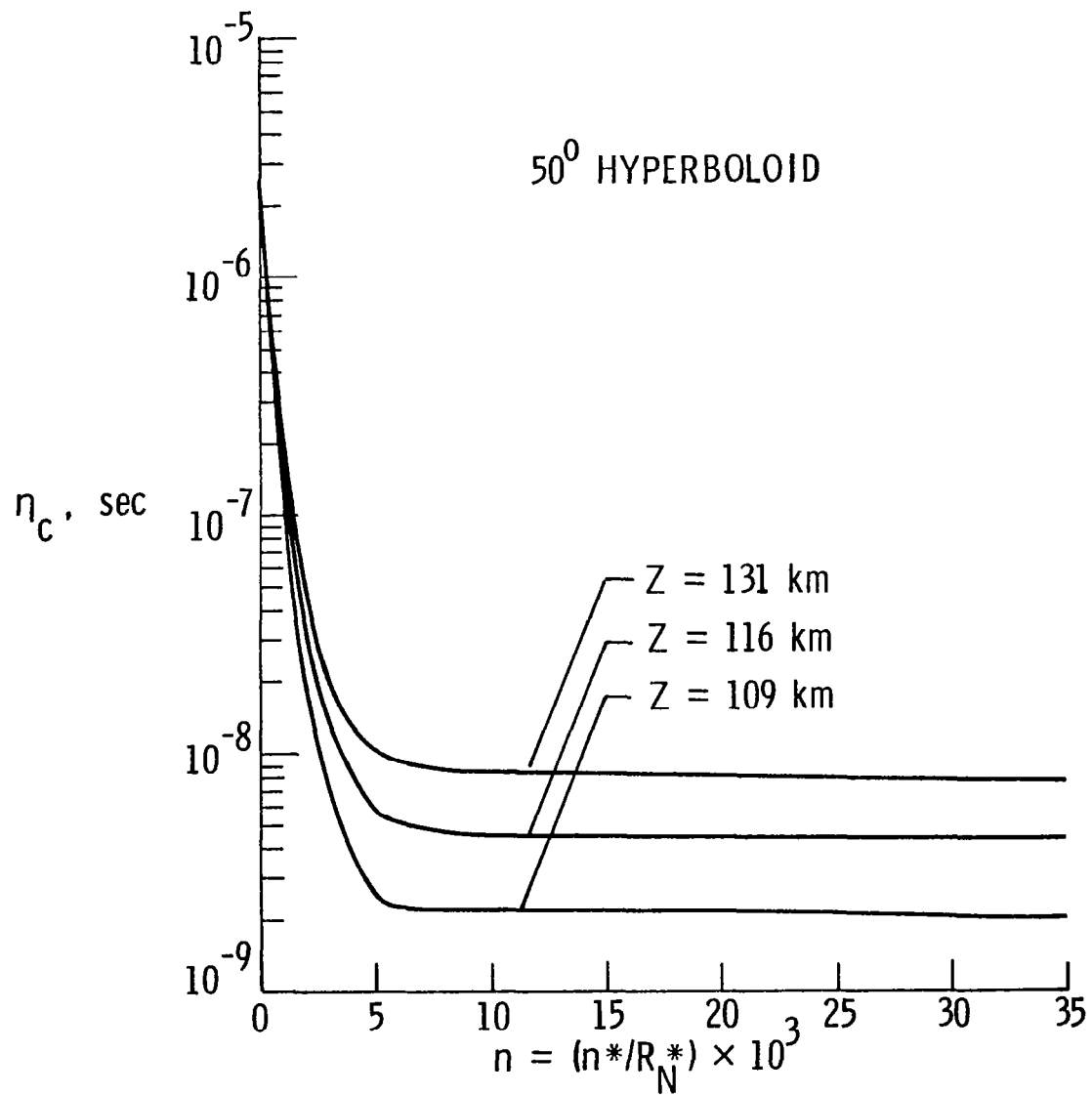the assumption of chemical equilibrium usually is justified (ref. 8).

Figure 21. Equilibrium and nonequilibrium absorption coefficients
for two-level energy transitions.
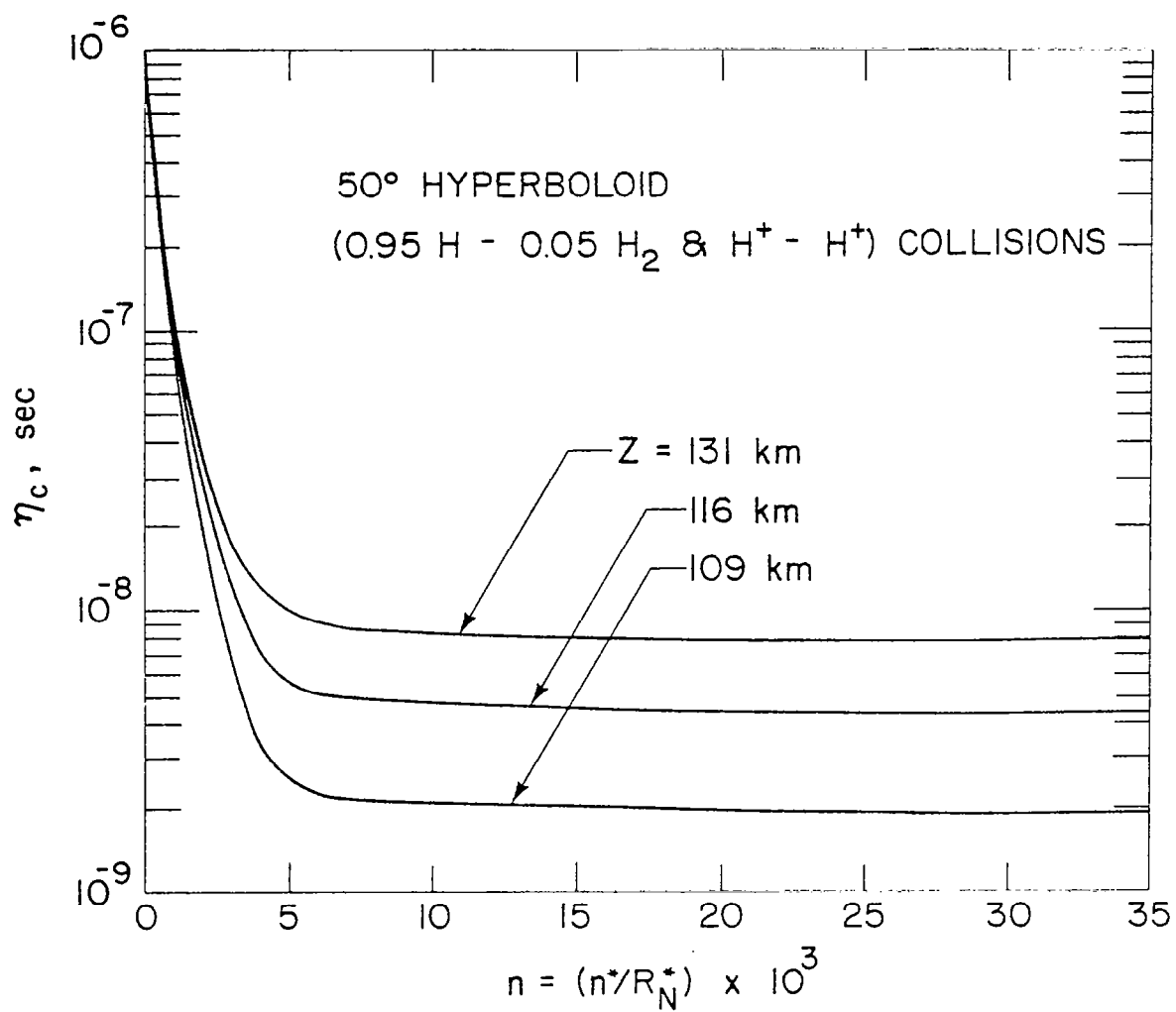
(a) for H-H and 0.5 H-0.5 H_2 collisions.

Figure 22.   Variation of relaxation time across the shock layer.

(b) for H-H and H^+-H^+ collisions.

Figure 22. (Continued).

50° HYPERBOLOID
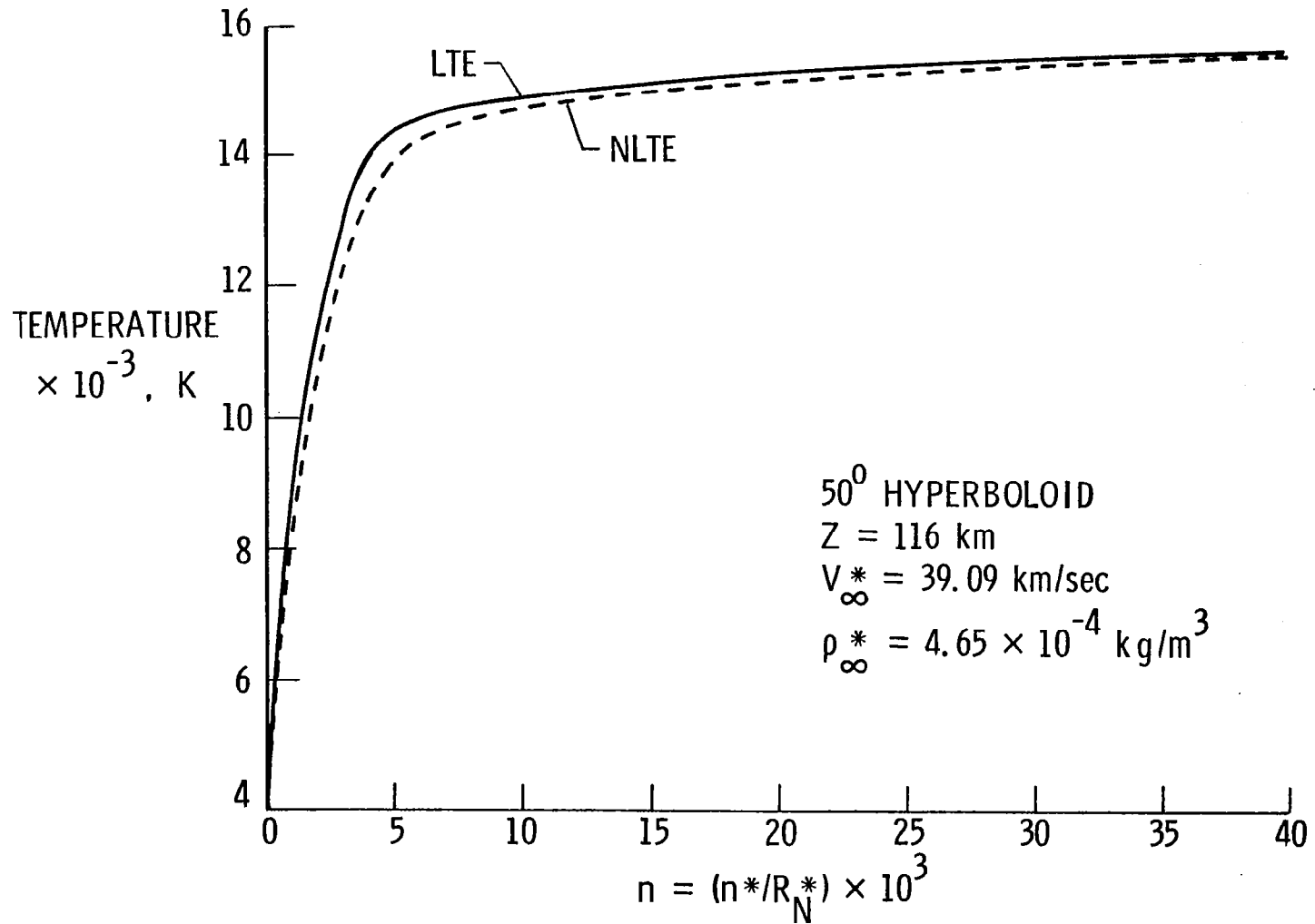
(0.95 H - 0.05 H_2 & H^+ - H^+) COLLISIONS

Z = 131 km

116 km

109 km

η_c, sec

$n = (n^*/R_N^*) \times 10^3$

(c) for 0.95 H-0.05 H_2 and H^+-H^+ collisions.

Figure 22. (Concluded).

88

Since relaxation times are comparatively longer for higher entry altitudes, one would expect the NLTE effects to be greater at higher altitudes. The results presented in figure 22(a) for combined H-H and $0.5 H - 0.5 H_2$ collisions, of course, are not representative of the results for the actual shock-layer collisional processes; they are presented here only for comparative purposes. The results of the other two collisional processes are found to be very close [figs. 22(b) and (c)], and they do represent very nearly the results of actual shock-layer collisional processes.

For the entry condition at $Z = 116$ km, the temperature distribution along the stagnation streamline is illustrated in figures 23(a) and (b). The results in figure 23(a) are for combined H-H and H^+-H^+ collisions and in figure 22(b) for $0.95 H - 0.05 H_2$ and H^+-H^+ collisions; the two sets of results are found to be almost identical. The results clearly indicate that the NLTE temperature distribution is consistently lower than the equilibrium temperature. This implies that the shock-layer gas absorbs less energy under NLTE conditions than under equilibrium conditions. This is because under NLTE conditions (where the population ratios of the energy levels deviate from the equilibrium Boltzmann distribution) the number of particles (capable of absorbing the incoming radiation) in the ground state is comparatively less than under equilibrium conditions. The differences between LTE and NLTE results are seen to be lower toward the shock than toward the body. This is mainly due to direct dependence of the collisional deactivation process on the temperature. The maximum NLTE effect, therefore, will occur near the body surface where the collisional deactivation process is slower because of the lower temperature (see also the results presented in fig. 22).

For the entry conditions at $Z = 116$ km, the temperature distributions along the body are shown in figure 24 for two locations in the shock layer. The NLTE results were obtained by considering the combined H-H and H^+-H^+ collisional process. In the region close to the shock ($n = 0.068$), the differences between the LTE and NLTE temperatures are negligible (less than 0.1 percent). On the other hand, at a location

(a) for H-H and H^+-H^+ collisions.

Figure 23. Temperature variation across the shock layer.
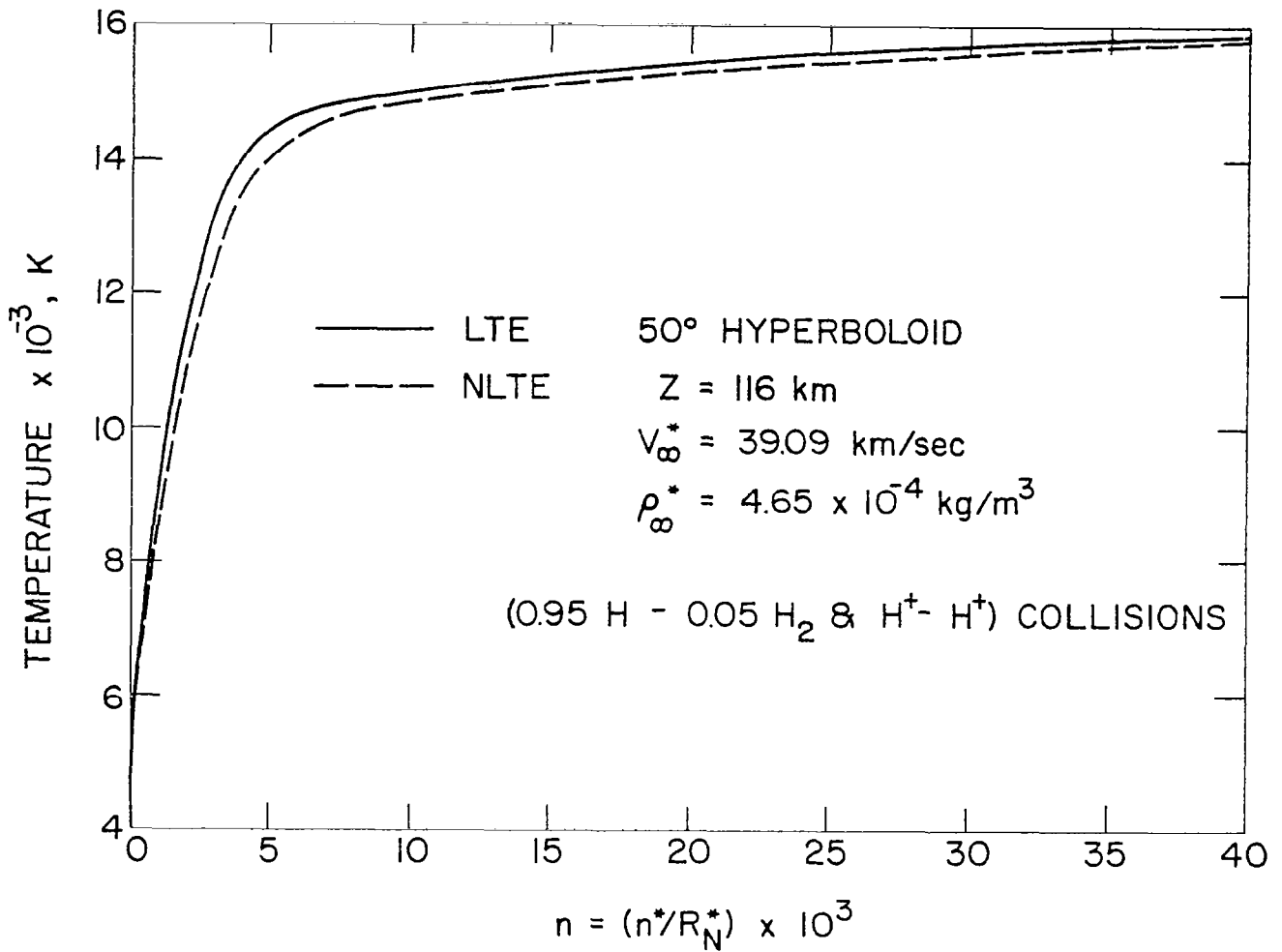
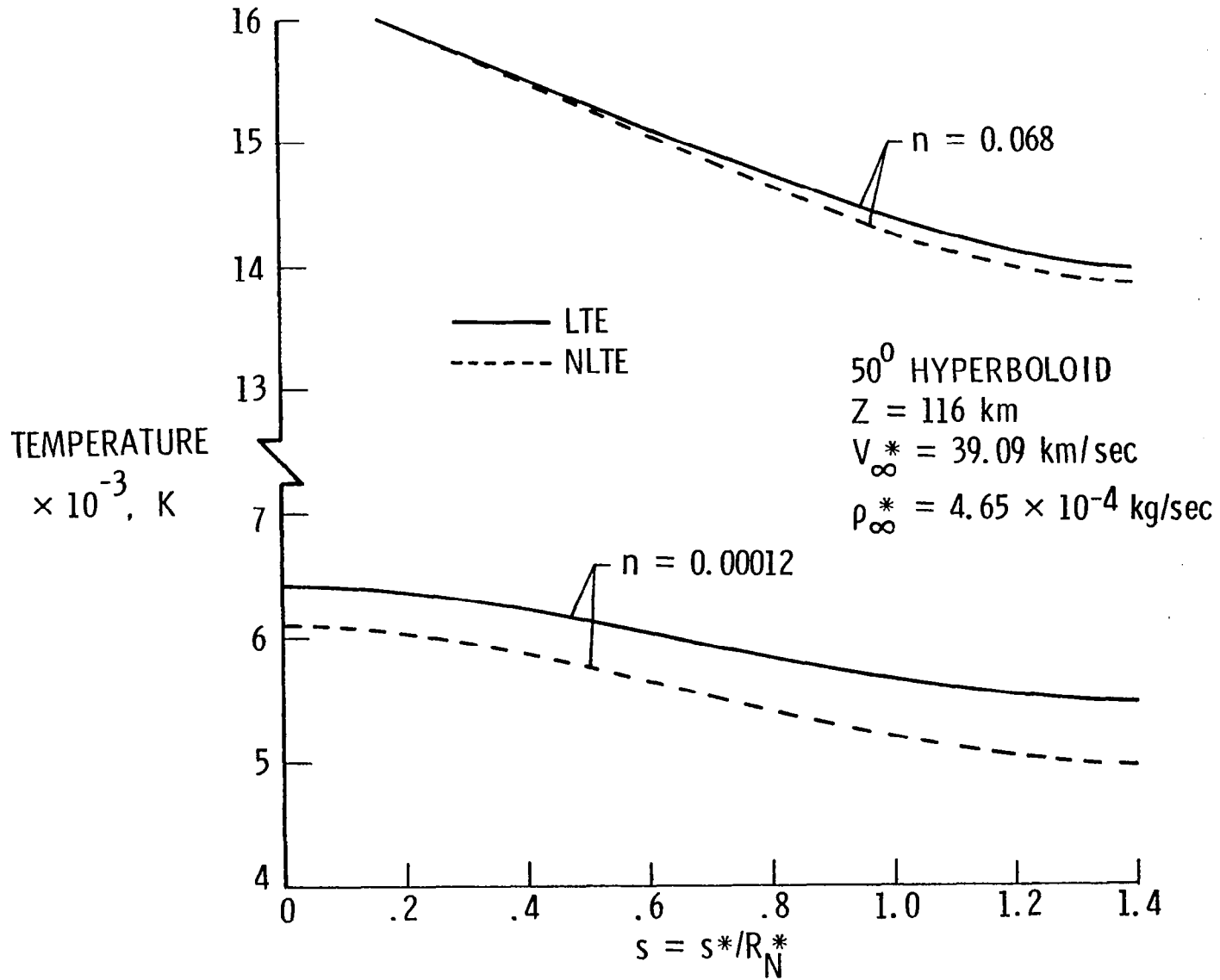(b) for 0.95 H-0.05 H_2 and H^+-H^+ collisions.

Figure 23. (Concluded).

Figure 24.   Temperature variation along the body for two locations in
the shock layer, H-H and H⁺-H⁺ collisions.

closer to the body (n = 0.00012), the differences are significantly larger: a difference of about 6.8 percent is noted at the stagnation point. Since temperature decreases in the direction of the s coordinate, the NLTE influence is found to be greater at locations away from the stagnation streamline.

For the entry conditions at $Z = 116$ km, the shock-standoff variation with distance along the body surface is shown in figure 25. Since the shock-standoff distance is influenced by the entry conditions and the shape of the entry body, the conditions of NLTE in the shock layer do not have any effect on its variation.

For entry conditions at $Z = 109$ km, the LTE and NLTE radiative heating along the body are illustrated in figure 26. The NLTE results were obtained by considering the combined H-H and H^+-H^+ collisional process. The results simply indicate that the NLTE heating is consistently lower than the LTE heating all along the body. Since the number density of participating particles is relatively higher at lower altitudes, larger NLTE effects would be expected at altitudes higher than $Z = 109$ km.

For the peak heating entry conditions (i.e., for $Z = 116$ km), the LTE and NLTE results of radiative heating along the body are illustrated in figure 27. In order to assess the influence of various deactivation processes, the NLTE results have been obtained by considering five different collisional relaxation times. This is essential because the exact nature of the collisional deactivation process, which actually occurs in the shock-heated gas, is not known. It is evident from the figure that the NLTE results obtained by considering only the H^+-H^+ collisions are very close to the LTE results. Consequently it may be concluded that in a fully ionized plasma the assumption of LTE is justified. The NLTE results obtained by considering only the 0.5 H - 0.5 H_2 collisions are seen to be significantly lower than the LTE results. This, however, does not represent a physically realistic situation for the shock-layer gas (because of a very low number density of hydrogen molecules); the results are presented here only for
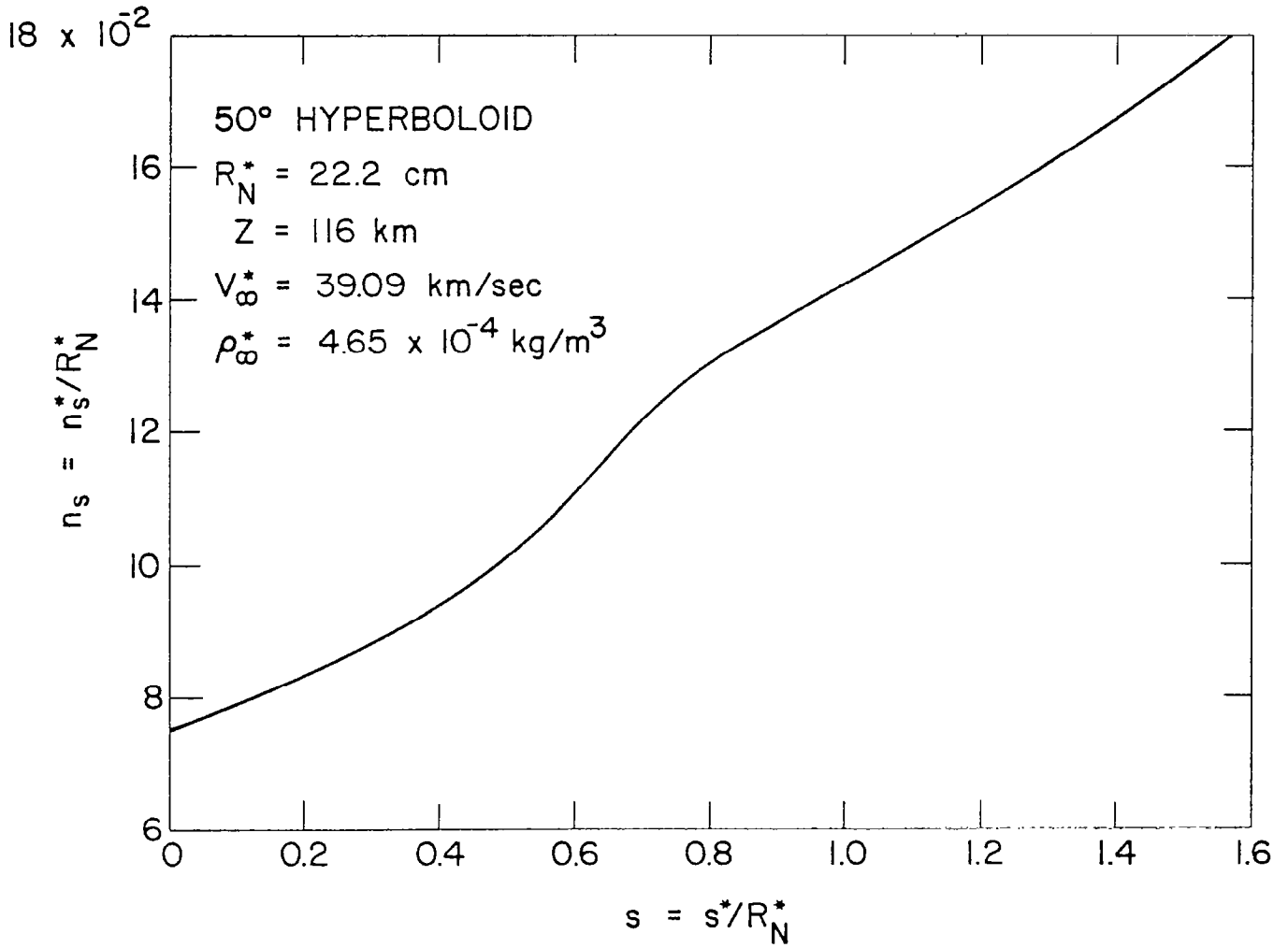
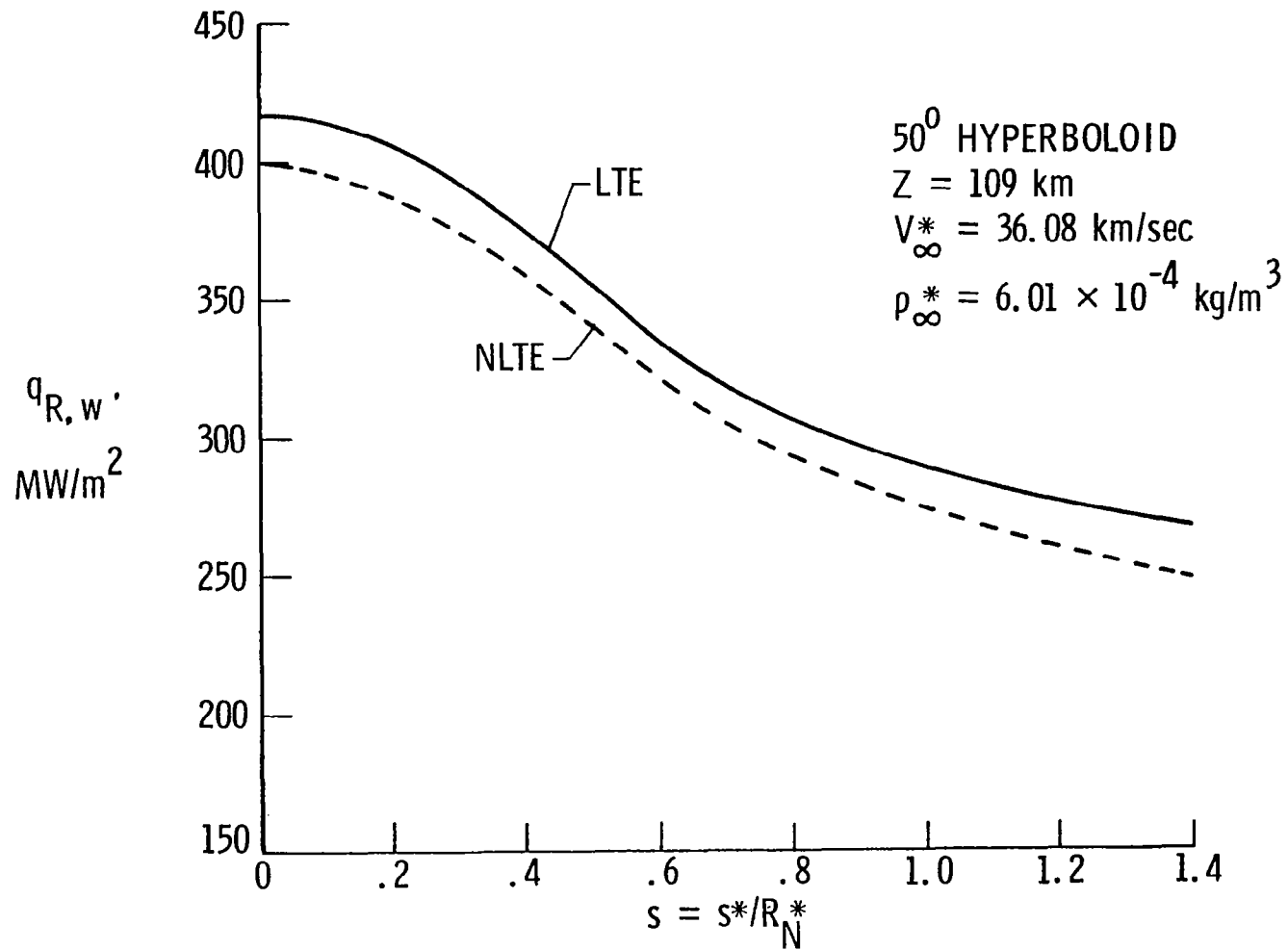Figure 25. Shock-standoff variation with distance along the body surface.

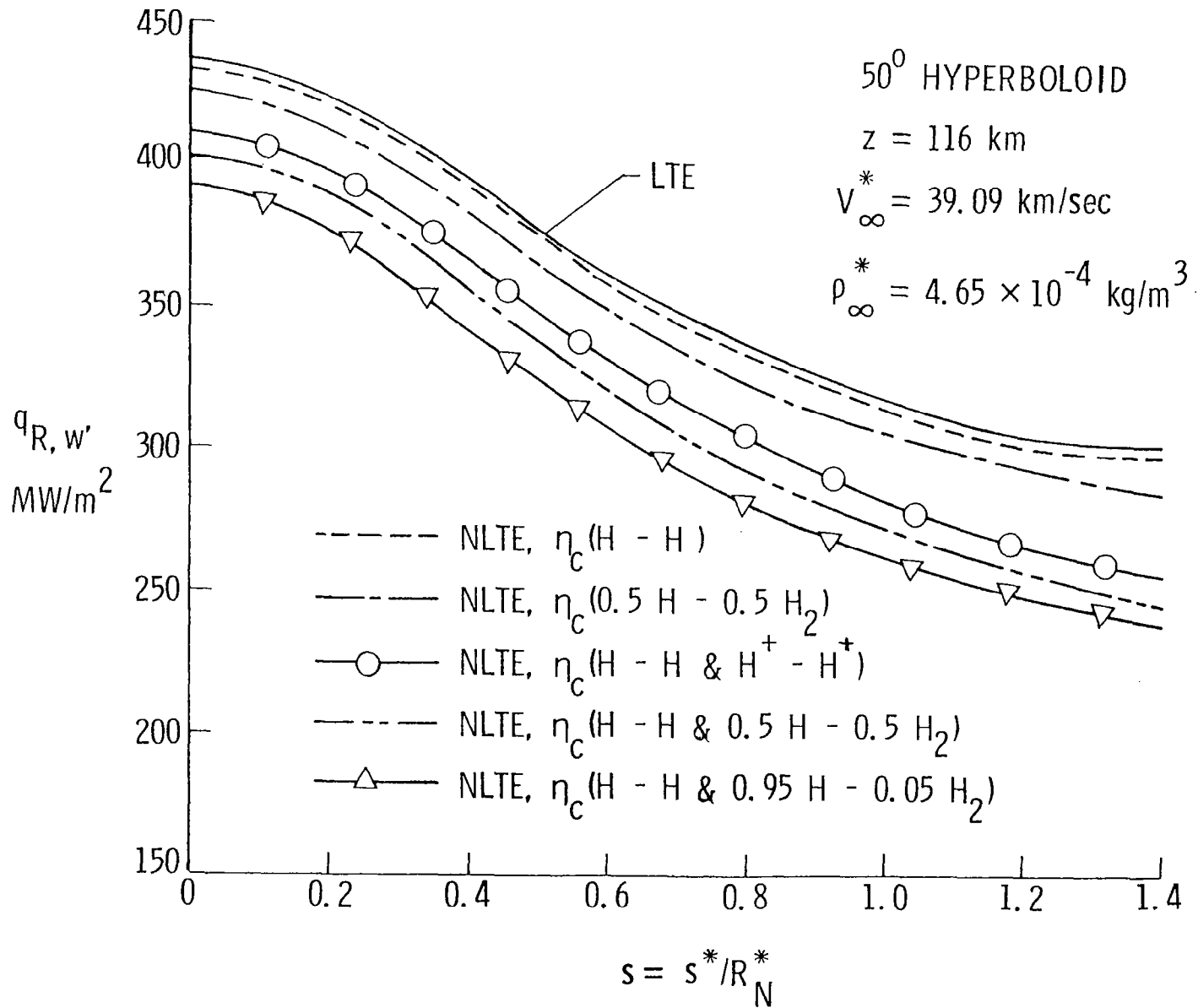Figure 26. Radiative heating along the body for entry conditions at Z = 109 km, H-H and H⁺-H⁺ collisions.

Figure 27. Radiative heating along the body for entry conditions at Z = 116 km.

comparative purposes. Probably the more realistic collisional process
for the shock-layer gas may be represented by the combined H-H and
H^+-H^+ or H-H_2 collisions. The NLTE results obtained by considering the
combined relaxation times of these collisions are seen to be much lower
than the LTE results all along the body. The maximum NLTE effects are
found to be for the case of combined H-H and $0.95\ H$ - $0.05\ H_2$ collisions.
The difference between LTE and NLTE results for this case is 11 percent
at the stagnation point. The case of the combined H-H and H^+-H^+ col-
lisional process (which is very close to the case of the combined
$0.95\ H$ - $0.05\ H_2$ and H^+-H^+ process), however, appears to be more phys-
ically convincing. For this case, a comparison of results presented in
figures 26 and 27 reveals that NLTE effects are significantly higher
at $Z = 116$ km than at $Z = 109$ km. Figure 27 shows a nine percent
reduction in radiative heating for this case at the stagnation point.
Perhaps an even more convincing process to consider will be the combined
H-H, H^+-H^+, and $0.95\ H$ - $0.05\ H_2$ collisional process. However, at
present no theory is available to calculate the relaxation times of such
collisions. The effects of such collisions, of course, will be lower
than those for the combined H-H and $0.95\ H$ - $0.05\ H_2$ collisions; the
results are expected to be closer to the results of the combined H-H
and H^+-H^+ collisions.

For entry conditions at $Z = 131$ km, the results of radiative and
convective heating along the body are illustrated in figure 28. The
NLTE results were obtained by considering the combined H-H and H^+-H^+
collisional process. For radiative heating, NLTE results are shown
also for two-level energy transitions. The results clearly indicate
that, although differences between LTE and NLTE results are small
for the convective heating, they are considerably larger for the
radiative heating. The contributions of higher level energy trans-
itions on NLTE results are seen to be quite small (less than 1.7
percent). Since NLTE affects the convective heating only through a
different temperature distribution, the effects are seen to be quite
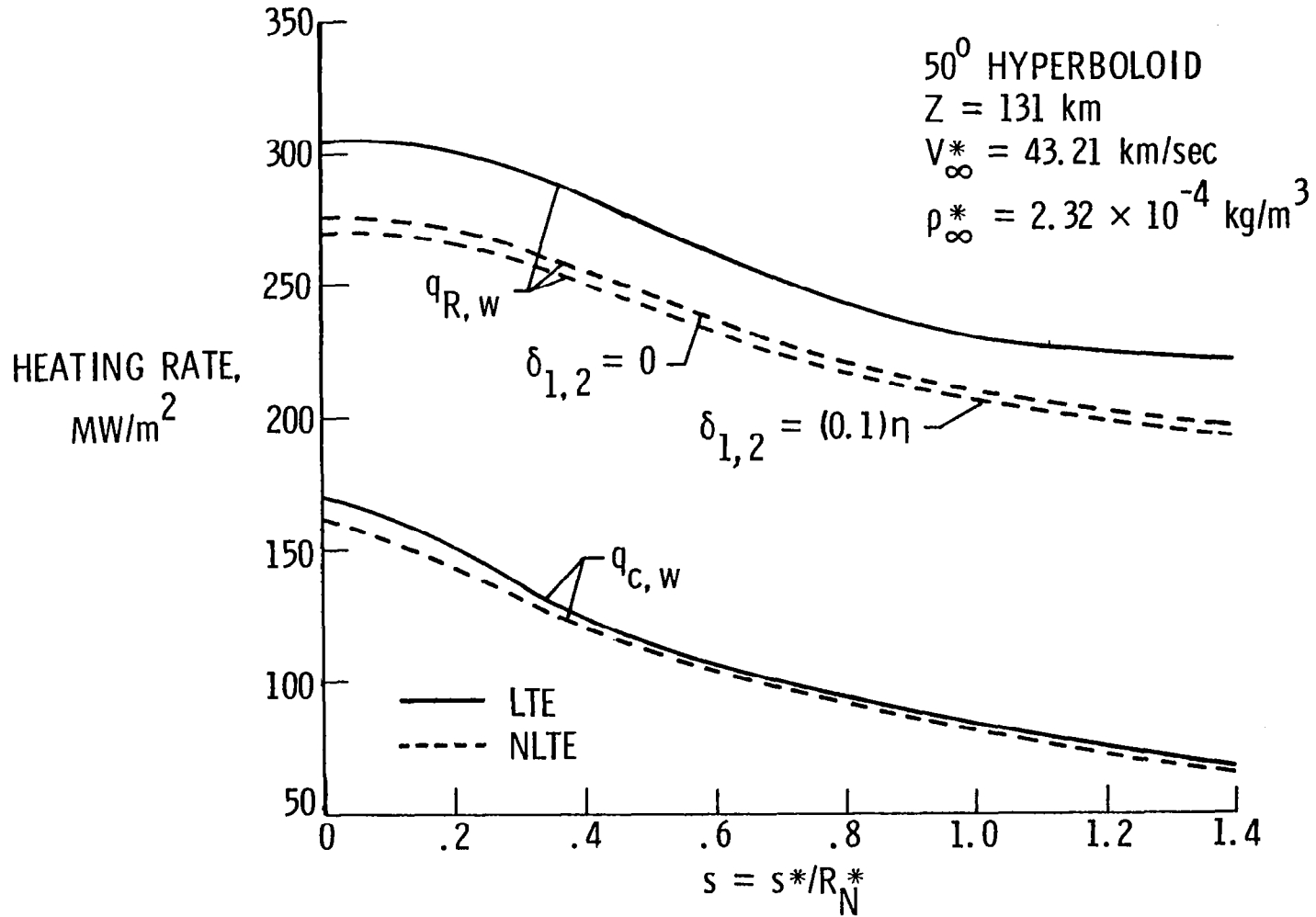small away from the stagnation point.

Figure 28. Radiative and convective heating along the body for entry conditions at Z = 131 km, H-H and H^+-H^+ collisions.
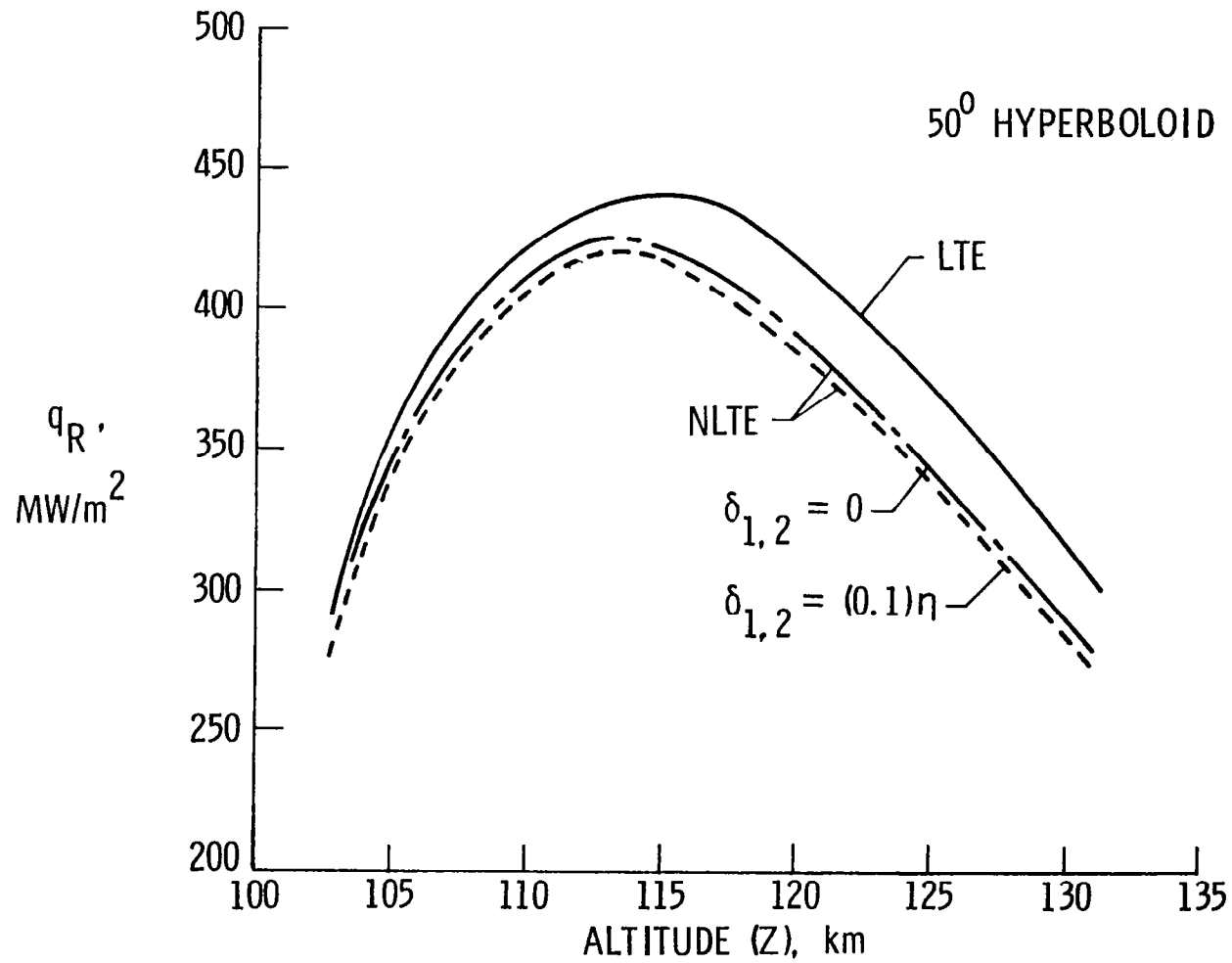
Figure 29. Stagnation-point radiative heating for different entry altitudes, H-H and H^+-H^+ collisions.

Results of LTE and NLTE radiative heating at the stagnation point
are shown in figure 29 for entry conditions at different altitudes.
The NLTE results again are obtained by considering the combined H-H
and H^+-H^+ collisions. Once again, the NLTE results for two-level
energy transitions are presented for comparative purposes. The results
show that differences between LTE and NLTE heating rates are larger at
higher altitudes. As mentioned earlier, this is because the densities
of participating species are relatively lower at higher altitudes (lower
pressures), and this, in turn, results in longer collisional deactivation
times.

NLTE results for a 55-degree sphere cone. - For the 55-degree
sphere cone, the radiative heating results for the peak heating condi-
tions are illustrated in figure 30. The NLTE results were obtained by
considering the combined H-H and H^+-H^+ collisional process. Because of
the numerical instability, it was possible to obtain accurate NLTE
results only up to the tangency point. Obviously, further work is
needed to improve the numerical procedure for obtaining the NLTE results
toward the downstream regions. In the stagnation region, the results
for the sphere cone show essentially the same trend as for the hyper-
boloid. At the stagnation point, the difference between the LTE and
NLTE results for the sphere cone is about the same as for the hyper-
boloid. This clearly indicates that the NLTE results are not
influenced significantly by the changes in forebody shapes. However,
further work is needed to make this a definite recommendation because
the LTE heating rates are influenced by the shape change (refs. 26, 27).

The results presented herein indicate that, although the relaxation
times for collisions between neutral particles decrease with increasing
temperature, the reverse is true for the charged particles. It is also
noted that the physically realistic collisional process for the shock-
layer gas (in the absence of ablative products) is the combined H-H and
H^+-H^+ deactivation process. Specific results indicate that NLTE effects
are greater closer to the body than near the shock. This is because the
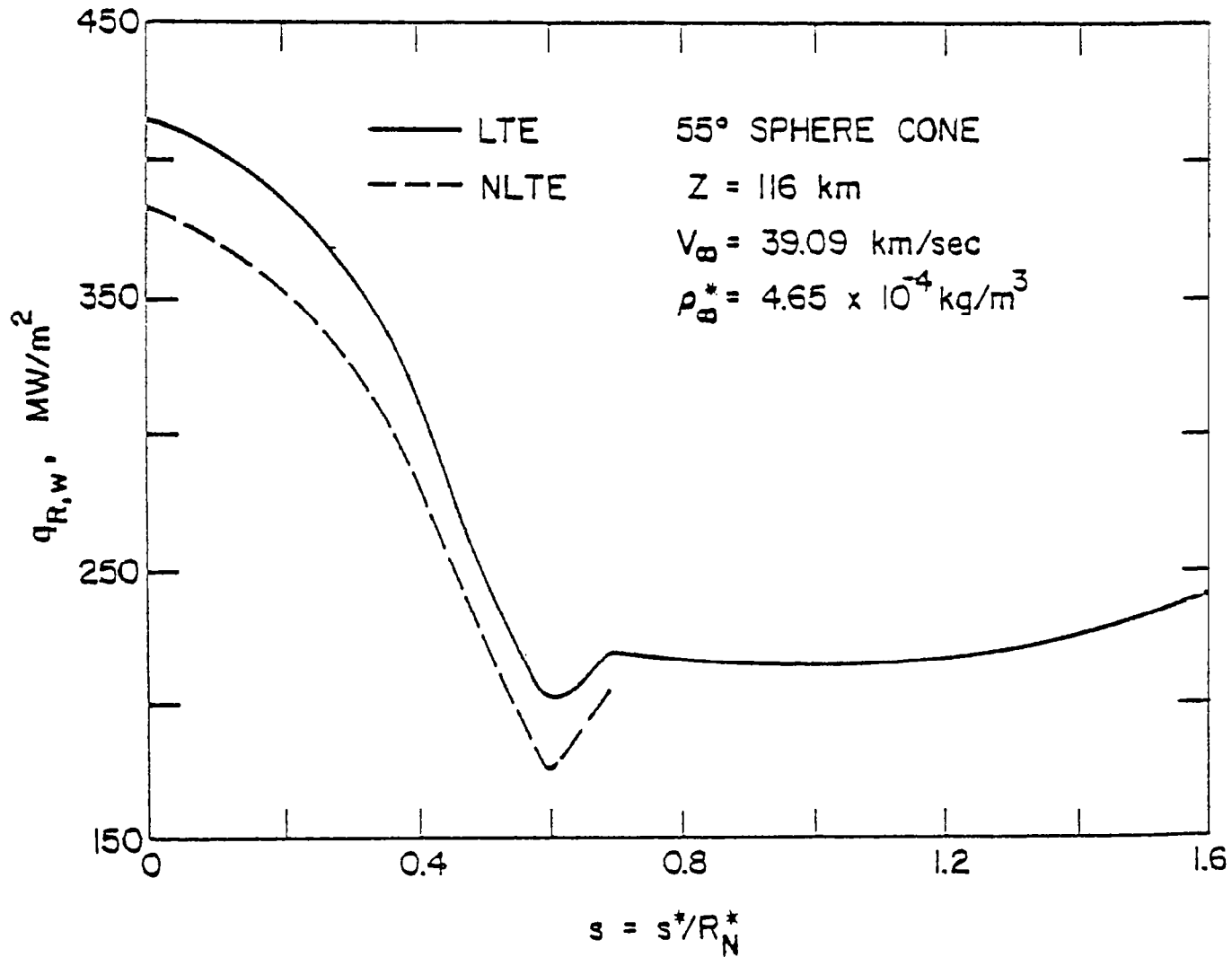NLTE results are influenced strongly by the temperature distribution in

Figure 30.   Radiative heating along the body (55° sphere cone) for entry conditions at Z = 116 km, H-H and H^+-H^+ collisions.

the shock layer and the effects are lower at higher temepratures. It
is further noted that the contribution of higher level energy transitions
on the NLTE results is relatively small for all entry conditions. It
is found that the influence of NLTE, in general, reduces the convective
and radiative heating to the entry body. Although this effect is small
for the convective heating, the radiative heating is influenced signif-
icantly. The NLTE effects are greater for higher altitude entry
conditions. A qualitative comparison of the results for a 50-degree
hyperboloid and a 55-degree sphere cone (under identical physical and
entry conditions) shows that the NLTE results are not influenced
significantly by the change in the forebody configurations of the entry
probe.

Importance of NLTE Radiation with Ablation Injection

To investigate the importance of NLTE radiation, the results were obtained only for a 35-degree hyperboloid (with coupled ablation mass loss from a carbon-phenolic heat shield). This is because, for this case, LTE results were already available in the literature (refs. 36 - 39). For comparative purposes, selected NLTE results were also obtained for the case with no ablative products (i.e., for $\dot{m} = 0$). The NLTE results, in this case, were obtained by considering the combined collisional deactivation process of H-H and H^+-H^+. Viscous shock-layer results obtained for the peak-heating conditions are presented in this subsection.

As discussed earlier (under "Radiative Lifetimes and Collisional Processes for the Shock-Layer Gases"), for NLTE study, it is essential to know the nature of the collisional deexcitation processes and relaxation times of different shock-layer species in presence of the ablative products. Figure 31 illustrates the important species concentrations near the wall influencing the C_2 collisional process. In general, the C_3 molecules are concentrated near the wall and the number density rapidly reduces away from the wall as they dissociate into C_2 and atomic carbon.

In the presence of the ablative products, the relaxation times for the combined collisional process of C_2-C_2, C_2-C, C_2-H, and H-H were used in the present study. The majority of NLTE results were obtained by using the combined radiative lifetimes of the Swan, Freymark, and Mulliken band system as indicated by η_r (III) under "Radiative Lifetimes and Collisional Processes for the Shock-Layer Gases." However, some results for radiative heating rates were also obtained by using the other radiative lifetimes of the band system as indicated by η_r (I), η_r (II), and η_r (IV).

The temperature variation across the shock-layer (for location s = 0) is shown in figure 32 for both LTE and NLTE (III) conditions. Results with no mass injection are also shown here for comparison. As would be expected, the shock-layer temperature,
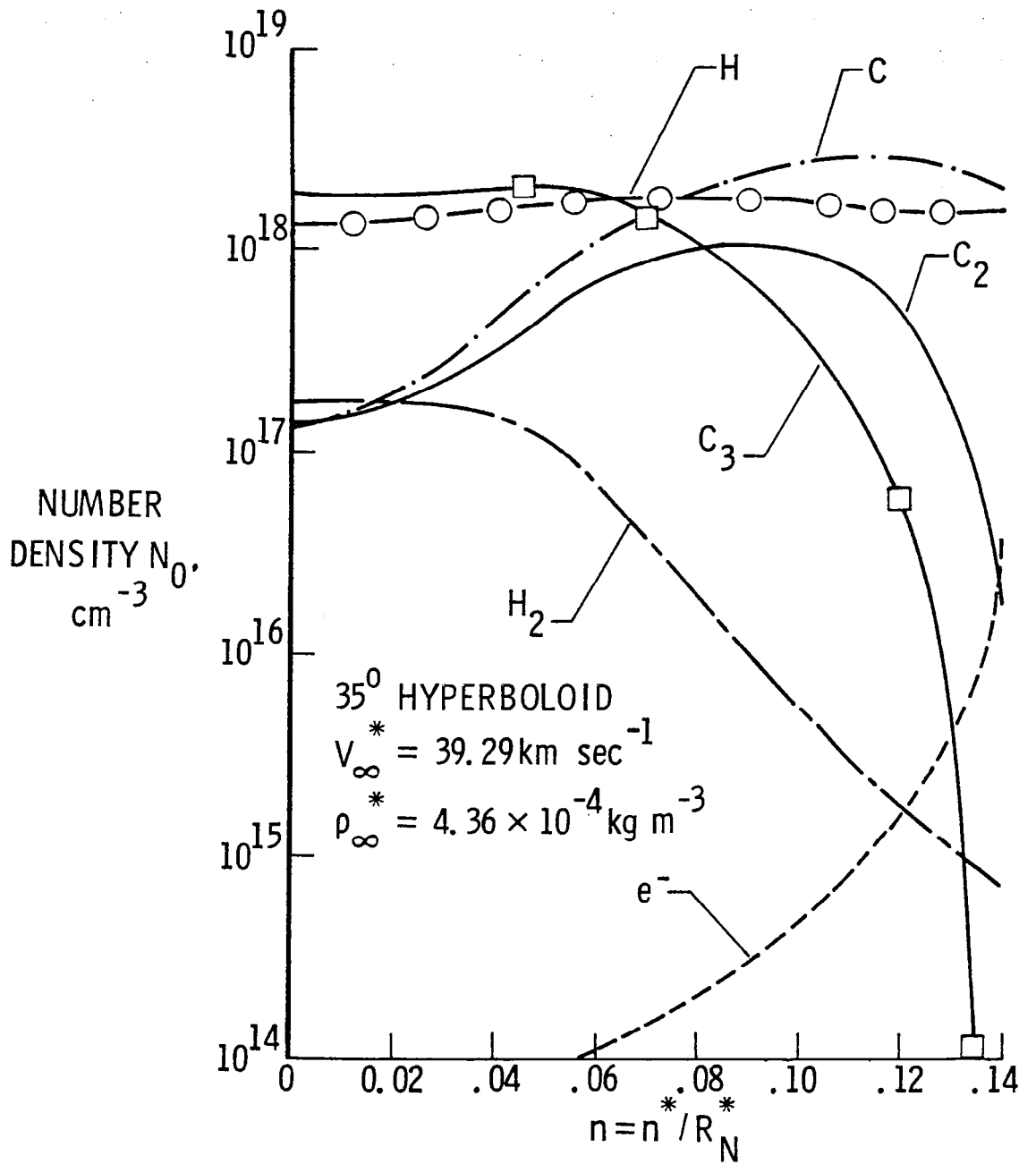
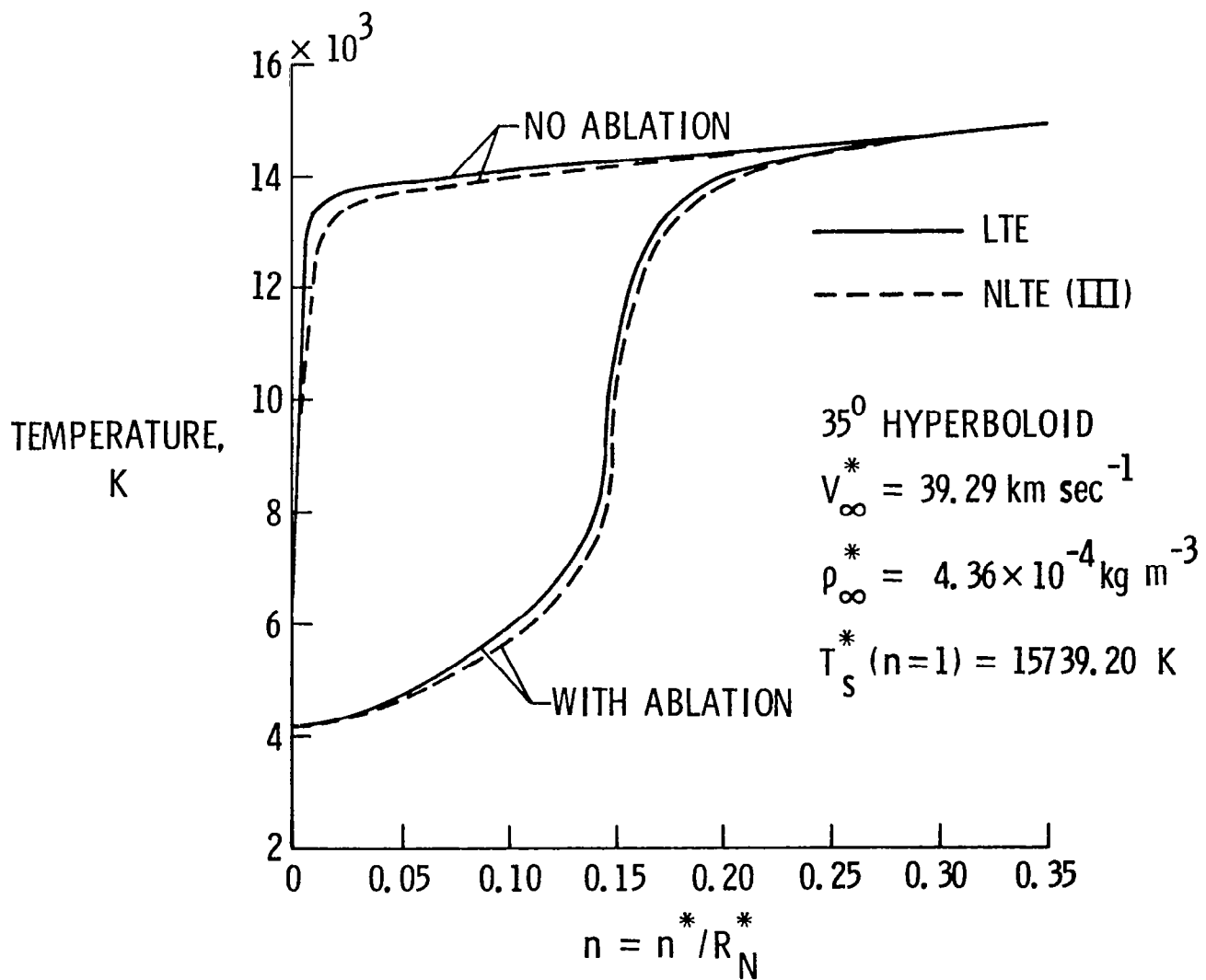Figure 31. Species concentrations in the vicinity of the wall.

Figure 32.   Temperature distribution across the shock layer.

in general, is lower in the vicinity of the body in the presence of the ablative products (refs. 36 - 39). It is seen that the NLTE temperature distribution is lower than the equilibrium values throughout the shock layer. A maximum difference of 5.48 percent is noticed between the 2 values at n = 0.13. The C_2 molecules in the ablation layer (a region in the vicinity of the wall), which absorb less under NLTE conditions, possess less energy than the equilibrium value. This, in turn, results in lower temperature values in the ablation layer, and the trend continues in the entire shock layer.

Figure 33 illustrates the density and enthalpy variations across the shock layer for LTE and NLTE (III) conditions. The enthalpy variation has a similar trend as the shock-layer temperature shown in figure 32. It was found that NLTE essentially had no influence on the pressure distribution in the shock layer. The density, however, is seen to be significantly higher for the NLTE case. This is a direct consequence of relatively lower NLTE temperatures in the shock layer. A maximum increase in density of about 5.5 percent is noticed at n = 0.15.

The equilibrium and nonequilibrium shock-standoff variation with distance along the body surface is shown in figure 34 for cases with and without ablation injection. As noted earlier, the shock-standoff distance is not influenced significantly by the NLTE conditions for the case with no ablation injection. For the case with ablation injection, however, the NLTE (III) results are comparatively higher than the LTE results. A possible reason for this behavior is the combination of enthalpy and density variation in the shock layer along with the energy loss at the shock for nonequilibrium conditions.

Variations in the nondimensional surface pressure and heating rate along the forebody of the probe are illustrated in figure 35. These quantities are nondimensionalized by their respective stagnation values of $p_{w,o}^* = 6.309$ atm, $q_{w,o}^*$ (LTE) = 201.849 MW/m^2, and $q_{w,o}^*$ (NLTE) = 208.927 NW/m^2. It is seen that NLTE virtually has no
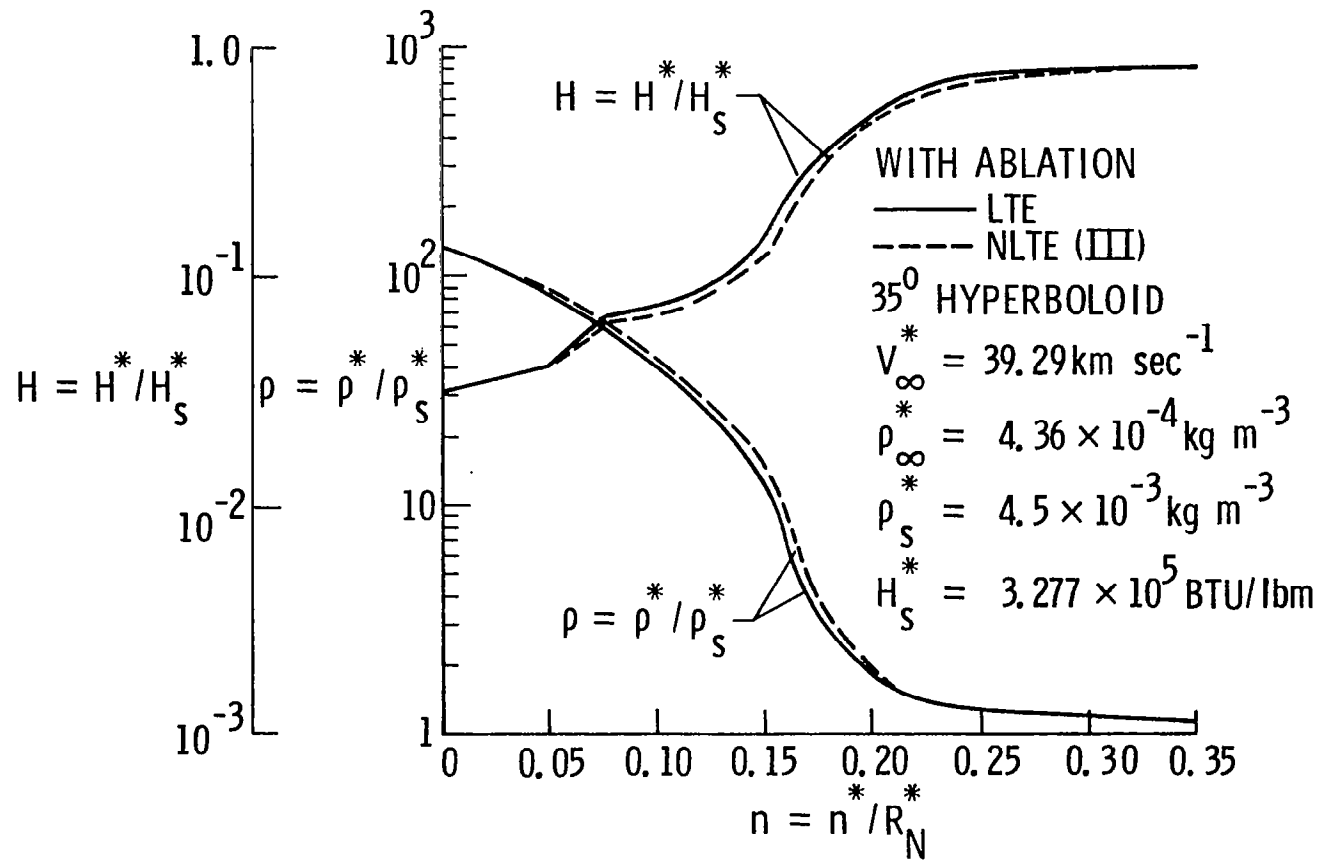
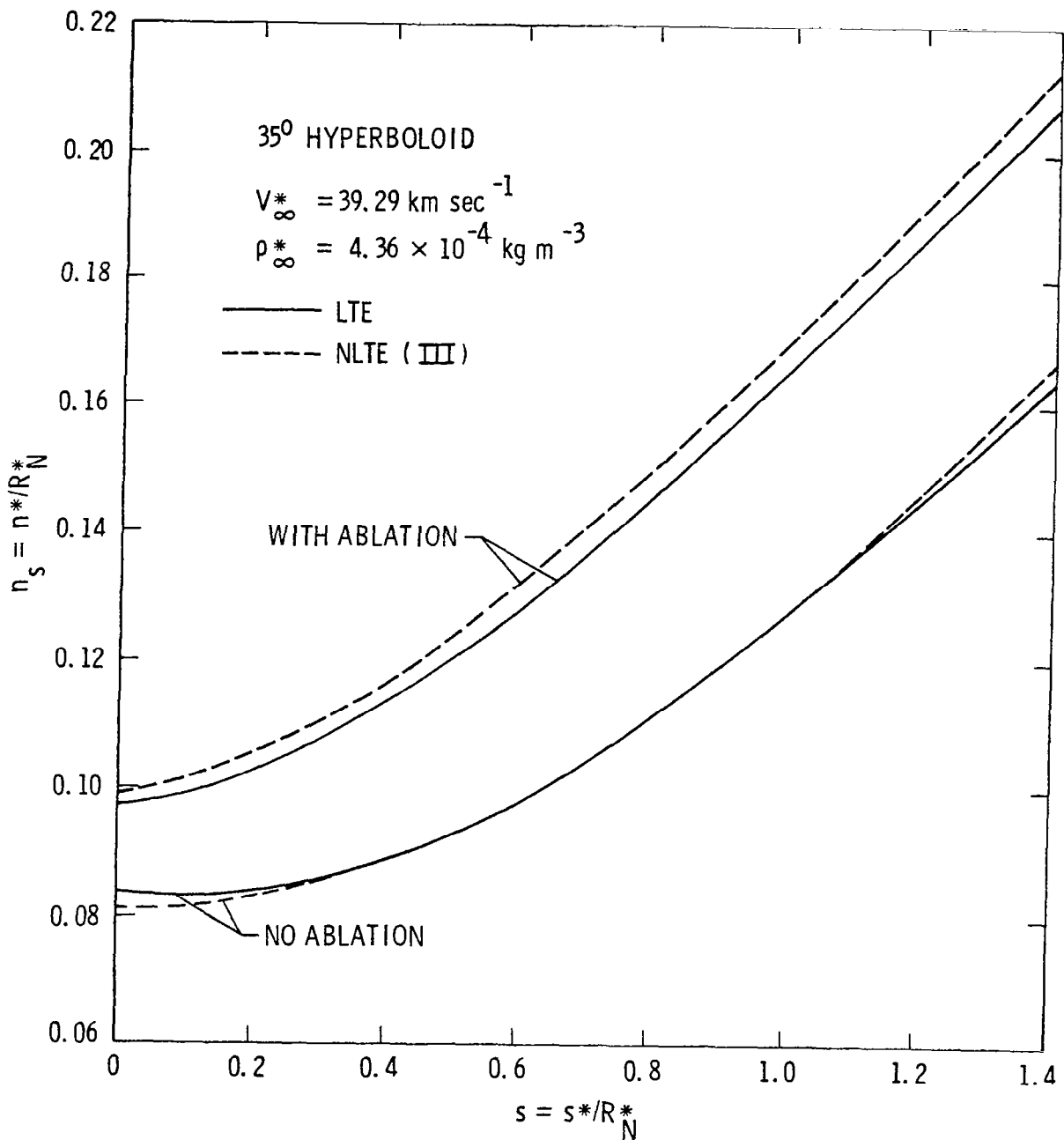Figure 33. Enthalpy and density variations across the shock layer.

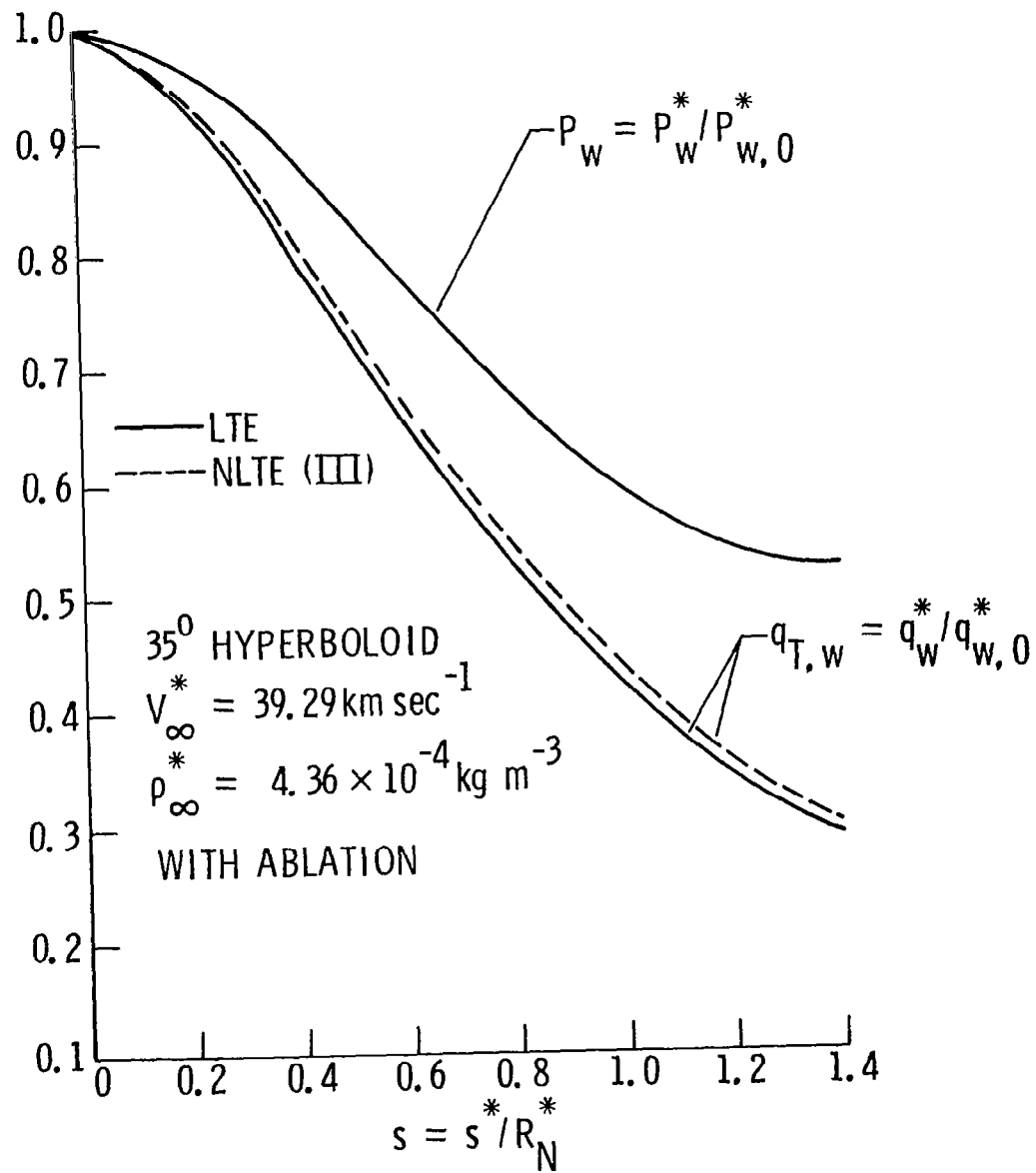Figure 34. Shock standoff variation with distance along the body surface.

Figure 35. Pressure and heating rate variations along the body surface.

influence on the pressure distribution. However, the total heating rate (convective plus radiative) is increased significantly under NLTE conditions. The main contribution to the total surface heating was found to be the radiative heating. The explanation of increased NLTE radiative heating, in this case, is given in the discussion of results presented in figure 36.

The results of radiative heating rates for different conditions are given in table 5 and are shown in figure 36. The LTE and NLTE (III) results are compared in figure 36(a) for the cases with and without ablation injection. The results clearly indicate that the radiative heating to the body, in general, is reduced significantly in the presence of the ablative products. For the case with no ablation, the NLTE results are found to be significantly lower than the LTE results; a decrease of about nine percent is noted at the stagnation point. In the presence of the ablative products, however, the results presented in figure 36 and table 5 show that NLTE results are comparatively higher than the LTE results. The reason for this is as follows: Under NLTE conditions, the number of C_2 molecules in the ground state (that are capable of absorbing the incoming radiation from the shock-layer gases) is less as compared to the LTE values (i.e., the number based on the Boltzmann distribution). This increases the transparency of the ablation layer which, in turn, results in higher heating of the entry body. This reverse trend in the NLTE heating rate is an important finding of this study. The results for the NLTE heating rate obtained by considering different radiative lifetimes are illustrated in figure 36(b). The results for cases η_r (II) and η_r (III) were found to be about the same for all body locations (see table 5). The results for η_r (I) are seen to give the smallest increase in NLTE heating whereas the results for η_r (IV) provide the maximum heating rate to the body. These NLTE results, however, do not differ from each other considerably. The maximum increase in the stagnation-point heating is found to be about 3.5 percent for η_r (III) and about 5 percent for η_r (IV). Thus, based on the information of radiative
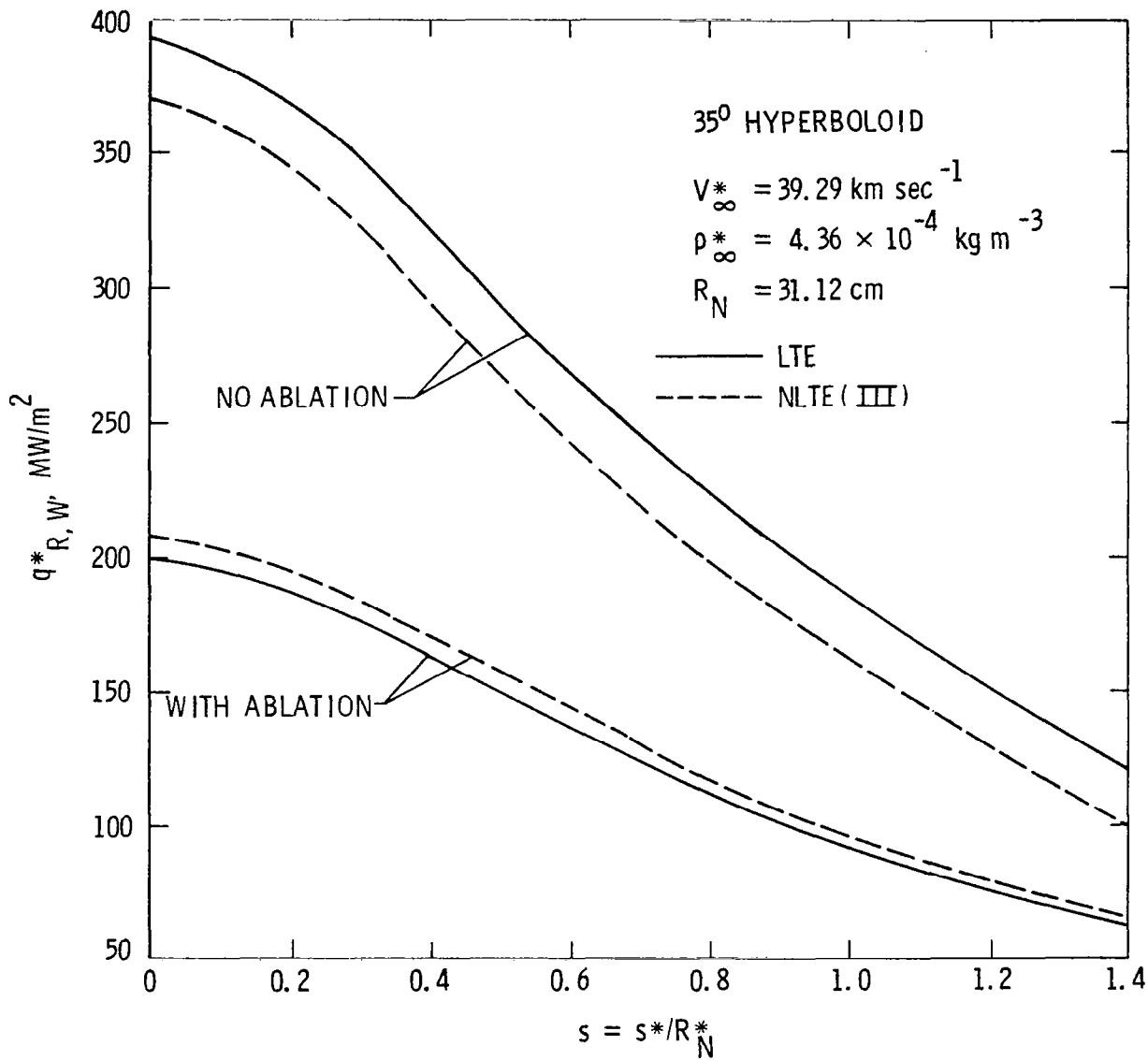
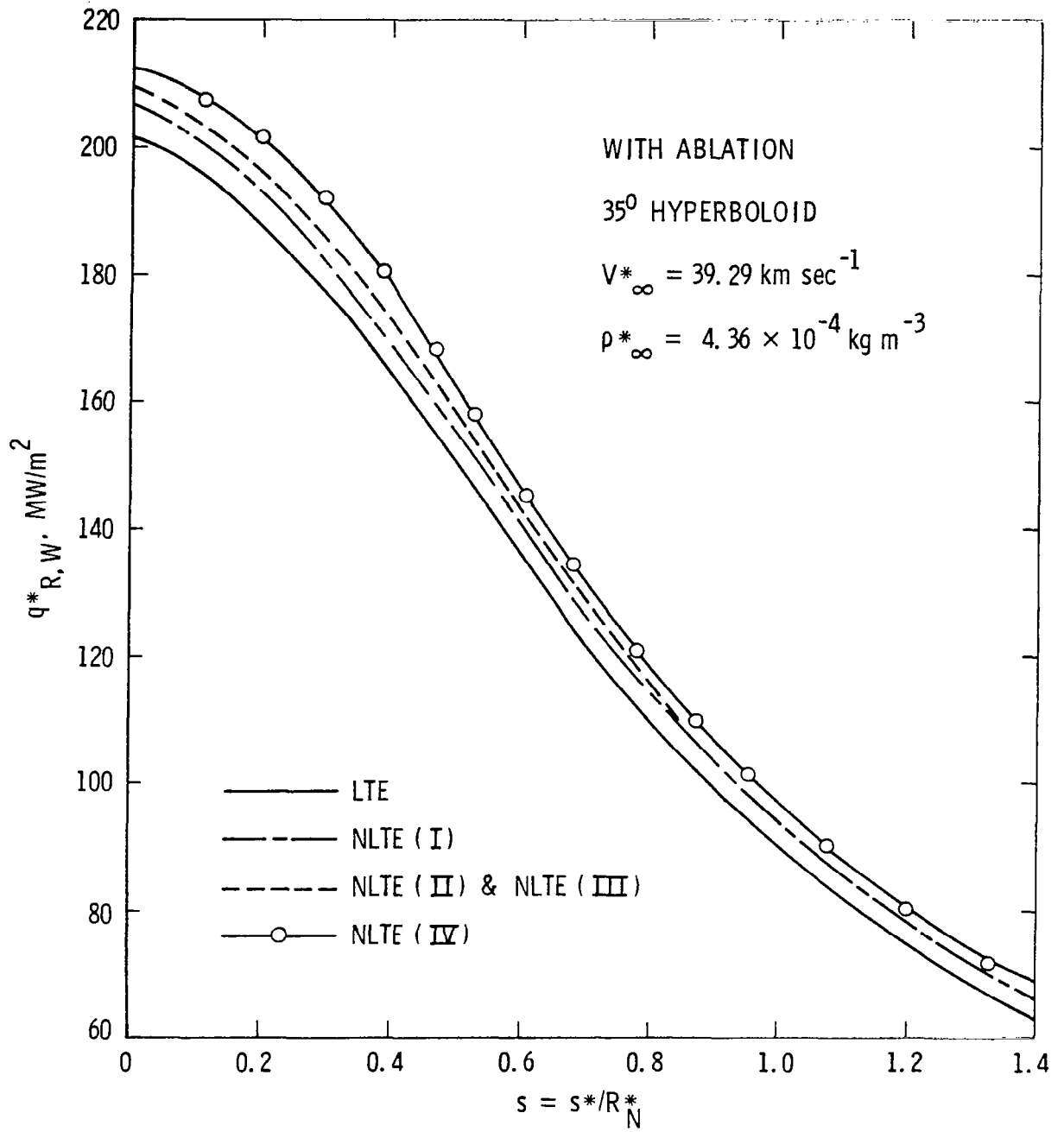Figure 36(a). Variation of radiative heating rate along the body surface (with and without ablation).

Figure 36(b). Comparison of LTE and NLTE radiative heating rates along the body surface with ablation.

lifetimes of the C_2 band system available at the present time, it may be concluded that the NLTE effects will be maximum for the combined radiative lifetime represented by n_r (IV), and this will increase the radiative heating to the body by a maximum of about five percent.

The ablation mass loss rate from the body surface is shown in figure 37. As would be expected, the mass loss rate is higher under the NLTE conditions (because of the increased heating rates to the body).

In conclusion, the results presented here indicate that the temperature and enthalpy distribution in the shock layer are lower under the NLTE conditions. The NLTE increases the density in the shock layer, but it has no influence on the pressure variation. The radiative heating to the entry body is increased significantly because of NLTE and this, in turn, results in increased mass loss from the body.

Table 5. Wall radiative heat flux for the case with ablation under LTE and NLTE conditions.

| $s = s^*/R_N^*$ | Wall Radiative Heat Flux q_r^*, MW/m^2 | | | | |
	$q_R^*(LTE)$	$q_R^*(I)$	$q_R^*(II)$	$q_R^*(III)$	$q_R^*(IV)$
0.0	201.849	206.774	209.017	208.927	211.987
0.2	188.172	193.127	196.020	195.891	201.497
0.4	164.709	169.658	173.278	173.127	178.165
0.6108	135.040	139.244	141.497	141.543	144.782
0.7854	110.900	114.765	115.900	115.974	120.841
1.200	75.012	78.767	80.256	79.012	80.572
1.500	58.271	61.813	61.570	61.902	62.090
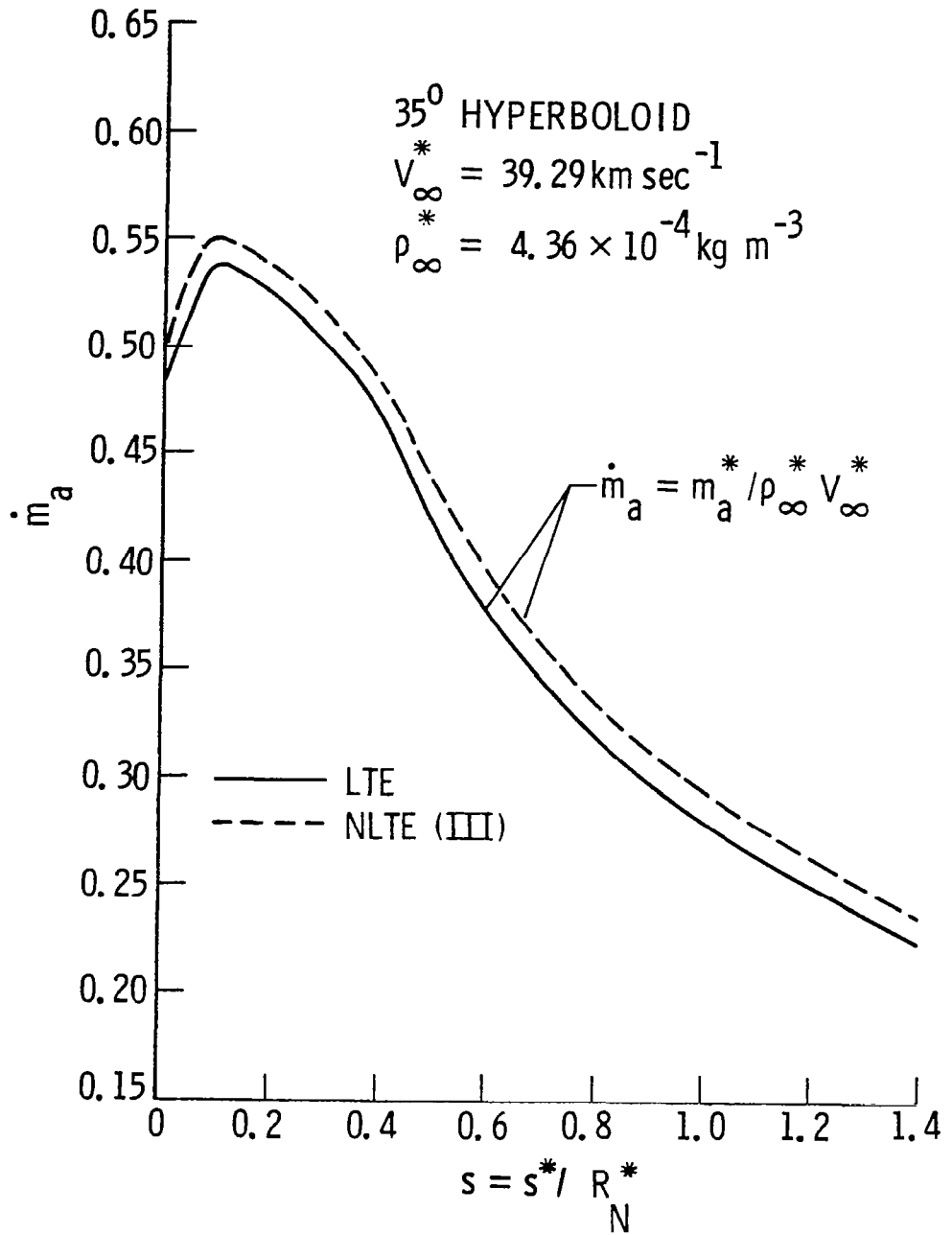
Figure 37. Ablation mass loss rate along the body surface.

The figure shows a graph with the vertical axis labeled $\dot{m}_a$ ranging from 0.15 to 0.65, and horizontal axis labeled $s = s^*/R_N^*$ ranging from 0 to 1.4.

Annotations on the graph:

35^0 HYPERBOLOID

$V_\infty^* = 39.29 \, \text{km sec}^{-1}$

$\rho_\infty^* = 4.36 \times 10^{-4} \, \text{kg m}^{-3}$

$\dot{m}_a = m_a^* / \rho_\infty^* V_\infty^*$

——— LTE

– – – NLTE (III)

114

Effect of Probe Shape Change on the Flow Phenomena

The shock shape and shock-standoff distance are influenced greatly by the shape of the entry body. To study the influence of shape change on flow phenomena around the entry body, it is essential to specify several speculative profiles that will emerge from mass loss and recession of the heat shield just after the peak heating phase of the entry mission. This is important because the main data collection phase of the mission starts after the heating phase. At this stage, it is essential to consider the actual shape of the probe rather than the initial shape in investigating the flow field and aerodynamic stability of the entry body. It is necessary, therefore, to have analytic expressions that are capable of generating such desired shapes. A general relation for the shape change can be given by a quadratic form as

$$y = 2R_N x - Bx^2 \qquad\qquad\qquad (118)$$

where B represents the bluntness factor which determines the body shape. For negative values of B, the resulting shapes are a family of hyperbolas. For B = 1, circular or spherical shapes are obtained. A family of parabolas is obtained for B = 0, and positive values of B give elliptical shapes.
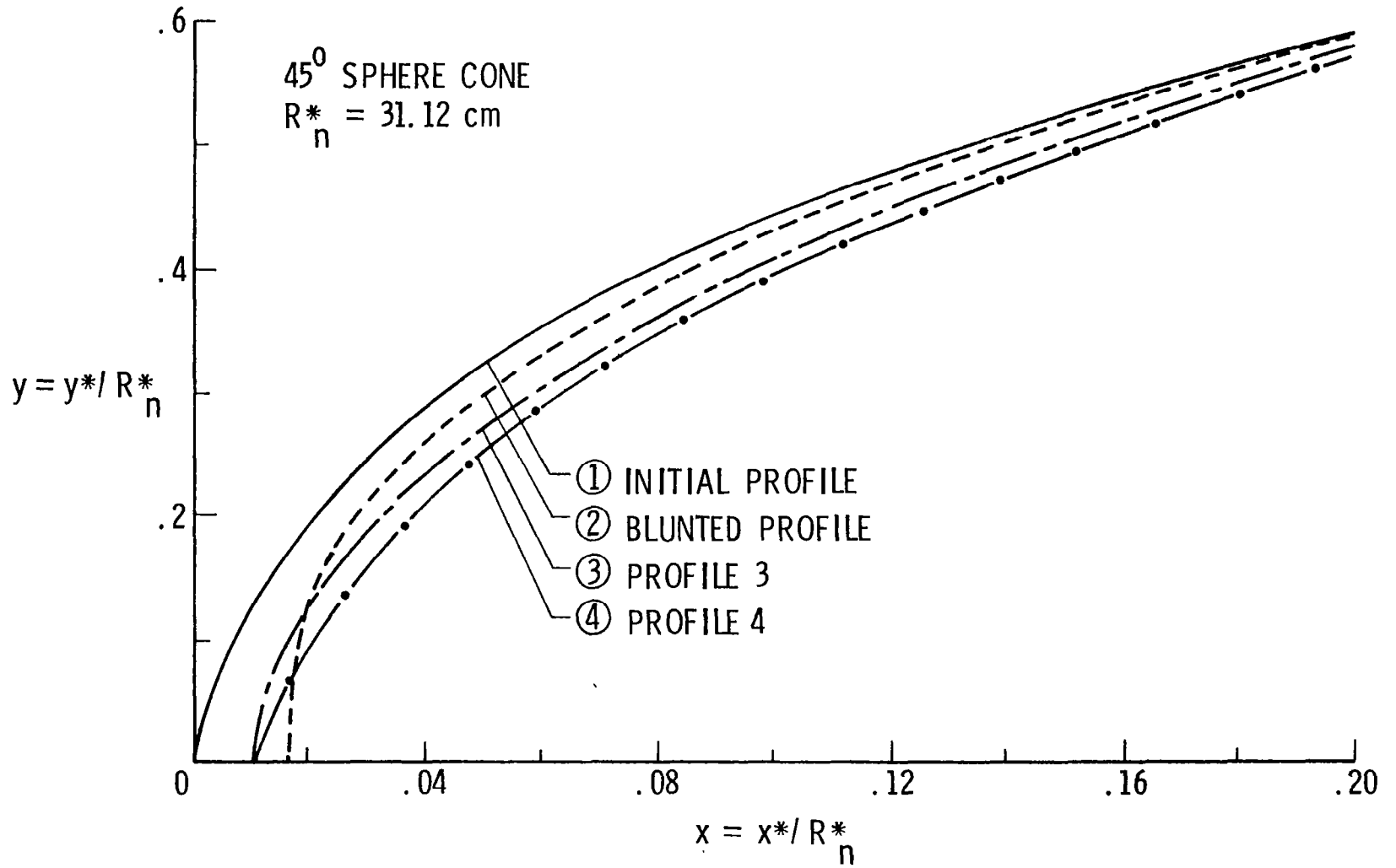
Equation (118) is used in generating different shapes for the entry probe. The initial body shapes considered for this study are a 45-degree sphere cone (i.e., a 45-degree half-angle, spherically capped, conical body), a 35-degree hyperboloid (i.e., a hyperbolic forebody shape with an asymptotic angle of $\theta = 35°$), and a 45-degree ellipsoid. The reason for selecting a 35-degree hyperboloid (instead of a 45-degree hyperboloid) is that the mass losses for this and the 45-degree sphere cone and 45-degree ellipsoid are comparable. For all initial shapes, the nose radius considered is 31.12 cm and the base radius is taken to be twice the nose radius. The final shape after the heating phase will depend upon the extent of absorption

of incoming radiation by the ablative products. If no radiation blockage is assumed, then it is possible to have severe recession of the forebody as well as of the afterbody. A 25 or 50 percent radiation blockage will result in relatively less severe blunting of the entry probe. It is possible to generate these speculative profiles with the help of equation (118).

The numerical procedure employed by Sutton et al. (ref. 26) for inviscid radiating flow is basically used in this study also. For the initial profile, the x and y coordinates, the distance along the body, and the radius of the curvature are specified at 14 selected stations along the body. For the changed profiles, the distance along the body, the radius of curvature, and the body angle are calculated at each station by using a subroutine with x and y coordinates as inputs. A three-point central differencing scheme is used for calculation of the s location, and a two-point backward differencing scheme is used for calculation of the curvature.
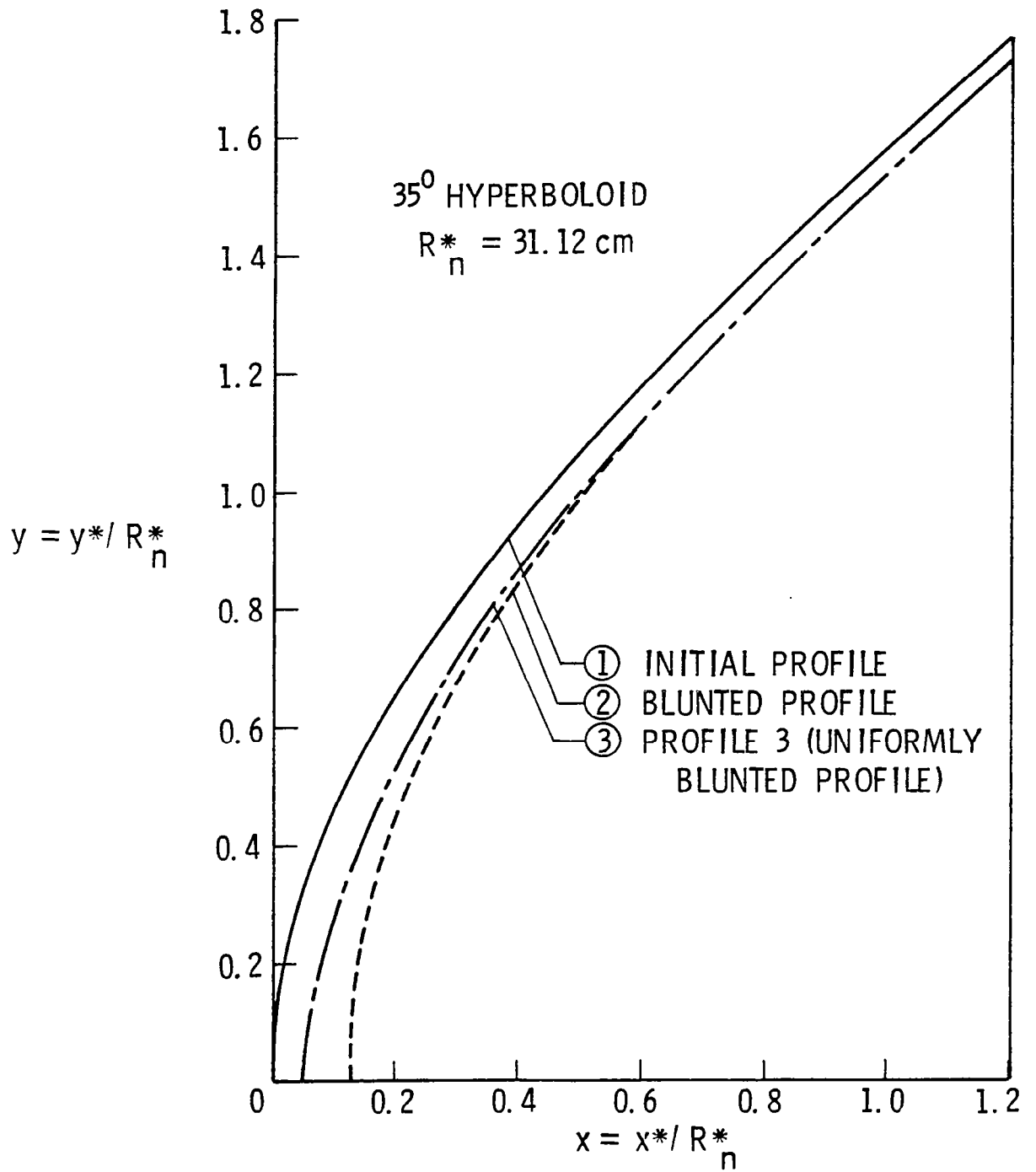
The three initial body shapes and the corresponding body profiles that emerge when the influence of shape change is considered are shown in figures 38(a) to (c). Figure 38(a) shows the forebody configurations of the 45-degree sphere cone in which profile 1 represents the initial shape and profile 2 is the corresponding blunted profile. Profile 2 represents a case where the entry body has experienced a severe blunting near the stagnation region as compared to the downstream region. Specifically, this represents a shape where the initial body has undergone a severe mass loss near the nose after absorbing about 50 percent of the incoming radiation. Profiles 3 and 4 in figure 38(a) represent two arbitrary blunted shapes for which the mass loss is assumed to be uniform all along the body. For all the forebody profiles shown in figure 38(a), the afterbody shape is a 45-degree half-angle cone.

Different configurations for the 35-degree hyperboloid are shown in figure 38(b). In this case also, the severely blunted profile is represented by the second curve. This corresponds to the case
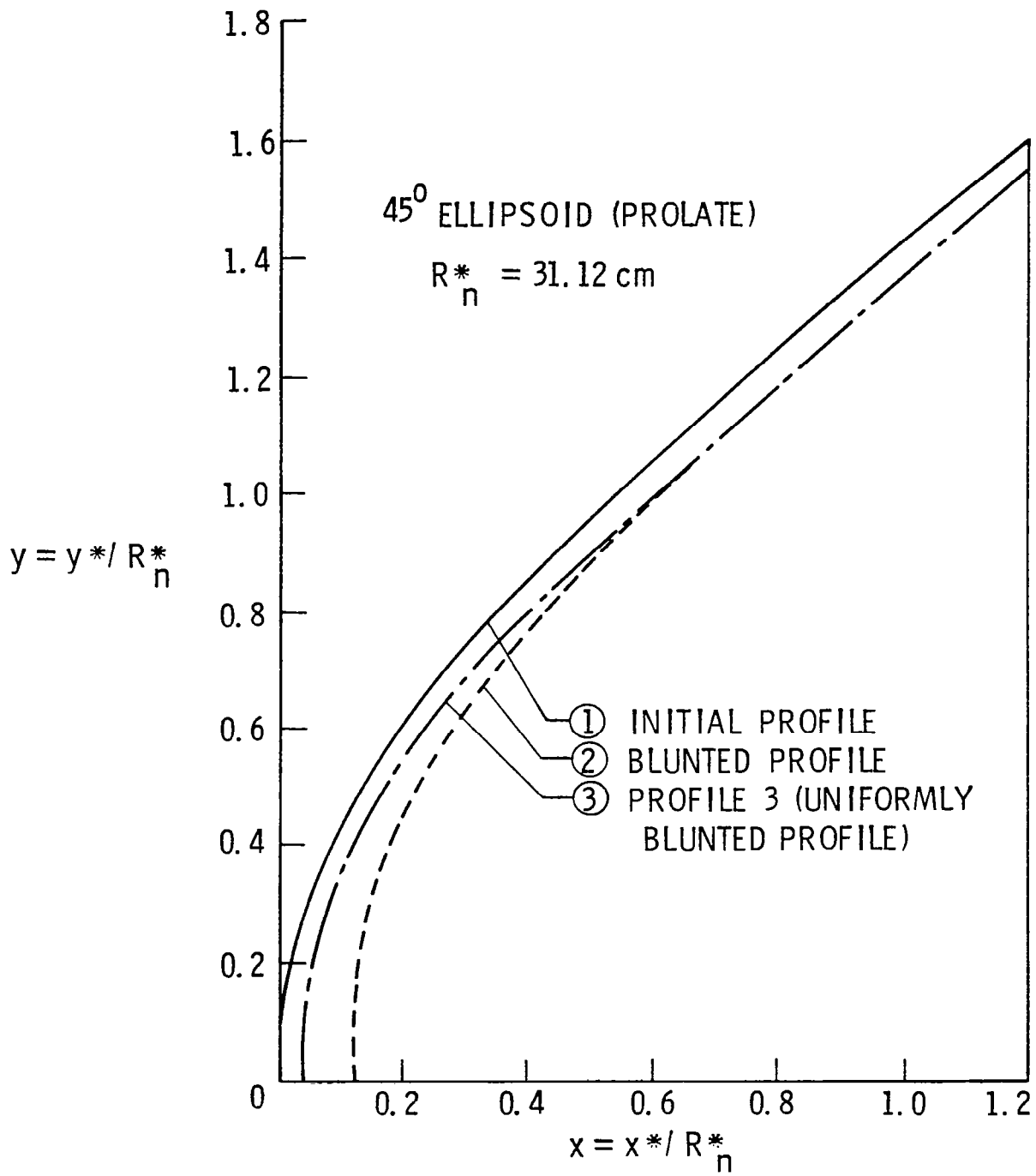
45^0 SPHERE CONE
$R^*_n = 31.12$ cm

$y = y^*/ R^*_n$

① INITIAL PROFILE
② BLUNTED PROFILE
③ PROFILE 3
④ PROFILE 4

$x = x^*/ R^*_n$

(a) for 45-degree sphere cone.

Figure 38. Forebody configurations.

35° HYPERBOLOID

$R_n^* = 31.12$ cm

$y = y^*/R_n^*$

① INITIAL PROFILE
② BLUNTED PROFILE
③ PROFILE 3 (UNIFORMLY BLUNTED PROFILE)

$x = x^*/R_n^*$

(b) for 35-degree hyperboloid.

Figure 38. (Continued).

(c) for 45-degree ellipsoid.

Figure 38. (Concluded).

of severe stagnation region mass loss with assumed radiation blockage of about 50 percent. Profile 3 in figure 38(b) represents the shape for 40 percent radiation blockage with uniform mass loss along the entire body. Different configurations for the 45-degree ellipsoid are shown in figure 38(c), and they correspond to exactly the same conditions as for the 35-degree hyperboloid.

The condition of LTE for the radiative transport was assumed while obtaining the results using different probe configurations. Since NLTE is a condition of the absorbing/emitting gases, it is assumed that the shape change will not influence the NLTE phenomena. The results have been obtained for different entry conditions, and they are presented here first for the 45-degree sphere cone and then for the 35-degree hyperboloid. Finally, the peak heating results for the 45-degree sphere cone and 35-degree hyperboloid are compared with peak heating results of the 45-degree ellipsoid.

Results for 45-degree sphere cone. - Different results obtained for the 45-degree sphere cone are illustrated in figures 39 to 46. The shock-standoff variation with distance along the body surface is shown in figures 39 and 40. For peak heating conditions (i.e. for Z = 116 km), results obtained for the four profiles indicated in figure 38(a) are illustrated in figure 39. Results obtained for the initial and blunted profiles are compared in figure 40 for the three entry conditions considered. The results indicate that blunting of the nose region increases the shock-layer thickness not only near the stagnation region but all along the body, although there is no significant change in the body shape near the flank region. It is evident from figure 39 that profiles 3 and 4 do not influence the shock-standoff distance appreciably. This is because the uniform mass loss tends to preserve the original configuration of the entry body. As would be expected, the shock-standoff distance, in general, increases with decreasing altitude, and near the stagnation region the influence of nose blunting is greater at lower altitudes.
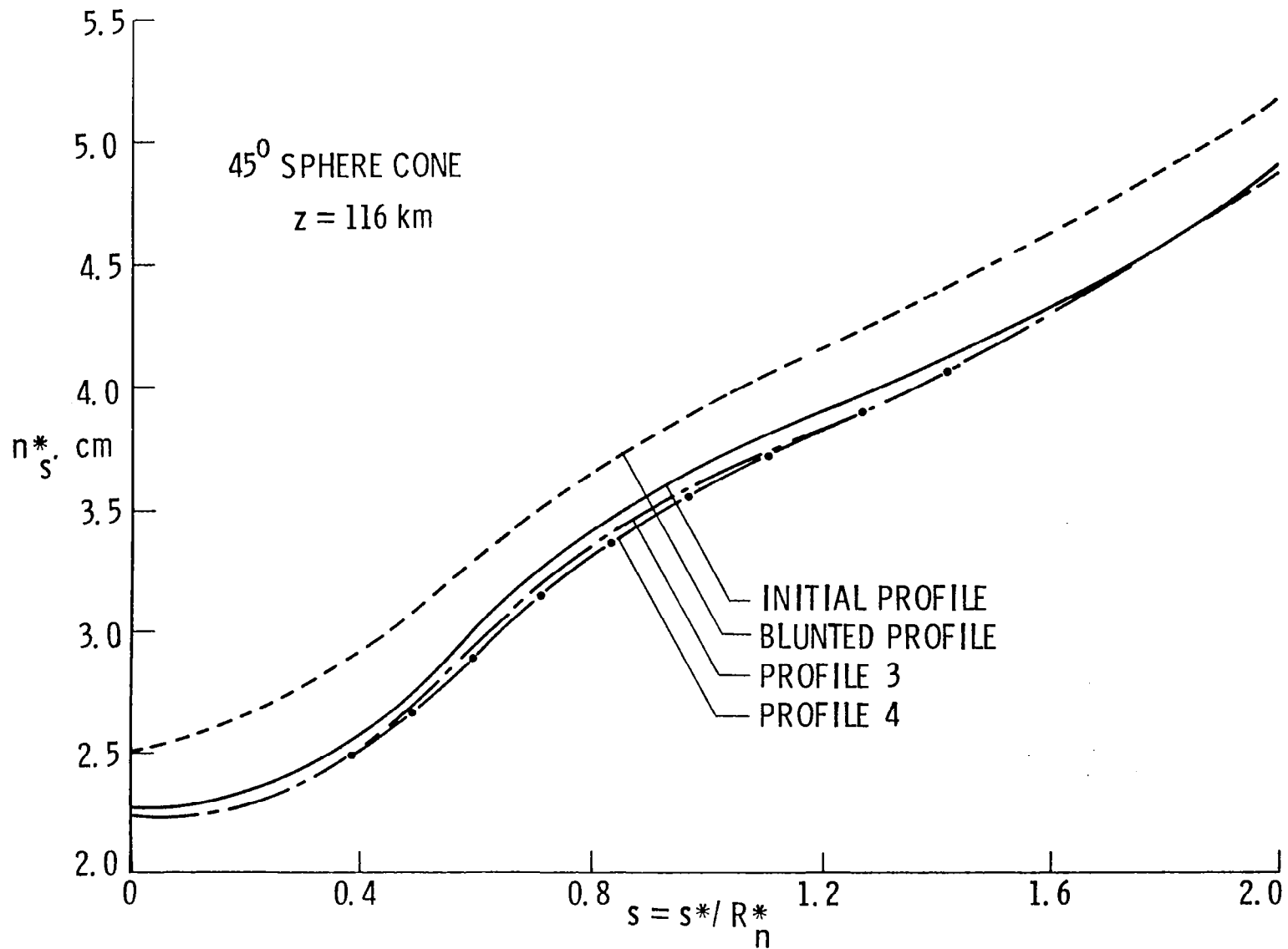
Figure 39. Shock-standoff variation for 45-degree sphere cone, Z = 116 km.
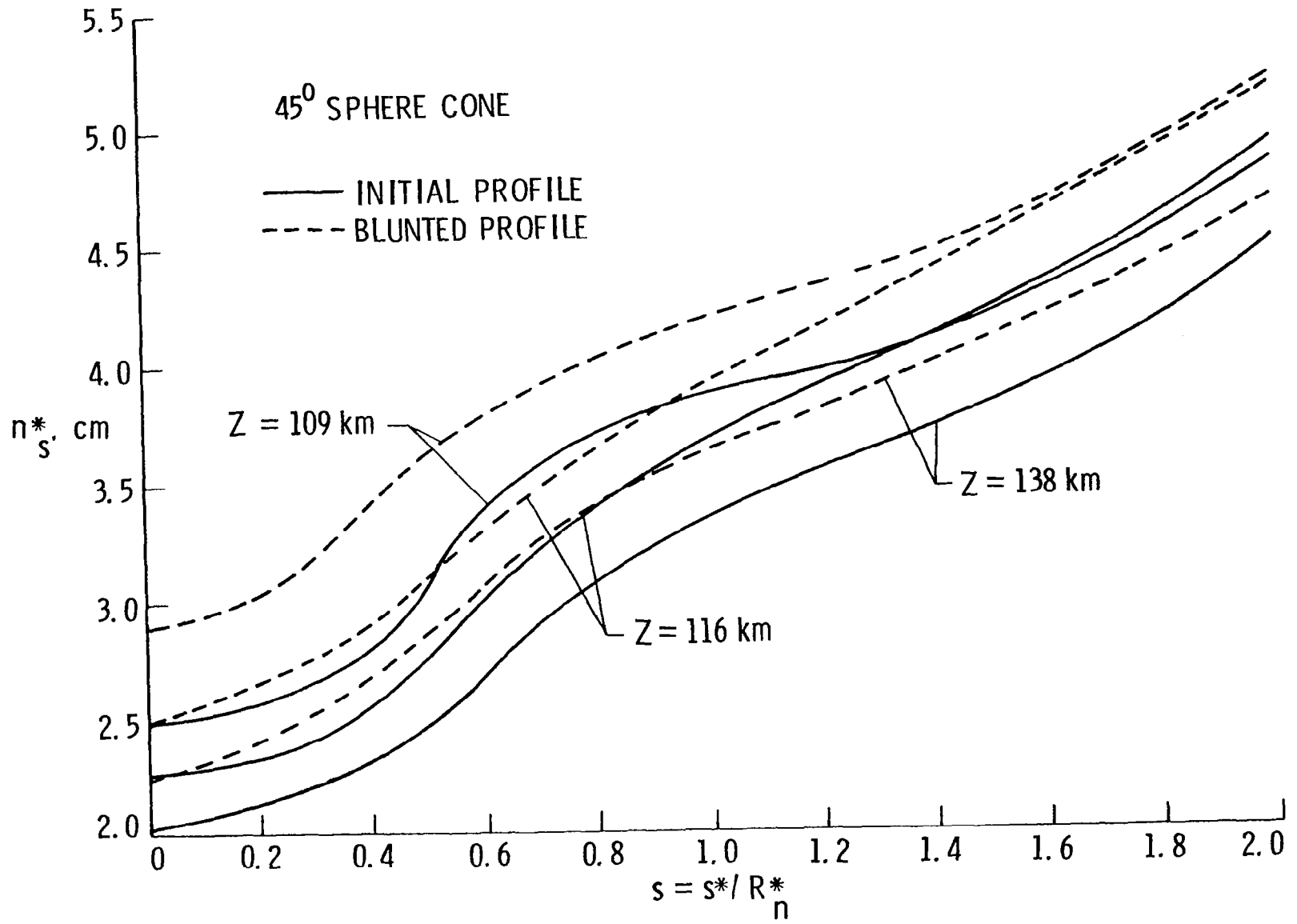
Figure 40.   Shock-standoff variation for 45-degree sphere cone.

Variation of the shock temperature (i.e., the temperature just behind the shock) with distance along the body surface is shown in figure 41 for the three entry conditions considered. For these conditions, the shock temperature, in general, is found to be higher for higher entry altitudes. The effect of blunting is seen to increase the shock temperature along most of the downstream region of the probe. For Z = 116 km, a maximum difference of 5.6 percent is found at the tangency point (where the forebody and the afterbody coincide asymptotically). The effect of blunting is seen to have relatively higher influence on the shock temperature for the other two entry conditions. Results of moderate shape change (with uniform mass loss), as shown by curves 3 and 4, indicate negligible influence on the shock temperature. Variation in density just behind the shock along the body surface is shown in figure 42 for 2 entry conditions, Z = 116 km and 138 km. In general, lower shock densities are associated with higher entry altitudes. This is because the free-stream densities are lower at higher altitudes. The shock-density variation is relatively higher for the blunted profile, and a significant increase is noted from the stagnation point to the tangency point. However, virtually no difference is seen after the location s = 1. For Z = 116 km, a maximum difference of 5.6 percent is noted between the initial and blunted profiles at location s = 0.8. This difference is even smaller (4.5 percent) for results at Z = 138 km. Results of profiles 3 and 4 are in general agreement with the results of the initial profiles; a maximum difference of 1.25 percent is noted at s = 0.8 for Z = 116 km.

Variations in density and v-velocity across the shock layer are shown in figures 43 and 44, respectively. Figure 43 shows the density variation for body locations (s = 0 and 1.4) and entry conditions (Z = 116 km and 138 km). It is seen that along the stagnation line the density is not influenced by the shape change. However, significant differences in results of the initial and blunted profiles are noted for the downstream location of s = 1.4. The density values are lower for the blunted profile because the temperatures are relatively higher. Uniform profile changes do not alter the density values
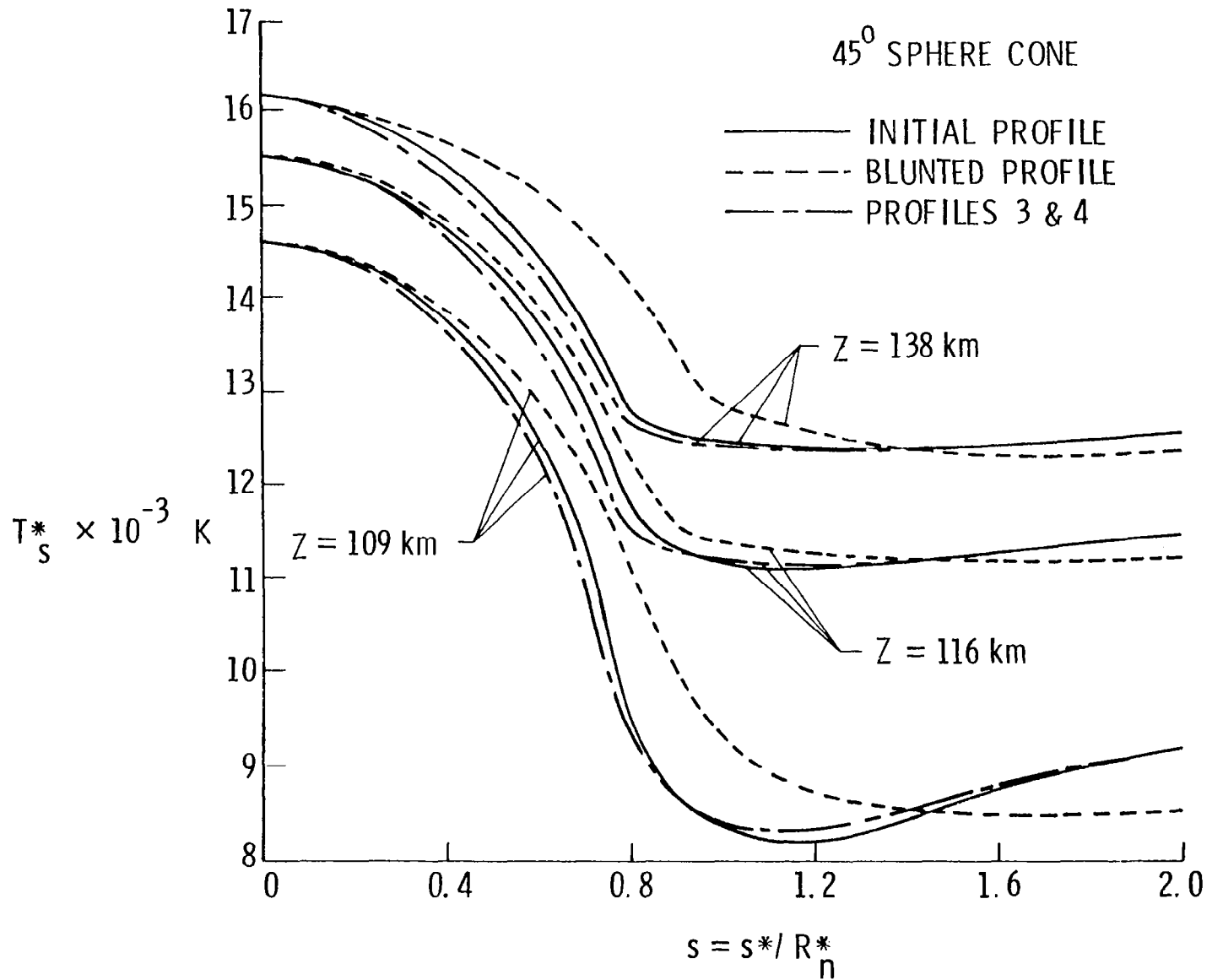
Figure 41. Variation of temperature just behind the shock for 45-degree sphere cone.
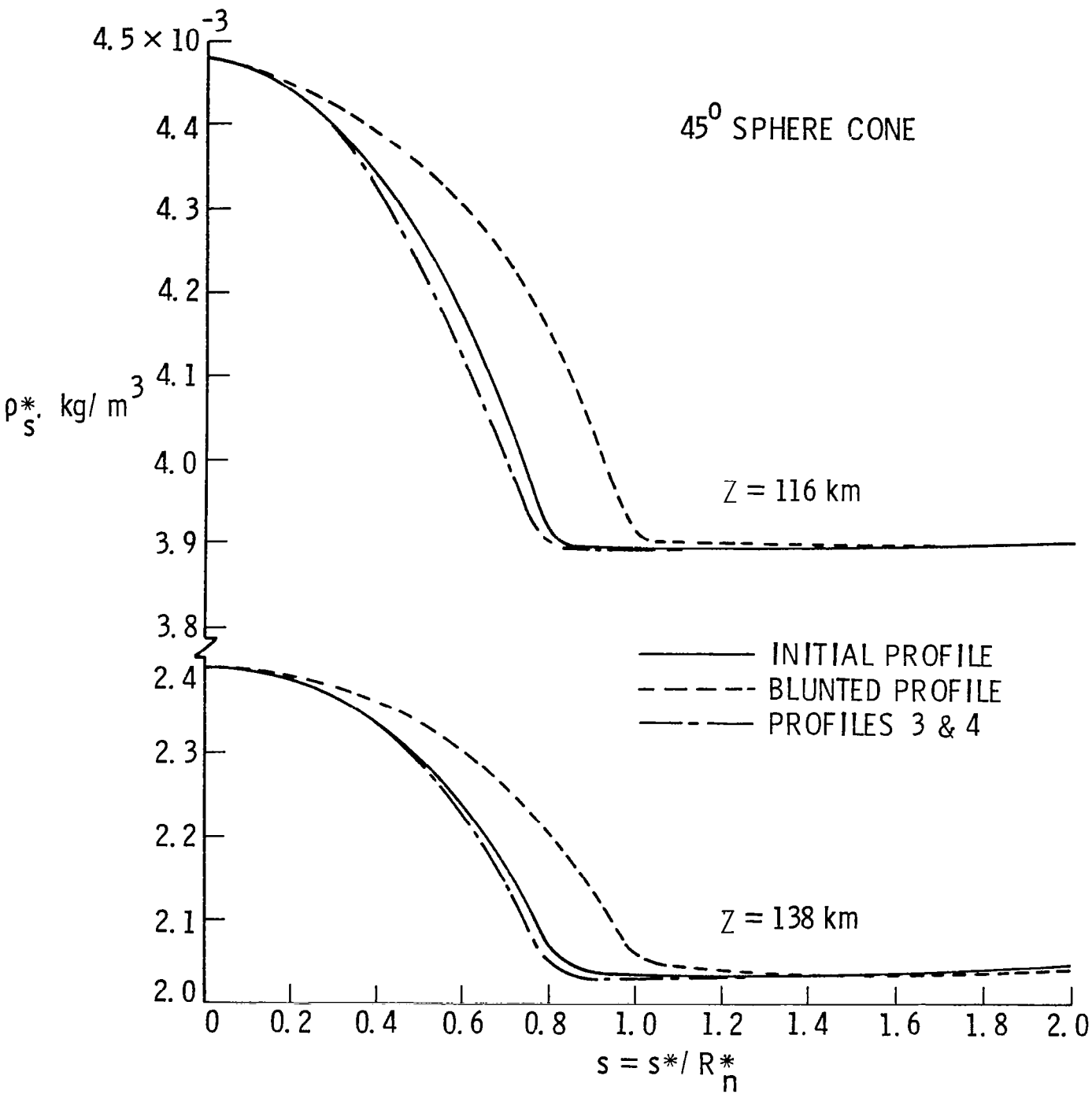
Figure 42. Variation of density just behind the shock for 45-degree sphere cone.
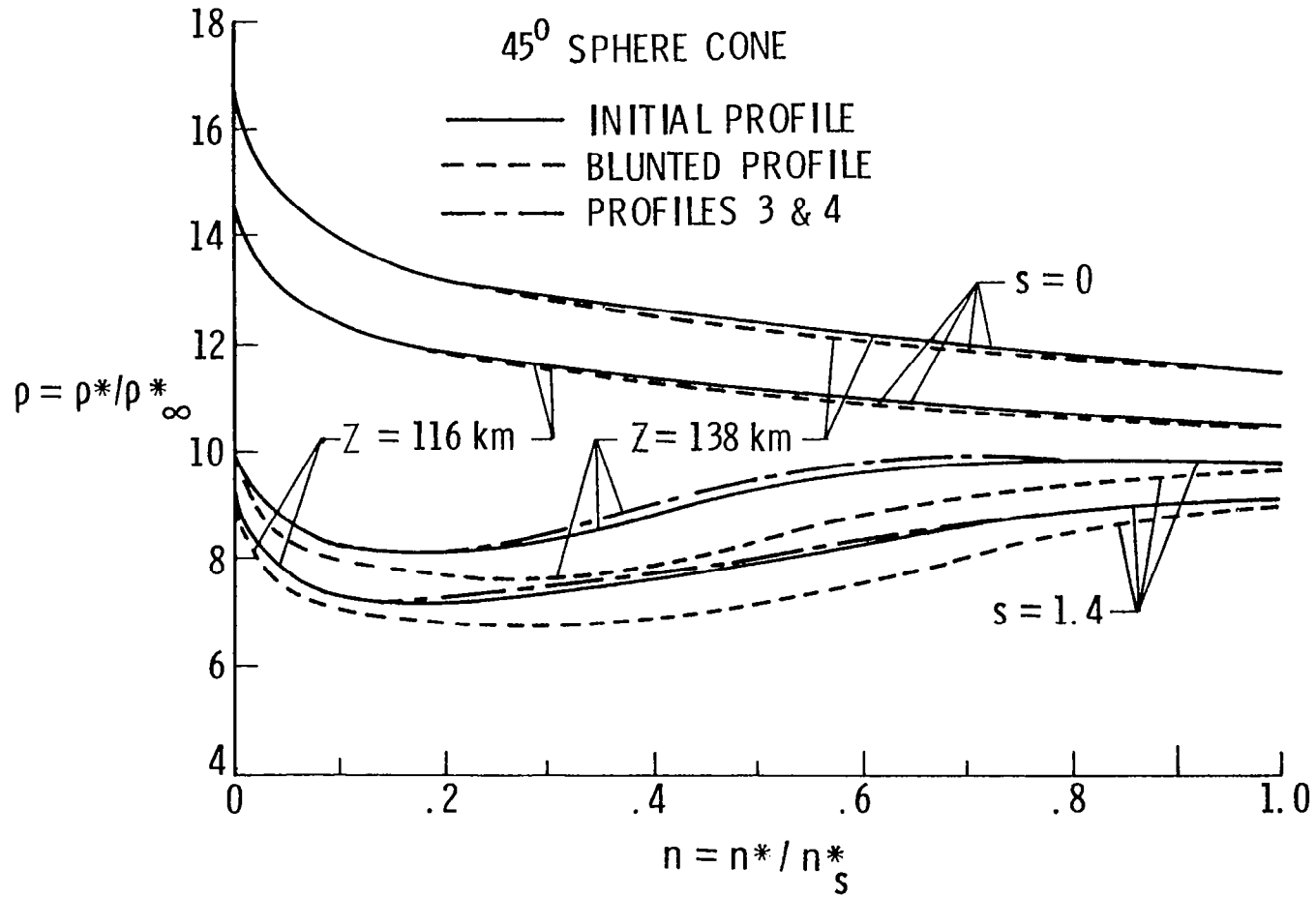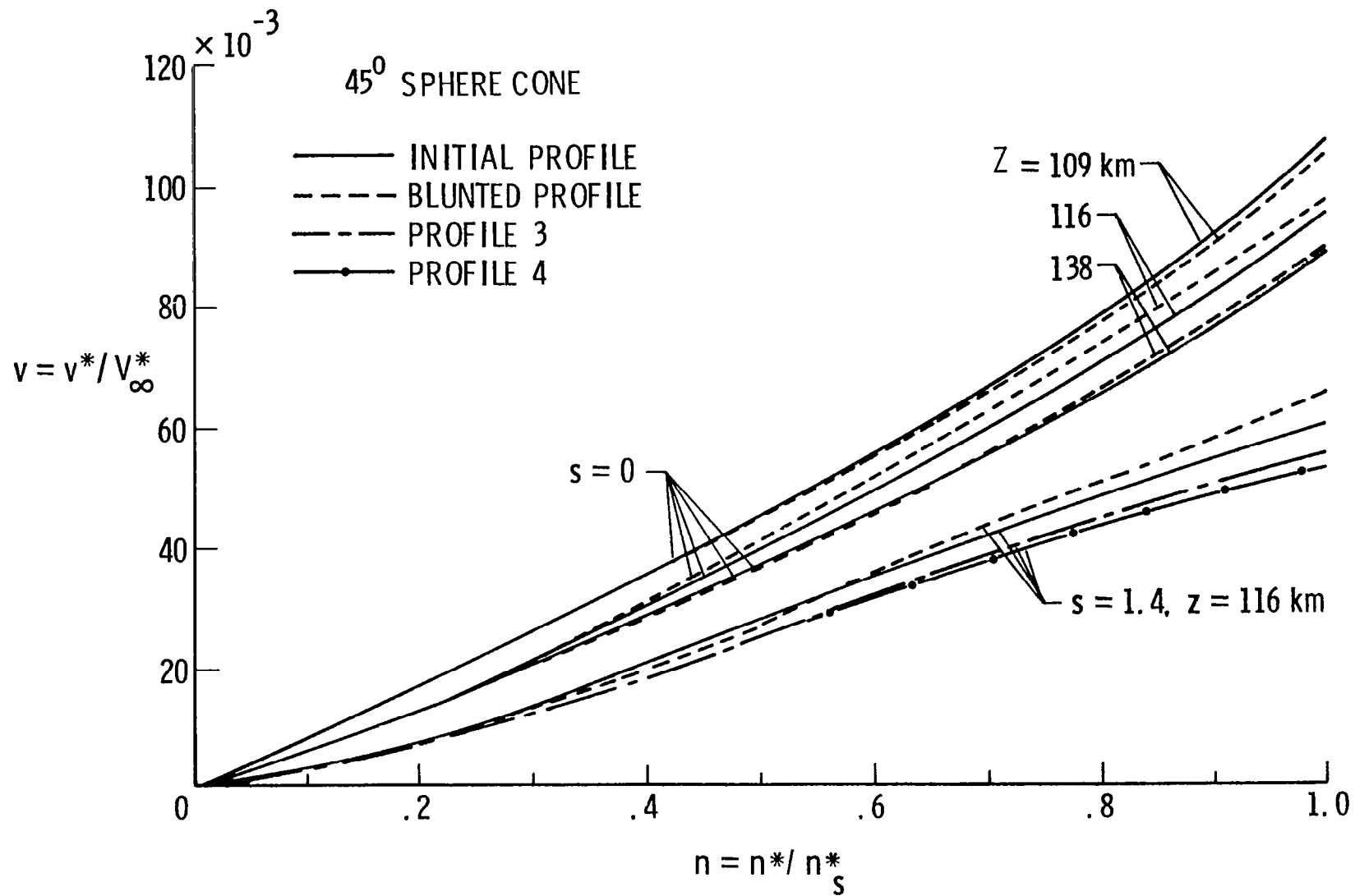
Figure 43. Variation of density in the shock layer for 2 body locations, s = 0 and 1.4, 45-degree sphere cone.

(a) s = 1.4 and Z = 116 km.

Figure 44. Variation of v-velocity component in the shock layer along the stagnation streamline.
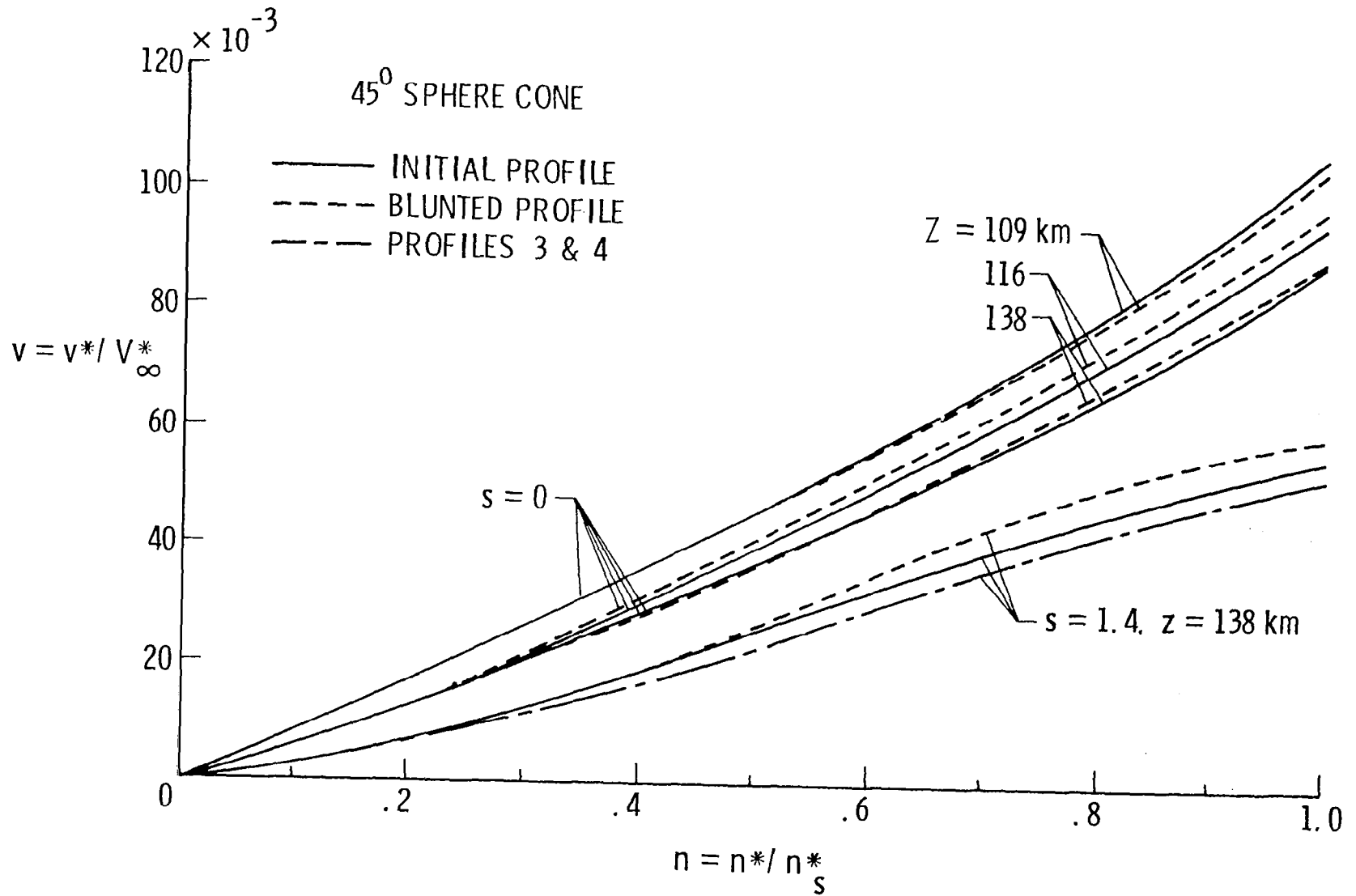
(b) s = 1.4 and Z = 138 km.

Figure 44. (Concluded).

appreciably. Figures 44(a) and (b) show that shape change does not influence the radial component of velocity significantly along the stagnation streamline; however, blunting is seen to influence the velocity toward downstream locations.

In the shock layer, variation in pressure is relatively small as compared to variations in temperature and density. The variation of pressure along the wall is shown in figure 45 for the four profiles and three entry conditions. As would be expected, pressure distribution is relatively higher for lower altitudes, and the maximum pressure occurs at the stagnation point. Results of profiles with uniform mass loss are not significantly different from the results of the initial profile. Blunting of the entry body is seen to increase the wall pressure significantly, the increase being maximum closer to the tangency point. Blunting does not seem to affect the stagnation region and downstream pressure distribution appreciably. However, it is possible for the blunted probe to experience relatively higher total drag.

The radiative heating results are illustrated in figures 46(a) and (b). In each case, the heating rate is seen to be significantly higher for the blunted profile all along the body. This, however, is expected because the shock temperature and shock-standoff distance are relatively higher for the blunted profile (see figs. 40 and 41). The maximum stagnation point heating occurs, of course, at $Z = 116$ km. For this case, the blunted profile heating rate is about nine percent higher than the initial profile heating. Figure 46(a) shows that heating rates for profiles 3 and 4 are lower than those of the initial profile. A difference of 4.9 percent between initial profile and profile 3, and of 5.3 percent between initial profile and profile 4, is noticed at the stagnation point. Results presented in figure 46(b) indicate that the stagnation-region heating is comparatively higher for $Z = 109$ km than for $Z = 138$ km. The difference between stagnation-point heating rates for the blunted and initial profiles is 10 percent for $Z = 109$ km and 6 percent for $Z = 138$ km. The
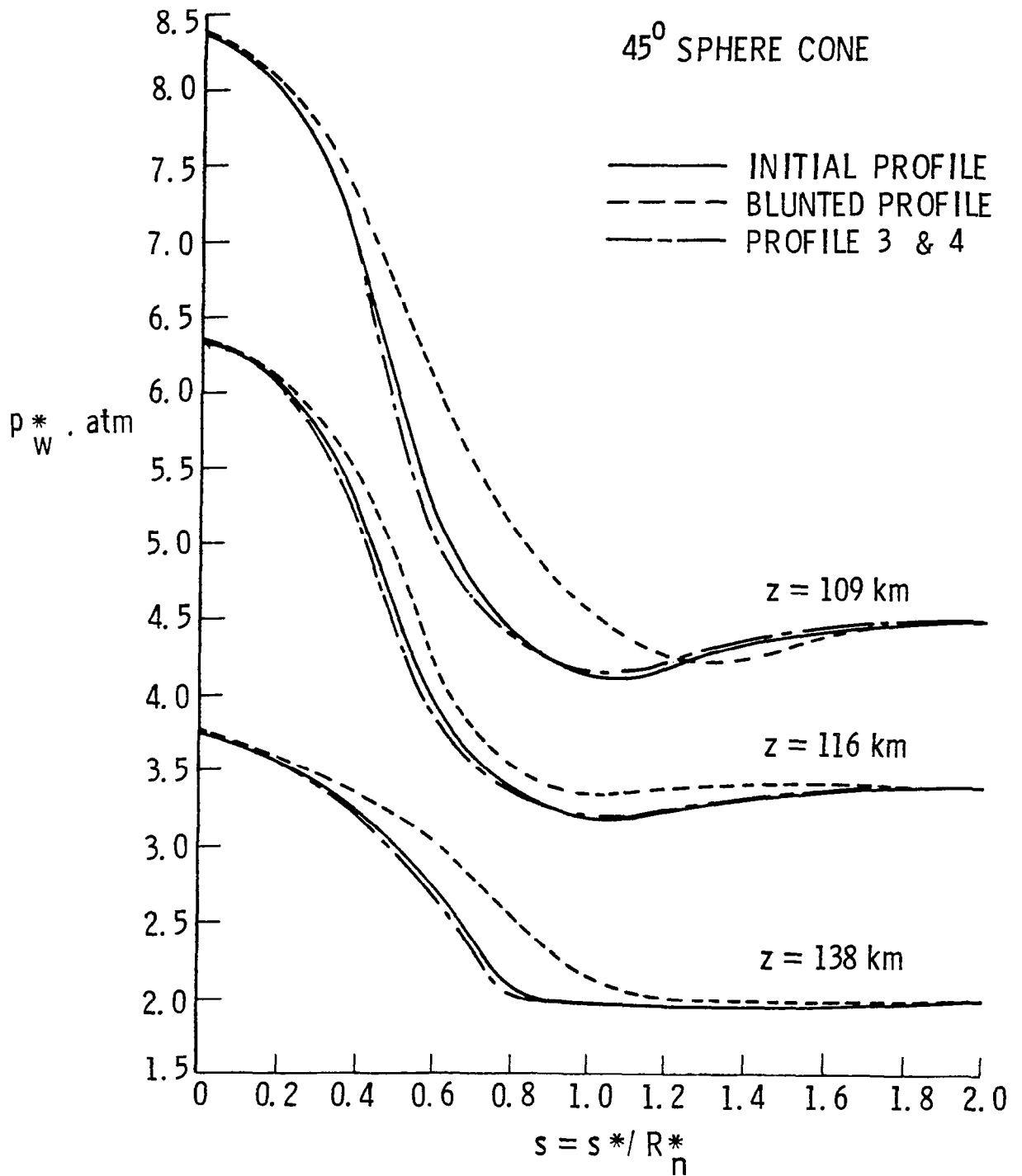
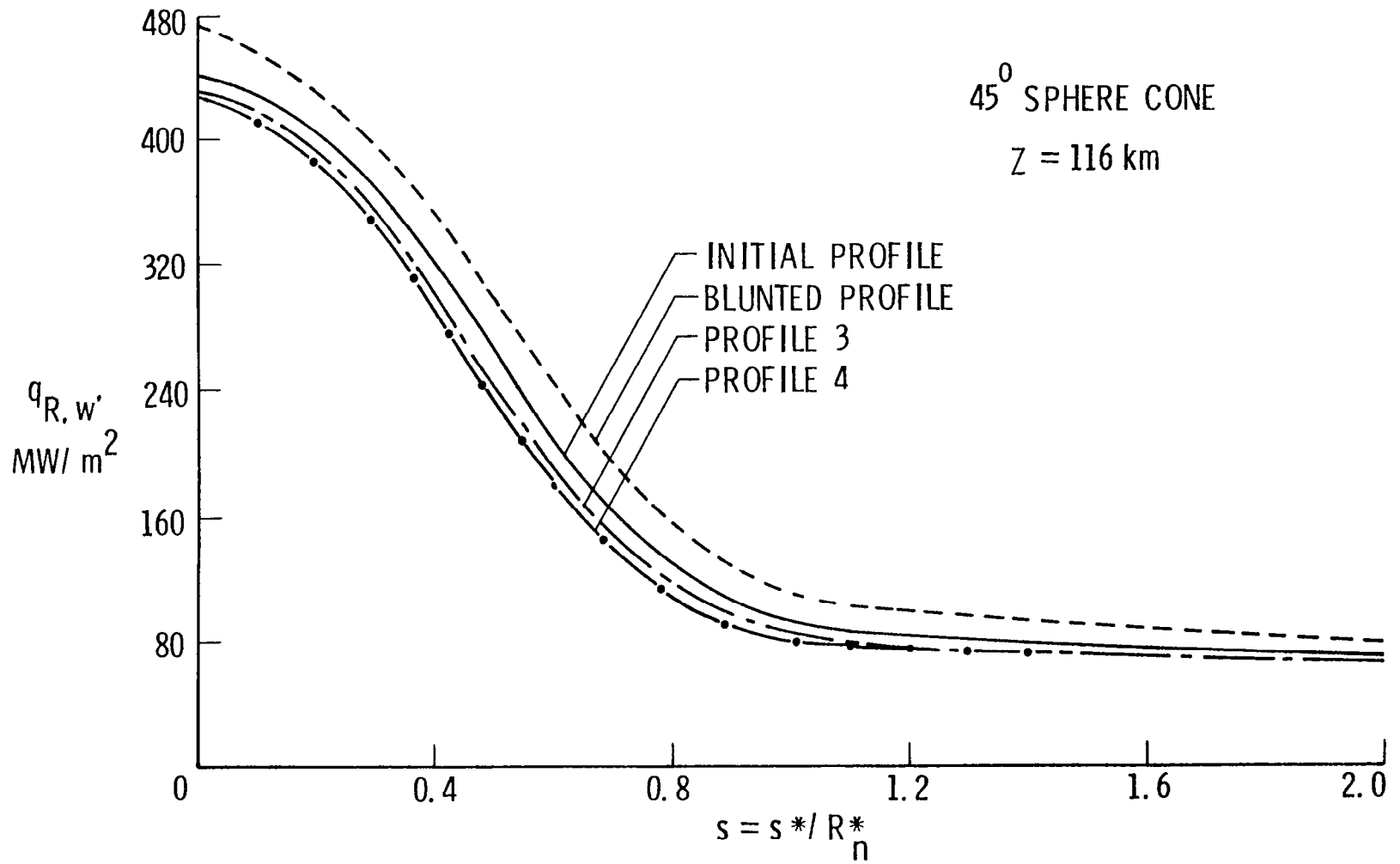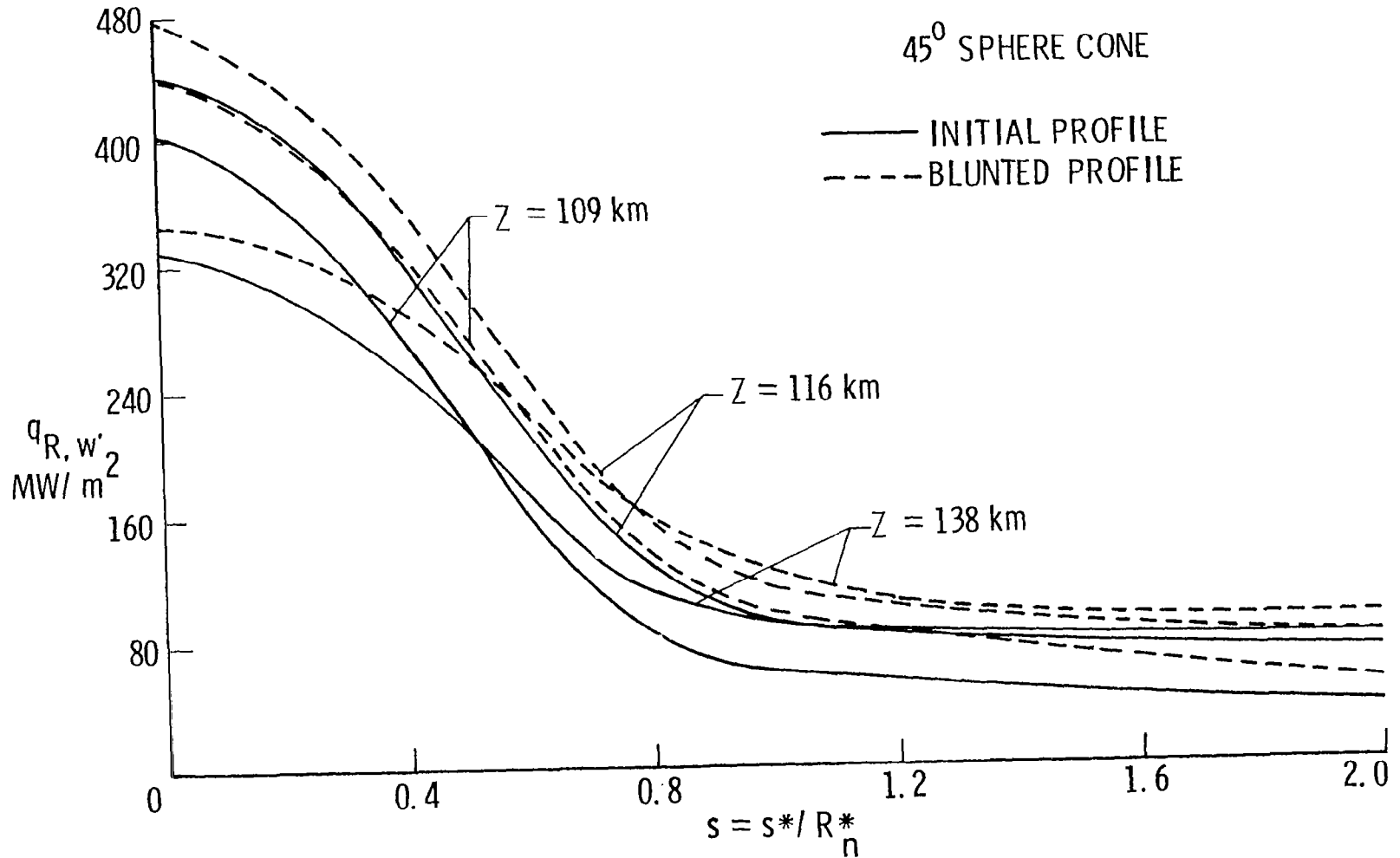Figure 45.   Surface pressure variation for 45-degree sphere cone.

(a) Z = 116 km.

Figure 46.   Radiative heating rates for 45-degree sphere cone.

(b) Z = 109, 116, and 138 km.

Figure 46. (Concluded).

results clearly indicate that the shape change can have significant influence on heating of the afterbody of the entry probe.

Results for 35-degree hyperboloid. - Some important results obtained for the 35-degree hyperboloid profiles [see fig. 38(b)] are presented in figures 47 to 53. As expected, the hyperboloid results show a smoother trend than the sphere cone results. The shock-standoff variation with distance along the body surface is illustrated in figure 47 for the three entry conditions considered. The results indicate that shape change increases the shock-standoff distance all along the body. The increase is greater for the blunted profile, and a maximum increase of 8.5 percent is noted for Z = 109 km at s = 0. The results of profile 3 show an increase of only about 3 percent for Z = 109 km at s = 0. Variation of the shock temperature is illustrated in figure 48. The results show that the shape change has only a slight influence on the temperature between locations s = 0.2 and 1.2, and its effects are negligible further downstream. Variation in the shock density for the initial and blunted profiles is shown in figure 49 for entry conditions at Z = 116 km and 138 km. The results indicate the shape change has only a slight influence on the density variation.

The changes in velocity, density, temperature, and pressure across the shock layer of a hyperboloid essentially follow the same general pattern as for the sphere cone, but the effects of shape change are not as pronounced. Variations in density and v-velocity across the shock layer are shown in figures 50 and 51, respectively. Figure 50 shows the density variation for two body locations (s = 0 and 1.5) and entry conditions (Z = 116 and 138 km). It is seen that along the stagnation line the density is not influenced by the shape change. However, small differences in results of the initial and blunted profiles are noted for the downstream location of s = 1.5. Uniform profile changes alter the density only slightly in the regions closer to the body. Figure 51 shows that along the stagnation streamline the shape change does not have any influence on the radial component of velocity: only slight changes are noted for Z = 138 km and s = 1.5.
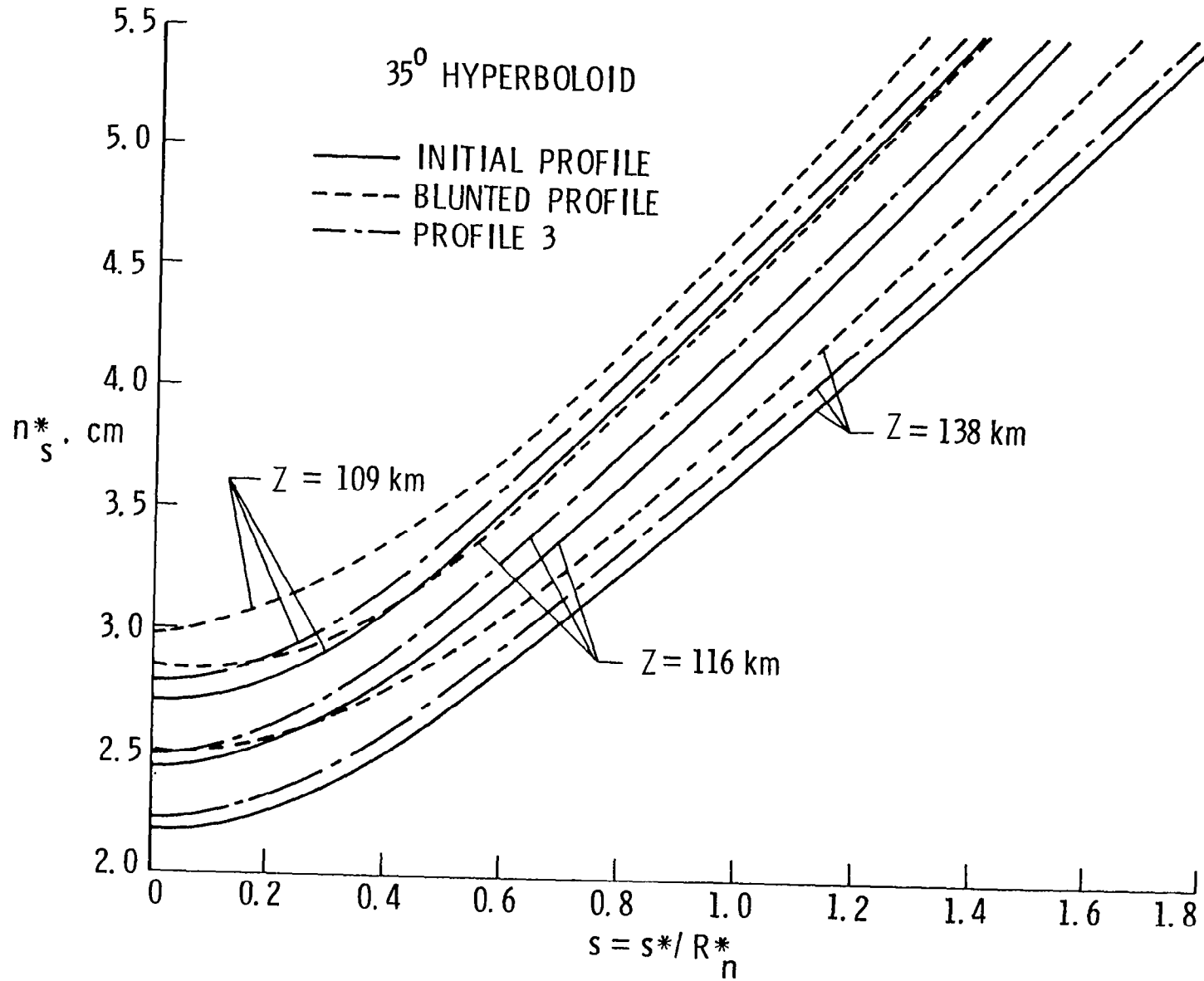
Figure 47. Shock-standoff variation for 35-degree hyperboloid.
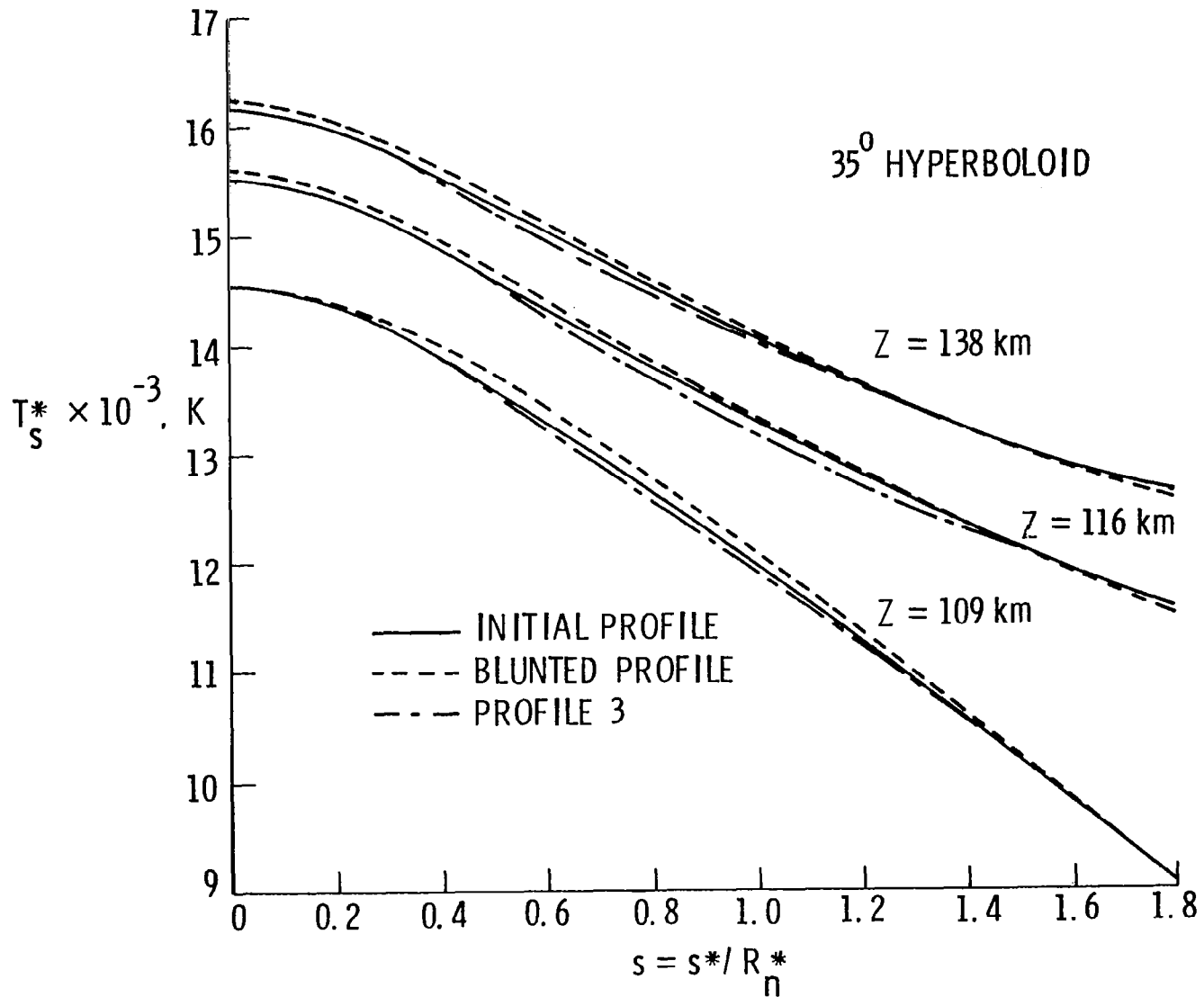
Figure 48. Variation of temperature just behind the shock for 35-degree hyperboloid.
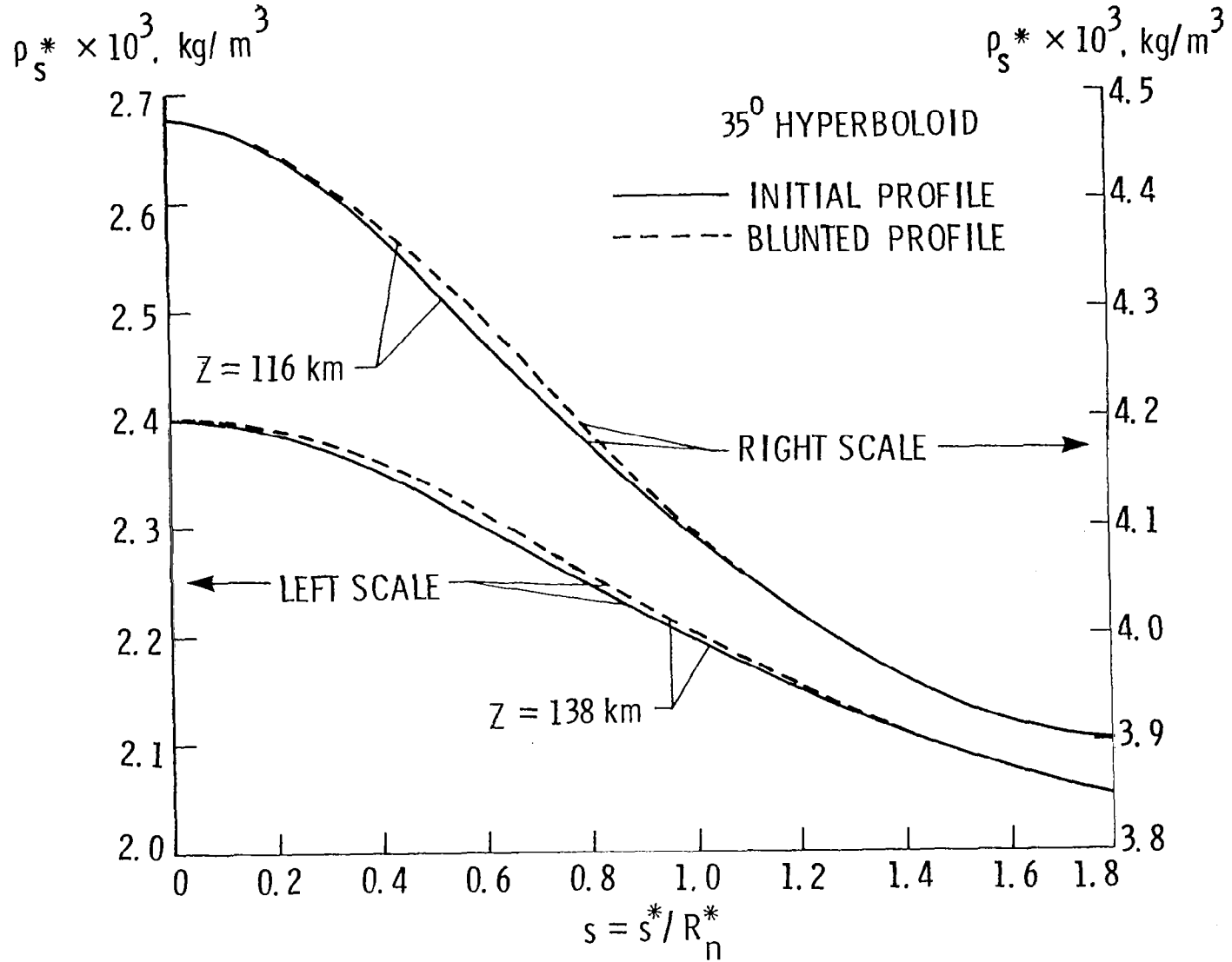
Figure 49. Variation of density just behind the shock for 35-degree hyperboloid.

Figure 50. Variation of density in the shock layer for body locations s = 0 and 1.5, 35-degree hyperboloid.

Figure 51. Variation of v-velocity component in the shock layer for 2 body locations, s = 0 and 1.5, 35-degree hyperboloid.

Figure 52. Surface pressure variation for 35-degree hyperboloid.

Figure 53. Radiative heating rates for 35-degree hyperboloid.

The pressure distribution along the wall is illustrated in figure 52 for the three entry conditions. The results indicate that blunting of the body slightly increases the wall press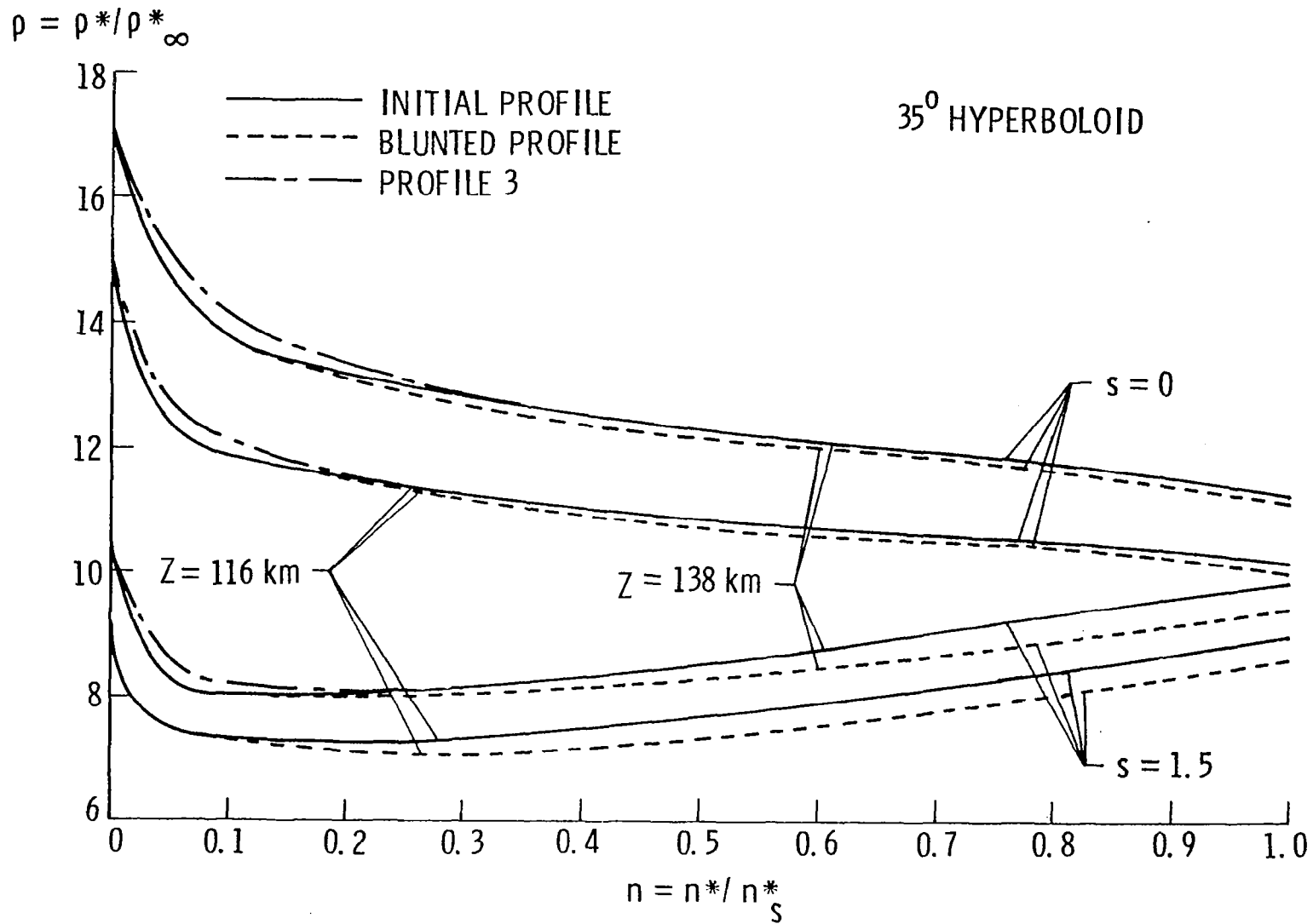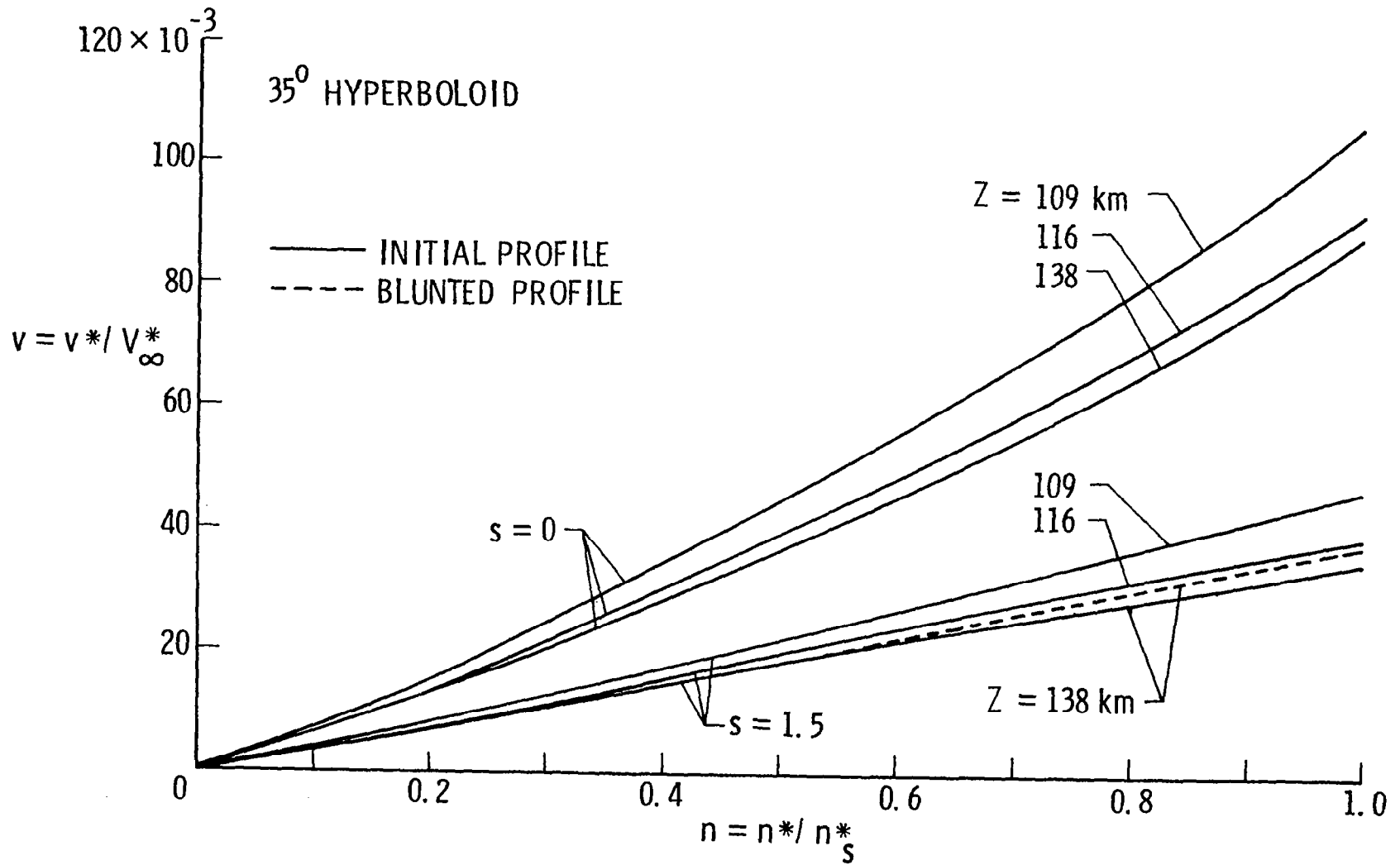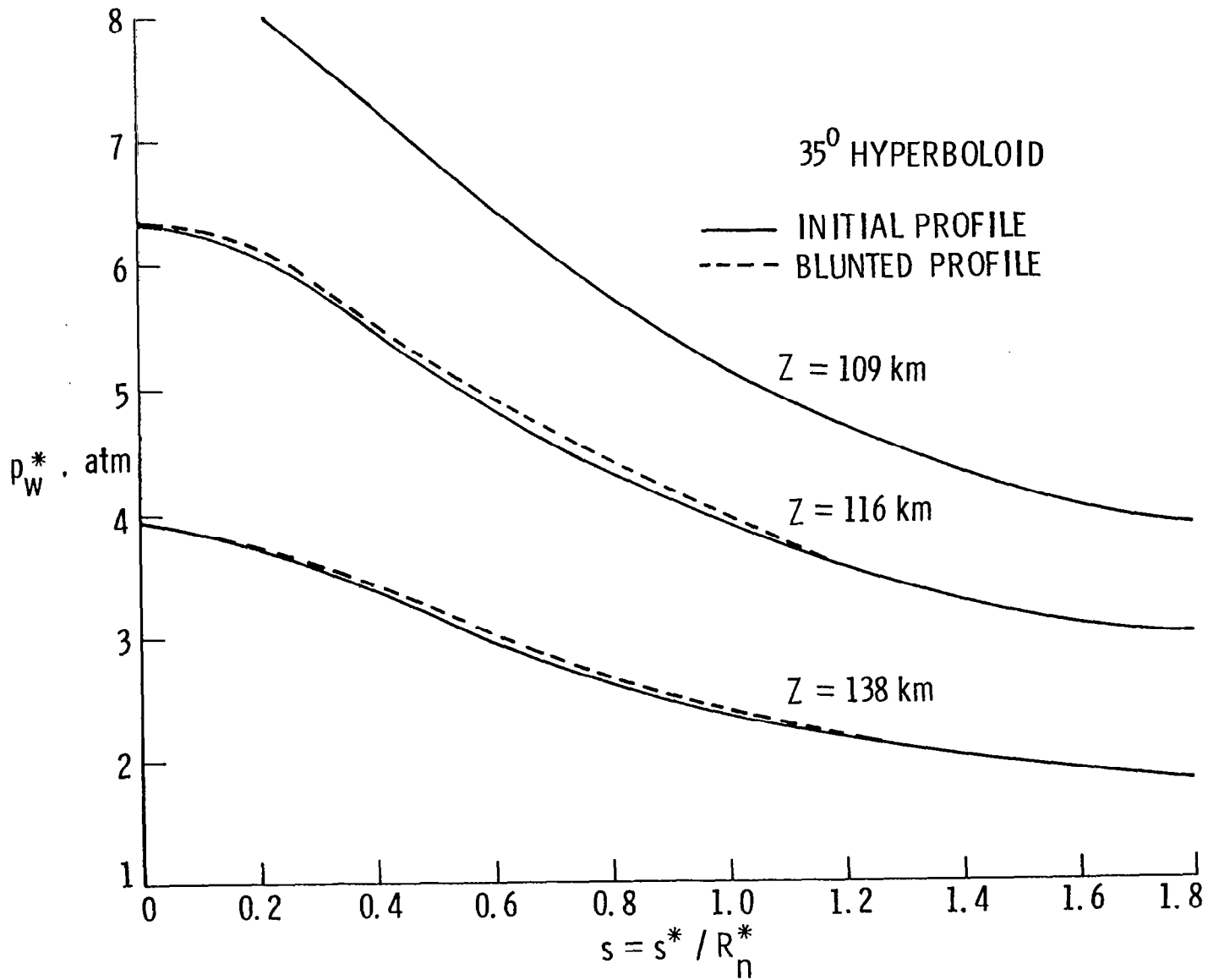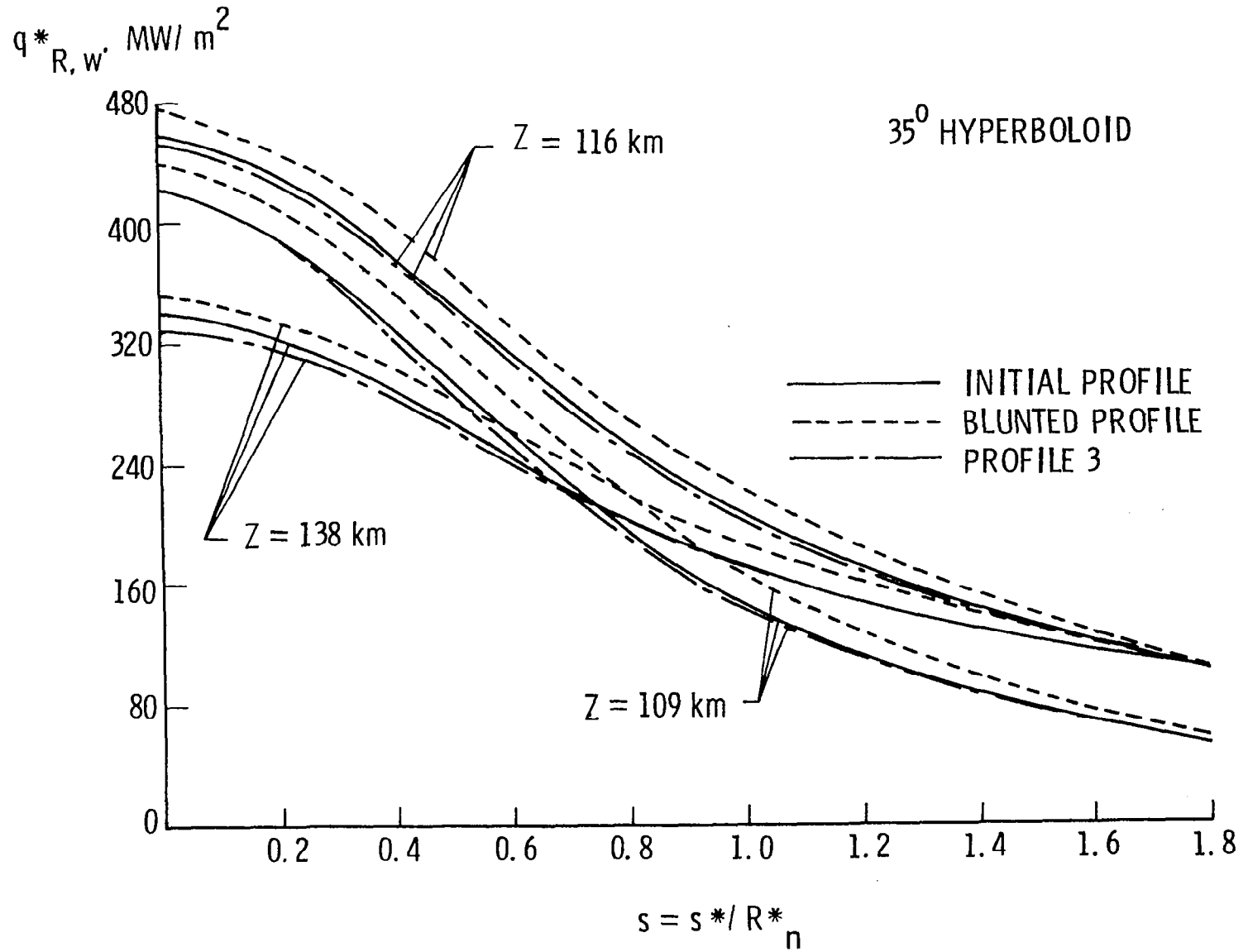ure for conditions of $Z = 116$ and 138 km. Results of the initial profile and the profile with uniform mass loss were so close that the difference could not be shown in figure 52.

The results of radiative heating are presented in figure 53. These results follow the general trend of the sphere cone results. The differences in stagnation-point heating rates for the initial and blunted profiles are found to be 4.9, 4.1, and 3.2 percent for $Z = 109$, 116, and 138 km, respectively. Results of the profile with uniform mass loss are not seen to be significantly different from the results of the initial profile.

Comparison of peak heating results. - Peak heating results for the 45-degree sphere cone, 35-degree hyperboloid, and 45-degree ellipsoid are compared in figures 54 to 58. Results for the 45-degree ellipsoid are seen to follow the same general trend as results for the 45-degree sphere cone; and, in comparison, results for the 35-degree hyperboloid are seen to exhibit a relatively smoother trend. In the stagnation region, all results for the ellipsoid are seen to be higher than results of the other two-body shapes.

Variations in the shock-standoff distance, illustrated in figure 54, indicate that the standoff distances for the ellipsoid are much greater than for the sphere cone, and, for the most part, the hyperboloid results fall between these two results. For the ellipsoid, the effect of blunting is seen to be quite pronounced in the stagnation region. As such, one would expect a higher stagnation-region heating rate for the ellipsoid.

The shock-temperature variations, illustrated in figure 55, indicate that the temperatures are higher for the ellipsoid near the stagnation region, but they fall between the results of the hyperboloid and sphere cone between $s = 0.6$ and 1.2. After location $s = 1.2$, the results are slightly lower than the results of the sphere cone.
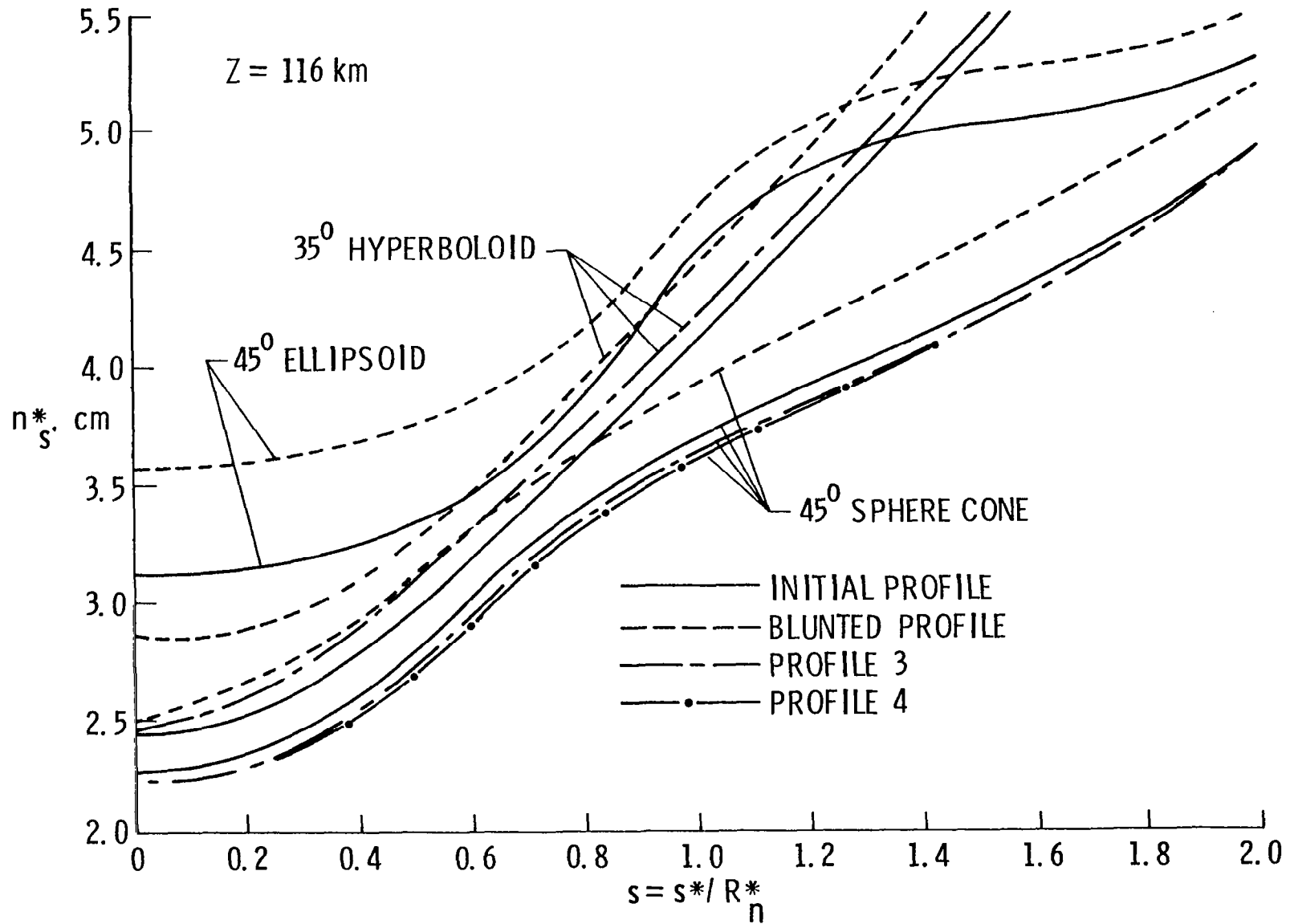
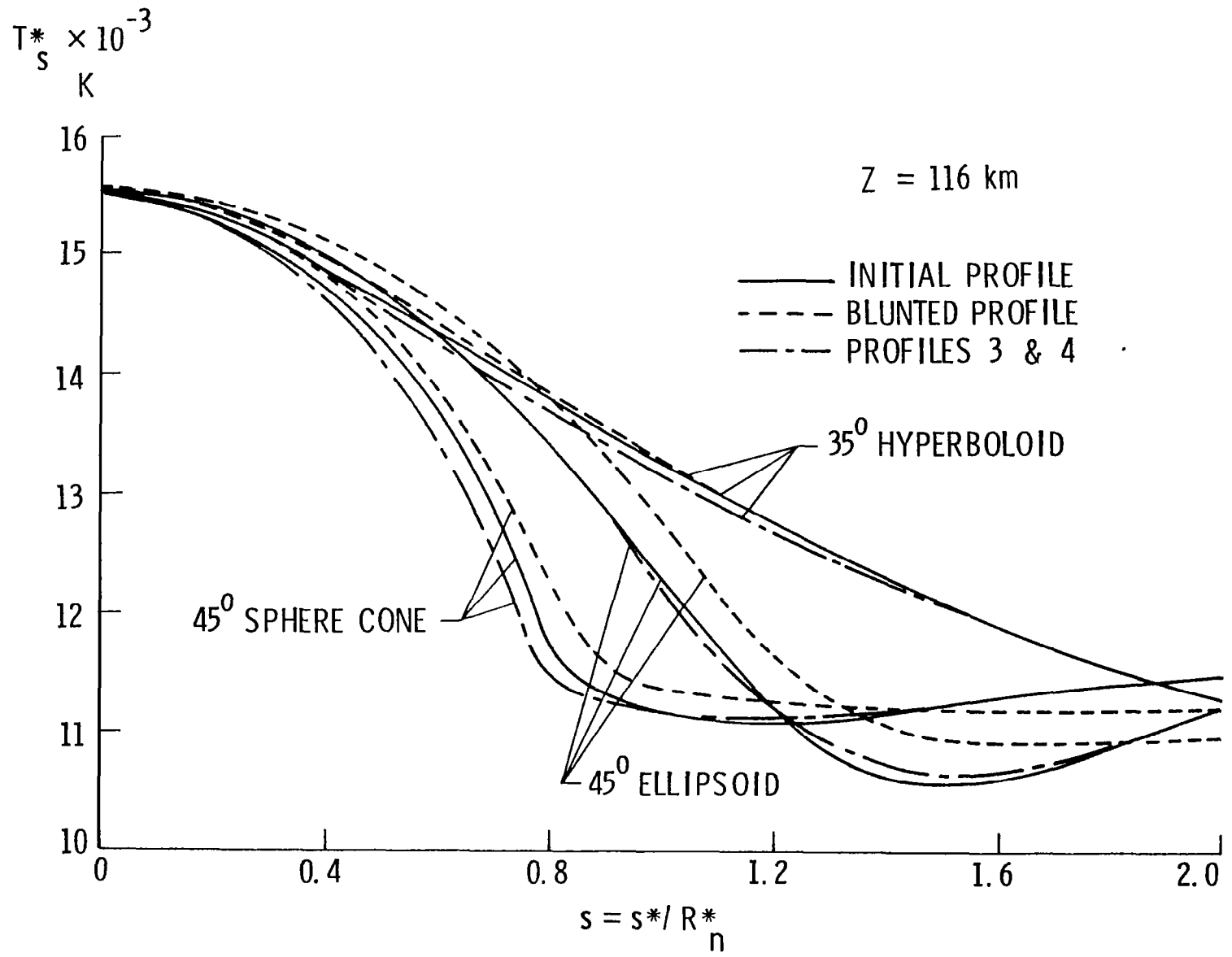Figure 54.   Comparison of shock-standoff distance for Z = 116 km.

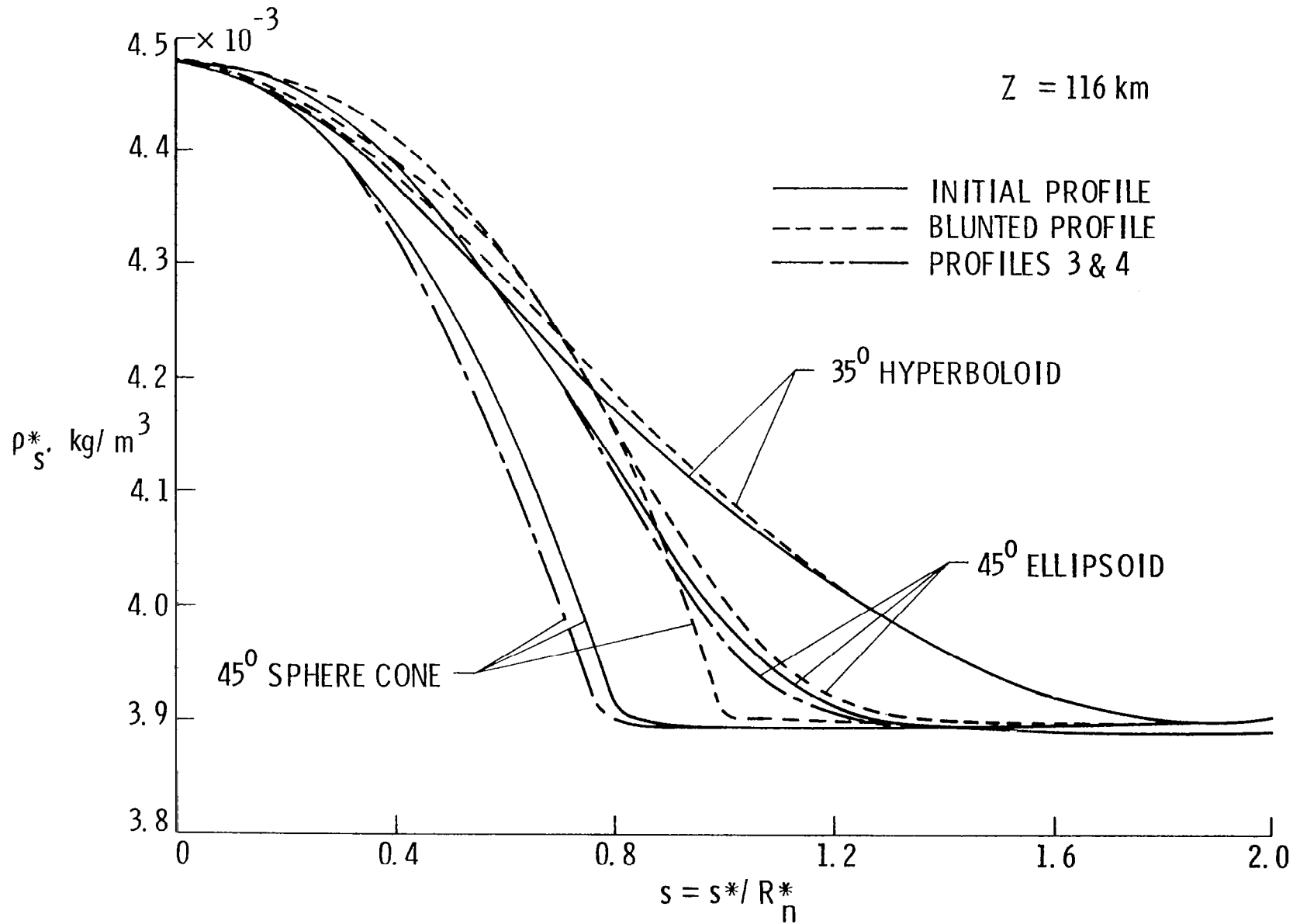Figure 55. Comparison of shock temperature for Z = 116 km.

Figure 56. Comparison of shock density for Z = 116 km.

In general, the shape change is seen to have greater effect on the temperature distribution for the ellipsoid than for the sphere cone. Variations in the shock density (fig. 56) follow essentially the same trend as the temperature variations. The effects of shape change for the ellipsoid, however, are not as pronounced as for the sphere cone. For the ellipsoid, blunting results in a maximum increase in density of 1.2 percent at s = 0.8. The results of uniform mass loss, however, do not show any significant change.

The pressure distribution along the body surface is illustrated in figure 57. The results show that the shape change has a considerable effect on the pressure variations for the ellipsoid in the range from s = 0.6 to 1.2. The total drag for the ellipsoid, however, may not be greater than that for the sphere cone. As noted earlier, the shape change does not have significant influence on the pressure distribution for the hyperboloid, but the total drag for this shape can be higher than that for the other two shapes.

The radiative heating rates for the three entry shapes are compared in figure 58. As expected, the radiative heating rates for the ellipsoid are comparatively higher in the stagnation region. In the downstream region, however, the results fall between the results of the hyperboloid and sphere cone. For the ellipsoid, blunting results in a maximum increase in heating of 7 percent at s = 0.8. In general, the increase in heating rates due to shape change is seen to be greater for the sphere cone and ellipsoid than for the hyperboloid. Also, the shape change is seen to have considerably more effect on heating of the afterbody for the sphere cone and ellipsoid than for the hyperboloid. The results further indicate that the total radiative heating load (i.e., the total radiative heat input) to the entry body will be comparatively higher for the ellipsoid, and this will be followed by the results for the hyperboloid and sphere cone, respectively.

The results presented here indicate that uniform mass loss resulting in a shape that corresponds closely to the initial profile does not affect the shock-standoff distance, temperature, density,
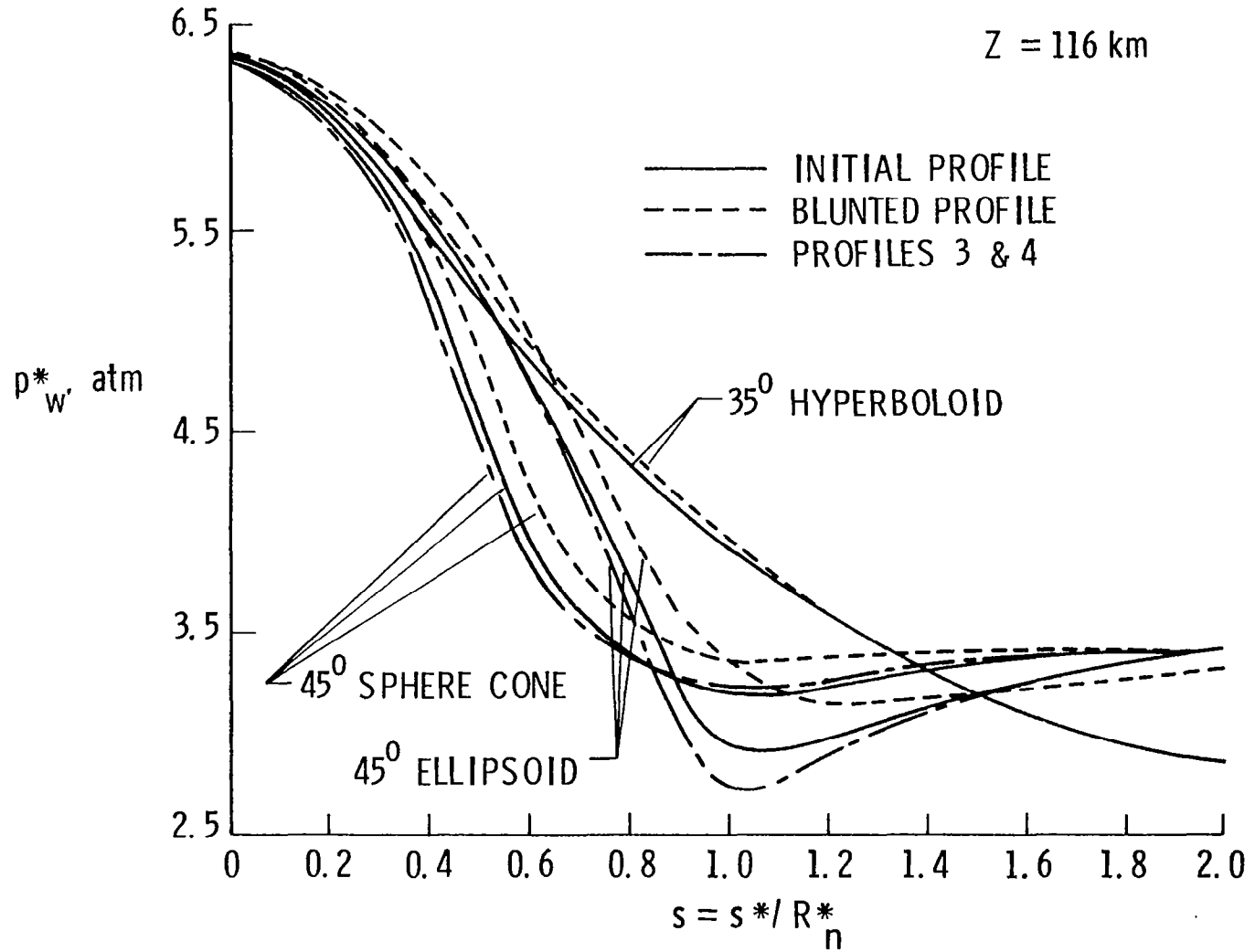
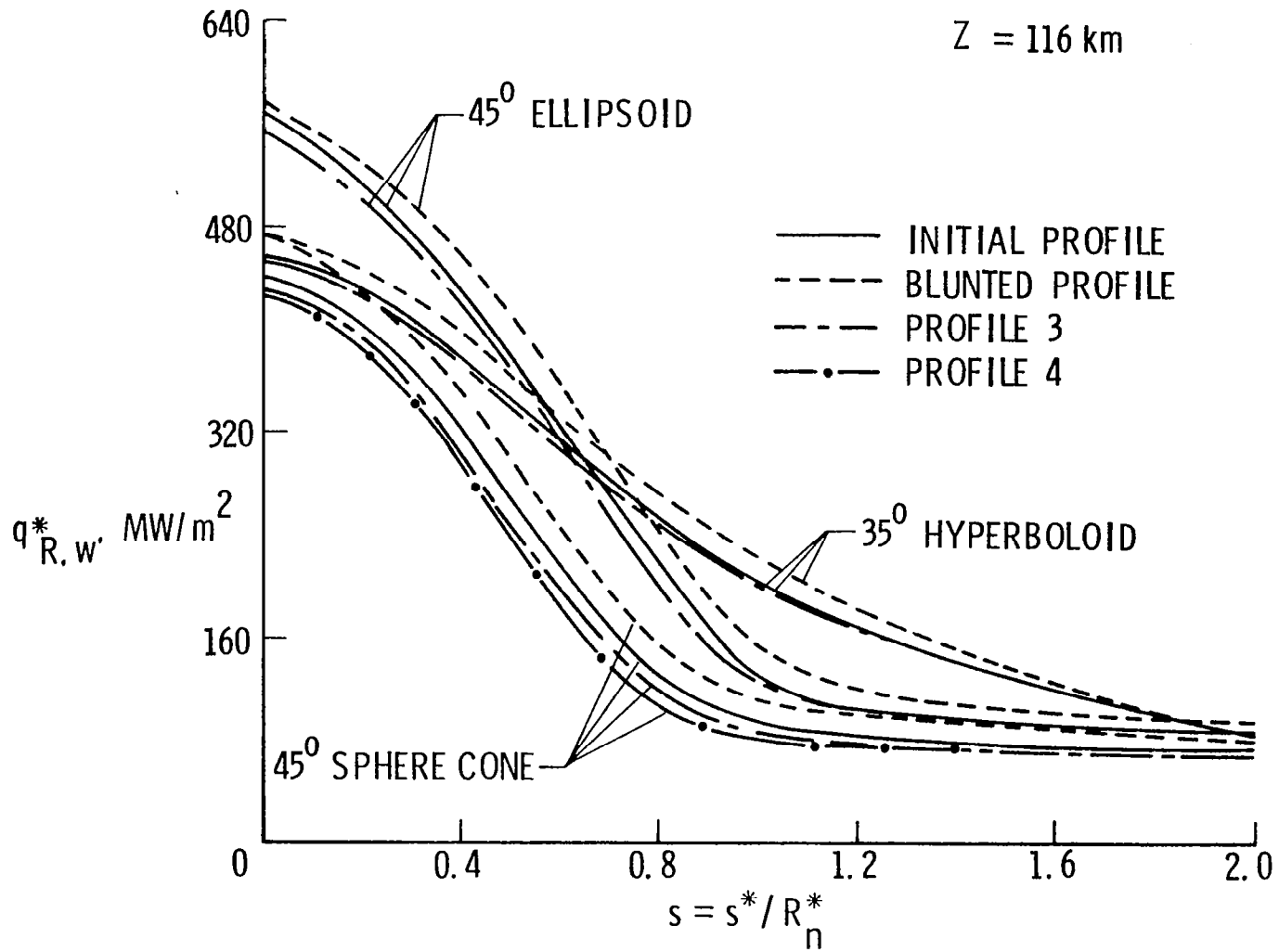Figure 57. Comparison of surface pressure for Z = 116 km.

Figure 58. Comparison of radiative heating rates for Z = 116 km.

and pressure distribution along the body appreciably. In such cases, radiative heating rates to the body are not different significantly from the heating rates to the body with initial configurations. Blunting of the nose region, however, is seen to have a significant influence on the entire flow phenomena in the stagnation and downstream regions. It is noted that the shock-standoff distance increases with increasing nose blunting. While nose blunting results in increasing the shock temperature all along the body, its influence on increasing the density is significant only in the stagnation region. In the downstream regions, the velocity, density, temperature, and pressure are altered significantly across the shock layer because of changes in the probe configurations. In most cases, considerable increase in radiative heating rates is noted in the stagnation as well as downstream regions due to severe nose blunting. Blunting of the entry body is seen to increase the wall pressure distribution significantly. But, its effect on stagnation-region and afterbody pressure distribution is relatively small. However, it is possible for the blunted sphere cone and ellipsoid to experience relatively higher total drag. Blunting is seen to increase the radiative heating rates all along the body for all configurations considered. But, in the stagnation region, the increase is relatively higher for the ellipsoid and sphere cone than for the hyperboloid. The shape change is seen to have considerably more effect on heating of the afterbody for the sphere cone and ellipsoid than for the hyperboloid. It is further noted that the total radiative heating load to the body will be comparatively higher for the ellipsoid followed by that for the hyperboloid and sphere cone.

148

CONCLUSIONS

Results were obtained to investigate the influence of simplified radiation models, nonequilibrium radiative energy transfer, and probe condiguration changes on the flow properties and the heating rates in the stagnation and downstream regions of a Jovian entry body. Results obtained by using a simple, 30-step, radiation absorption model are in good agreement with results of other sophisticated models available in the literature. It is found that use of the present model reduces the computational time significantly. However, use of this simplified model is recommended only for general parametric studies.

The radiative transfer equation has been formulated under the nonlocal thermodynamic equilibrium (NLTE) conditions. The NLTE effects are seen to enter through the absorption coefficient and the source function. The NLTE source function is expressed in terms of the Planck function, an NLTE parameter that measures the relative importance of the collisional and radiative deactivation processes in the gas and the influence factors arising from the higher level energy transitions. The influence of NLTE on the entire shock-layer flow phenomena is investigated by neglecting the contributions of ablative products as well as by including them.

The results obtained in the absence of the ablative species in the shock layer indicate that the NLTE effects are greater closer to the body than near the shock. The influence of NLTE, in general, is to reduce the convective and radiative heating to the entry body, and a significant reduction in radiative heating is noted. The NLTE effects are greater for higher entry conditions. The NLTE results, however, are not influenced by the change in the forebody configurations.

The viscous shock-layer equations with coupled ablation and mass injection (for the entry probe with carbon phenolic heat shield) are solved under the NLTE conditions. The Swan (0,0), Freymark (0,1), and Mulliken (0,0) bands of the C_2 band systems are treated to be in nonequilibrium in the ablation layer. Flow-field results obtained

for the peak-heating conditions (t = 111.3 sec) indicate that the temperature distribution in the shock layer is lower under NLTE conditions. tions. Similar behavior is also noticed for the enthalpy distribution. It is found that NLTE increases the density in the shock layer, but has no influence on the pressure variation. The radiative heating to the entry body is increased significantly because of NLTE; this, in turn, results in increased mass loss from the body.

For investigating the influence of shape change of the entry probe on the flow field, different initial configurations (45-degree sphere cone, 35-degree hyperboloid, and 45-degree ellipsoid) for the entry probe were considered, and results were obtained for three different entry conditions (Z = 109. 116, and 138 km). The results indicate that uniform mass loss resulting in a shape that corresponds closely to the initial profile does not affect the shock-standoff distance, temperature, density, and pressure distribution along the body appreciably. Blunting of the nose, however, is seen to have a significant influence on the entire flow phenomena in the stagnation and downstream regions. Considerable increase in radiative heating rates is noted in the stagnation as well as downstream regions for all configurations considered. In the stagnation region, however, the increase is relatively higher for the ellipsoid and sphere cone than for the hyperboloid. It is concluded that, due to the shape change, the total heating load to the body will be higher for the ellipsoid than the hyperboloid and sphere cone.

APPENDIX

FINITE-DIFFERENCE SCHEME FOR VISCOUS
RADIATING SHOCK-LAYER FLOW

The solution of the second-order partial differential equation expressed by equation (113) is obtained by employing the implicit finite-difference scheme. For this purpose, the shock layer is considered as a network of nodal points with a variable grid space in the η-direction. The scheme is shown in figure A.1, where m is a station measured along the body surface and n denotes the station normal to the body surface. The derivatives are converted to finite-difference form by using Taylor's series expansions. Thus, unequal space central difference equations in the η-direction at point m, n can be written as

$$\left(\frac{w}{\partial \eta}\right)_n = \frac{\Delta\eta_{n-1}}{\Delta\eta_n \left(\Delta\eta_{n-1} + \Delta\eta_n\right)} \left(W_{m,n+1}\right) - \frac{\Delta\eta_n}{\Delta\eta_{n-1}\left(\Delta\eta_{n-1} + \Delta\eta_n\right)} \left(W_{m,n-1}\right)$$

$$+ \frac{\Delta\eta_n - \Delta\eta_{n-1}}{\Delta\eta_n \Delta\eta_{n-1}} \left(W_{m,n}\right) \tag{A.1a}$$

$$\left(\frac{\partial^2 W}{\partial \eta^2}\right)_n = \frac{2}{\Delta\eta_n \left(\Delta\eta_n + \Delta\eta_{n-1}\right)} \left(W_{m,n+1}\right) - \frac{2}{\Delta\eta_n \Delta\eta_{n-1}} \left(W_{m,n}\right)$$

$$+ \frac{2}{\Delta\eta_{n-1}\left(\Delta\eta_n + \Delta\eta_{n-1}\right)} \left(W_{m,n-1}\right) \tag{A.1b}$$

$$\left(\frac{\partial W}{\partial \xi}\right)_m = \frac{W_{m,n} - W_{m-1,n}}{\Delta\xi} \tag{A.1c}$$

A typical difference equation is obtained by substituting equations (A.1) in equation (113) as

$$W_{m,n} = -(D_n/B_n) - (A_n/B_n) W_{m,n+1} - (C_n/B_n) W_{m,n-1} \tag{A.2}$$
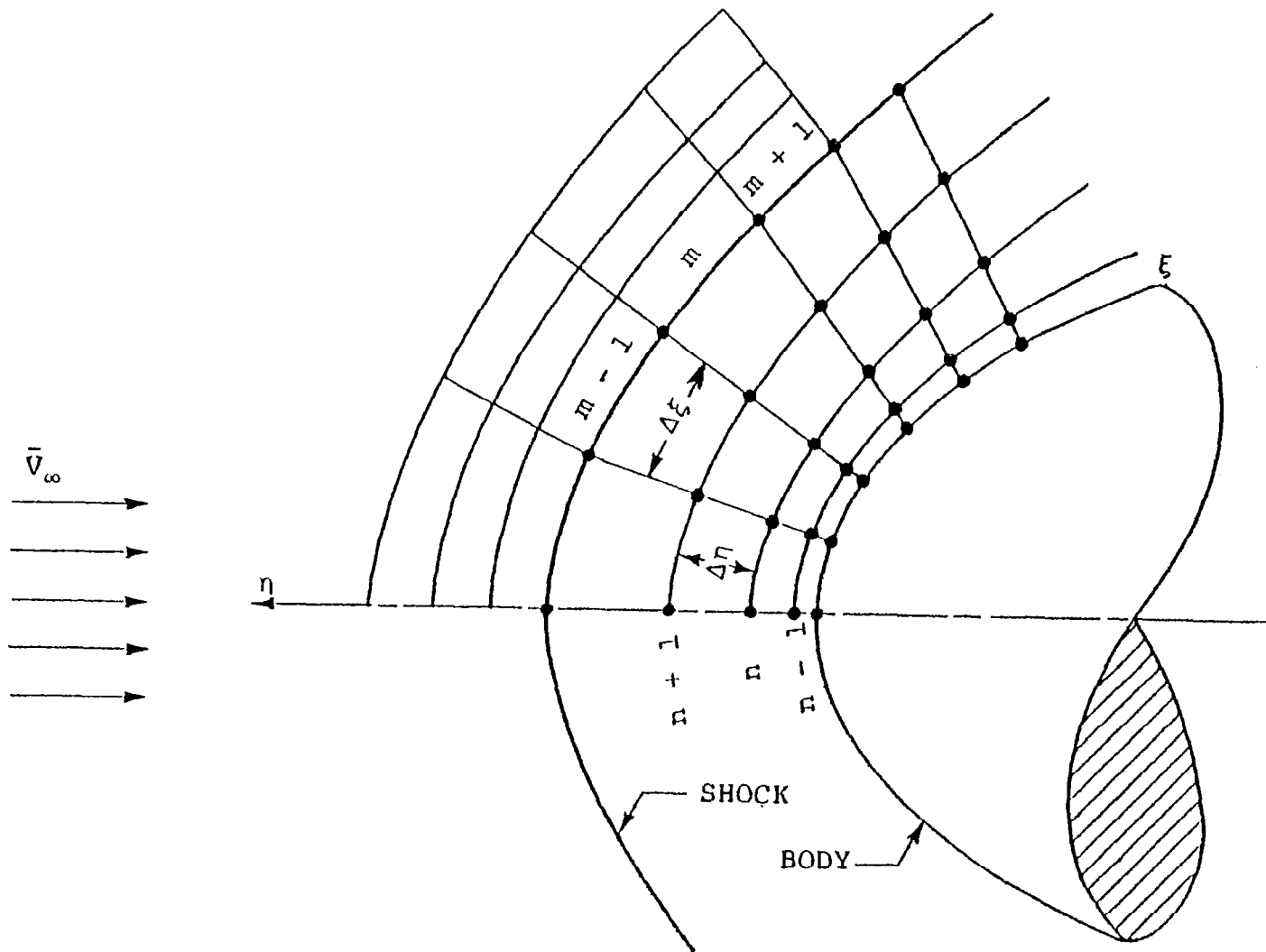
Figure A.1.   Finite-difference representation of flow field.

where

$$A_n = (2 + a_1\Delta\eta_{n-1})/[\Delta\eta_n(\Delta\eta_n + \Delta\eta_{n-1})]$$

$$B_n = -[2 - a_1(\Delta\eta_n - \Delta\eta_{n-1})]/[(\Delta\eta_n\Delta\eta_{n-1}) - a_2 - (a_4/\Delta\xi_{m-1})]$$

$$C_n = (2 - a_1\Delta\eta_n)/[\Delta\eta_{n-1}(\Delta\eta_n + \Delta\eta_{n-1})]$$

$$D_n = a_3 - a_4 W_{m-1,n}/\Delta\xi_{m-1}$$

Now, if it is assumed that

$$W_{m,n} = E_n W_{m,n+1} + F_n \tag{A.3}$$

or

$$W_{m,n-1} = E_{n-1} W_{m,n} + F_{n-1} \tag{A.4}$$

then by substituting equation (A.4) into equation (A.2) there is obtained

$$W_{m,n} = [-A_n/(B_n + C_n E_{n-1})](W_{m,n+1})$$

$$+ (-D_n - C_n F_{n-1})/(B_n + C_n E_{n-1}) \tag{A.5}$$

By comparing equations (A.3) and (A.5), one finds

$$E_n = -A_n/(B_n - C_n E_{n-1}) \tag{A.6}$$

$$F_n = (-D_n - C_n F_{n-1})/(B_n + C_n E_{n-1}) \tag{A.7}$$

Now, since E and F are known form the boundary conditions, E_n and F_n can be calculated from equations (A.6) and (A.7). The quantities $W_{m,n}$ at point m, n can now be calculated from equation (A.3).

153

The overall solution procedure starts with evaluation of the flow
properties immediately behind the shock by using the Rankine-Hugoniot
relations. With known shock and body surface conditions, each of the
second-order partial differential equations is integrated numerically
by using the tridiagonal formalism of equation (113) and following the
procedure described by equations (A.2) to (A.7). As mentioned before,
the solutions are obtained first for the stagnation streamline. With
this solution providing the initial conditions, the solution is marched
downstream to the desired body location. The first solution pass
provides only an approximate flow-field solution. This is because in
the first solution pass the thin shock-layer form of the normal momentum
equation is used, the stagnation streamline solution is assumed to be
independent of downstream influence, $dy_s/d\xi$ is equated to zero at each
body station, and the shock angle α is assumed to be the same as the
body angle θ. All these assumptions are removed by making additional
solution passes.

In the first solution pass, the viscous shock-layer equations are
solved at any location m after obtaining the shock conditions from the
free-stream conditions. The converged solutions at station (m-1) are
used as the initial guess for the solution at station m. The solution
is iterated locally until convergence is achieved. For the stagnation
streamline, guess values for dependent variables are used to start the
solution. In the first local iteration, $(\partial n_s/\partial \xi)$ and $(\partial W/\partial \xi)$ are assumed
to be zero. The energy equation is then integrated numerically to
obtain a new temperature. By using this temperature, new values of
thermodynamic and transport properties are calculated. Next, the x-
momentum equation is integrated to find the $\bar{u}$-component of velocity. The
continuity equation is used to obtain both the shock standoff distance
and the $\bar{v}$-component of velocity. The pressure $\bar{P}$ is determined by
integrating the normal momentum equation. Then the equation of state is
used to determine the density value.

With known stagnation streamline solution and body surface and
shock conditions, the above procedure is used to find solutions for any

body location m. The flow chart for the computational procedure is shown in figures A.2 and A.3. Further details of this procedure and flow chart are given in reference 35. The flow chart for the NLTE radiation computation is shown in figure A.4, and the integrals used in this chart are defined in figure A.5.
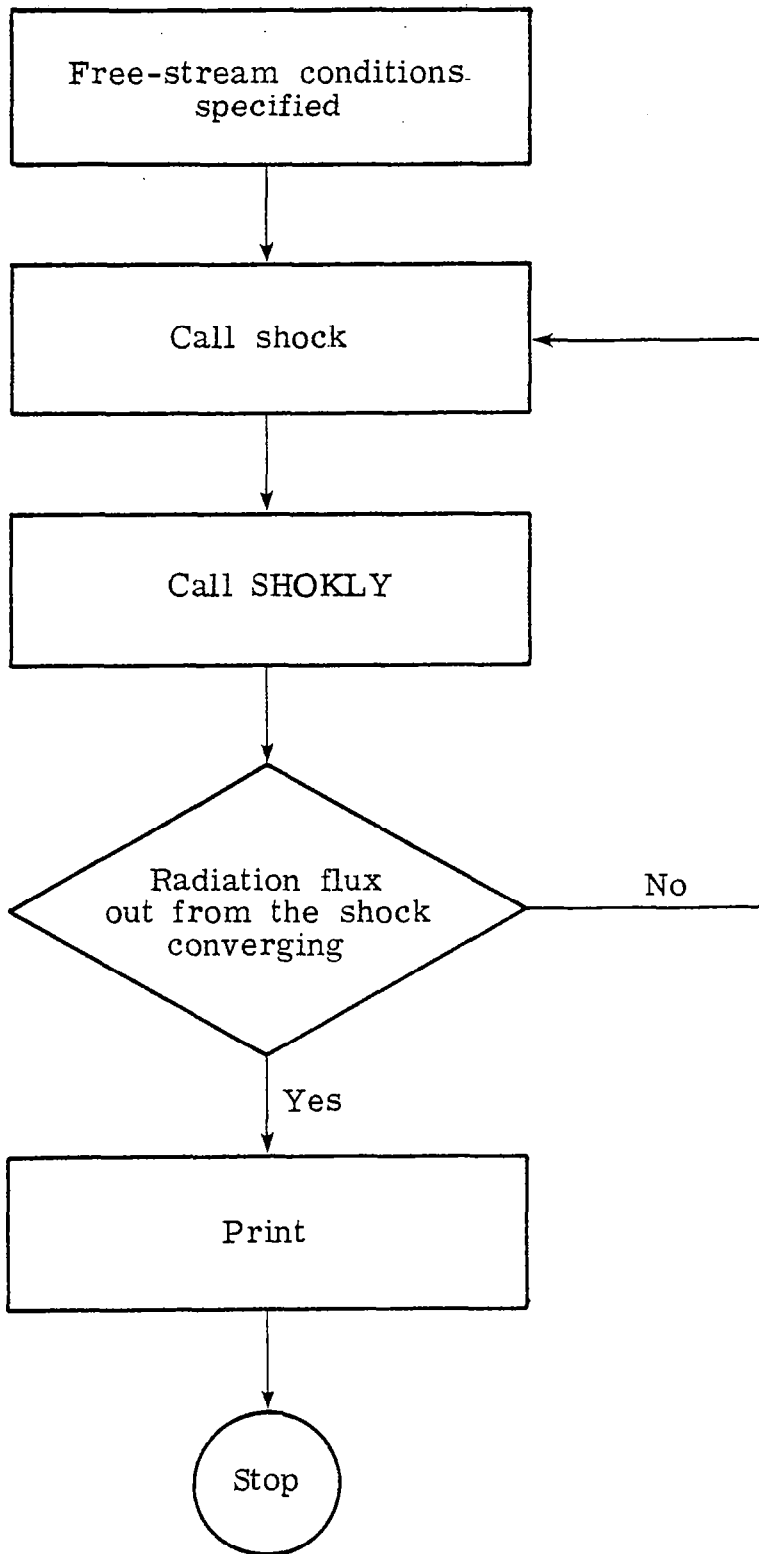
Figure A.2. Flow chart for shock-layer solution procedure.
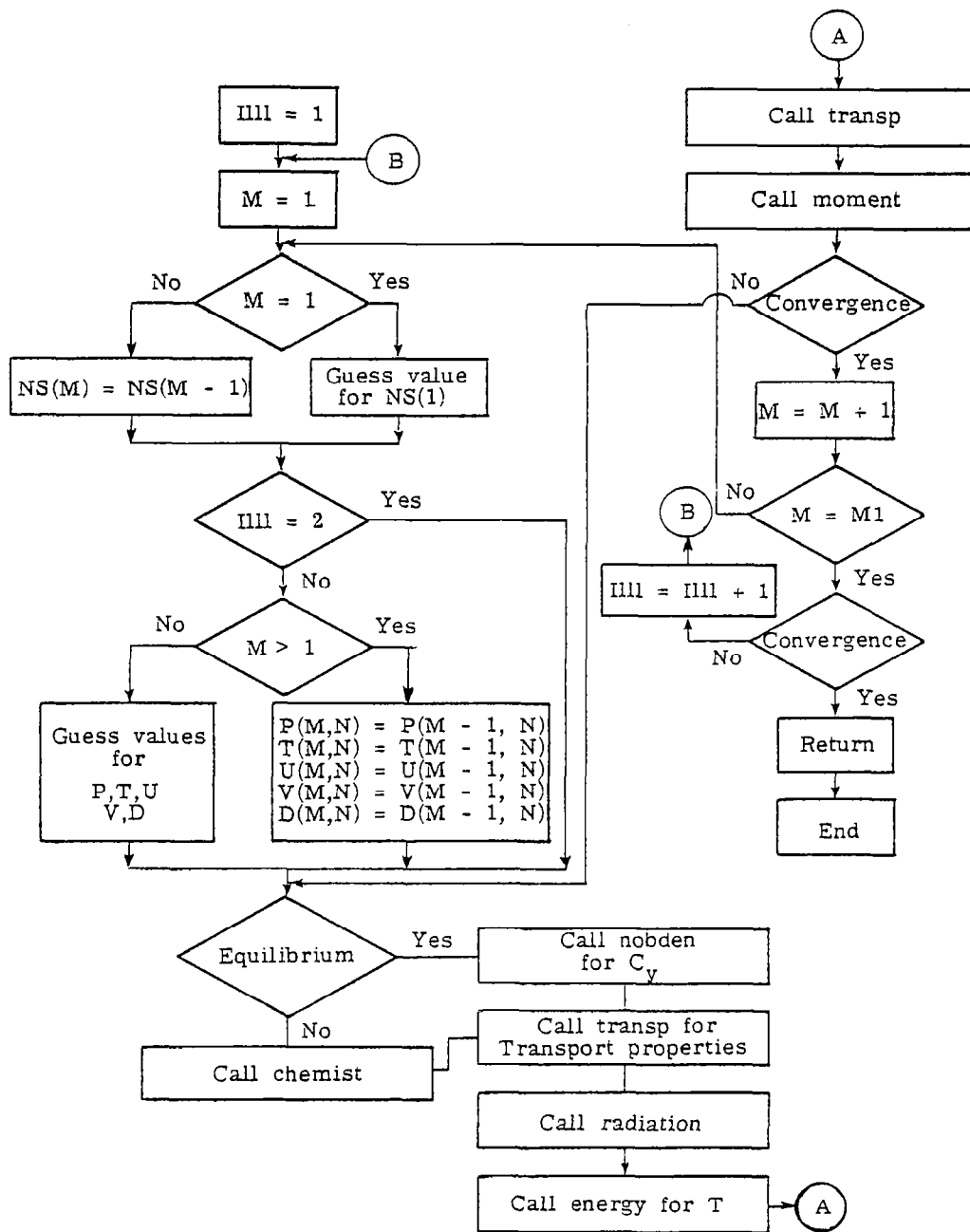
Figure A.3. Flow chart for subroutine SHOKLY for shock-layer solution.
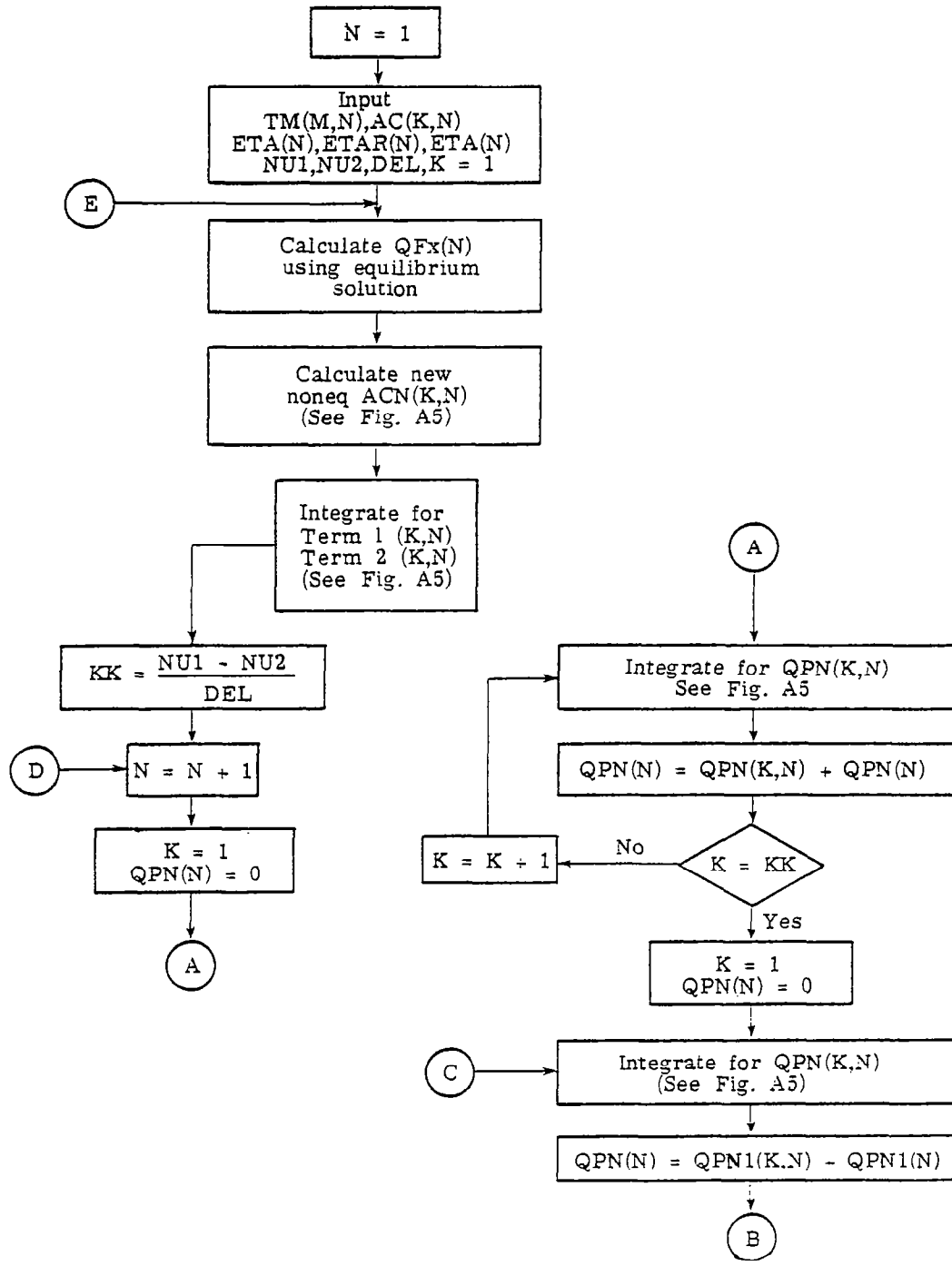
Figure A.4.   Flow chart for subroutine NRAD.
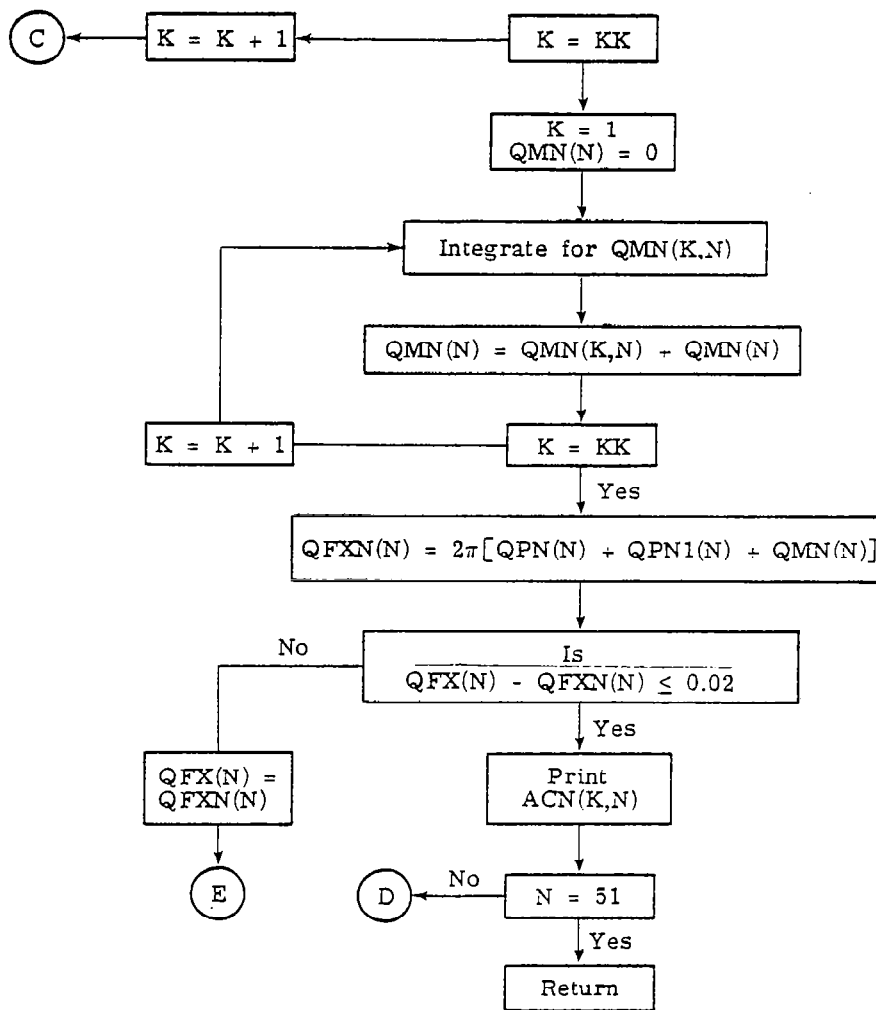
Figure A.4. (Concluded).

$$ACN(K,N) = AC(K,N) \left[1 + \eta + h\eta/2 (\nu_{1k}^4 - \nu_{2k}^4) \right] / \overline{\underline{X}}$$

$$\overline{\underline{X}} = \int_{\nu_{k1}}^{\nu_{k2}} \left\{ 2h\eta\nu^3/c^2 + \exp(-h\nu/kT) \right\} d\nu$$

$$X_1 = \int_{\nu_{k1}}^{\nu_{k2}} \nu^3 / [\exp(\nu)-1] d\nu$$

$$X_3 = \int_{\nu_{k1}}^{\nu_{k2}} \left\{ \nu^3 / [\exp(k\nu-1)] \right\} d\nu$$

$$X_2 = \eta \left[QFX(N+1) - QFX(N) \right] / 4\pi AC(K,N) \, DN$$

$$\text{Term 1 } (K,N) = (2h/c^2) \, (kT^4/h) \, X_1 - X_2$$

$$\text{Term 2 } (K,N) = (\epsilon h/c^2) \, X_3$$

$$QPN(K,N) = \int_0^N \text{Term 1 } (K,N) \, ACN(K,N) \, E_2 \left[\int_0^N \alpha_j(N')dN' \right] d\xi$$

$$QPN1(K,N) = \int_0^N \text{Term 2 } (K,N) \, E_3 \left[\int_0^N \alpha_j(N')dN' \right] d\xi$$

$$QMN(K,N) = \int_N^\xi \text{Term 1 } (K,N) \, ACN(K,N) \, E_2 \left[\int_N^\xi \alpha_j(N')dN' \right] d\xi$$

Figure A.5.   Definition of integrals used in NRAD.

160

REFERENCES

1. Anderson, J.D.: An Engineering Survey of Radiating Shock Layers. AIAA, Vol. 7, No. 9, Sept. 1969, pp. 1665-1675.

2. Page, W.A.: Aerodynamic Heating for Probe Vehicles Entering the Outer Planets. American Astronautical Society Paper No. AAS-71-144, June 1971.

3. Olstad, W.B.: Nongray Radiating Flow About Smooth Symmetric Bodies. AIAA, Vol. 9, No. 1, Jan. 1971, pp. 122-130.

4. Callis, L.B.: Coupled Nongray Radiating Flow About Long Blunt Bodies. AIAA, Vol. 9, No. 4, Apr. 1977, pp. 553-559.

5. Moss, J.N.: Reacting Viscous-Shock-Layer Solutions with Multi-component Diffusion and Mass Injection. NASA TR R-411, June 1974.

6. Sutton, K.: Fully Coupled Nongray Radiating Gas Flows with Ablation Product Effects About Planetary Entry Bodies. AIAA Paper No. 73-672, July 1973.

7. Sutton, K.; Moss, J.N.; Falanga, R.A.; and Olstad, W.B.: Outer Planet Entry Probes Aerothermal Environment - Status of Prediction Methodology. AIAA Paper No. 75-1148, Sept. 1975.

8. Tiwari, S.N.; and Szema, K.Y.: Effects of Precursor Heating on Radiative and Chemically Reacting Viscous Flow Around a Jovian Entry Body. NASA CR-3186, Oct. 1979.

9. McWhirter, R.W.P.: Spectral Intensities. Plasma Diagnostic Techniques, edited by R.H. Huddlestone and L.S. Leonard, Academic Press (N.Y.), 1966.

10. Jefferies, J.T.: Source Function in a Nonequilibrium Atmosphere: VII. The Interlocking Problem. Astrophys. J., Vol. 132, Nov. 1960, pp. 775-789.

11. Cottrell, T.L.; and Matheson, A.J.: Transition Probability in Molecular Encounters. Faraday Society (London) Transactions, Vol. 58, July 1962, pp. 2336-2341.

12. Tiwari, S.N.; and Cess, R.D.: The Influence of Vibrational Nonequilibrium upon Infrared Radiative Energy Transfer. J. Quant. Spectrosc. Radiat. Transfer, Vol. 11, Mar. 1971, pp. 237-248.

13. Tiwari, S.N.; and Subramanian, S.V.: Evaluation of Upwelling Infrared Radiance in a Nonhomogeneous Nonequilibrium Atmosphere. NASA CR-149090, Nov. 1976.

14. Horton, T.E.: The Importance of Nonequilibrium in Estimating Radiative Heat Transfer Through a Flow. AIAA Paper No. 76-170, Jan. 1976.

15. Wilson, K.H.: RATRAP - A Radiation Transport Code 6-77-67-12. Lockheed Missiles and Space Co., Mar. 14, 1967.

16. Thomas, M.: The Spectral Linear Absorption Coefficient of Gases - Computer Program SPECS (H189). DAC-59135, Missile & Space Syst. Div., Douglas Aircraft Co., Inc., Dec. 1966. (Revised May 1967).

17. Nicolet, W.E.: User's Manual for the Generalized Radiation Transfer Code (RAD/EQUIL). Aerotherm Report No. UM-69-9, Aerotherm Corp. (Mountain View, Calif.), 1969; also, User's Manual for RAD/EQUIL/1973, A General Purpose Radiation Transport Program, NASA CR-132470, Nov. 1973.

18. Zoby, E.V.; Sutton, K.; Olstad, W.B.; and Moss, J.N.: An Approximate Inviscid Radiation Flow Field Analysis of Outer Planet Entry Probes. AIAA Paper No. 78-189, Jan. 1978.

19. Tiwari, S.N.; and Subramanian, S.V.: Significance of Radiation
    Models in Investigating the Flow Phenomena Around a Jovian
    Entry Body. NASA CR-158972, Jan 1978. AIAA Paper No. 78-188,
    Jan. 1978.

20. Vincenti, W.G.; and Kruger, C.H.: Introduction to Physical Gas
    Dynamics. John Wiley and Sons (N.Y.), 1965.

21. Sparrow, E.M.; and Cess, R.D.: Radiation Heat Transfer (Augumented
    Edition). Hemisphere Publishing Corporation, McGraw-Hill Book
    Co. (N.Y.), 1978.

22. Penner, S.S.; and Olfe, D.B.: Radiation and Reentry. Academic
    Press (N.Y.), 1968.

23. Tauber, M.E.; and Wakefield, R.E.: Heating Environment and
    Protection During Jupiter Entry. J. Spacecrafts and Rockets,
    Vol. 8, 1971., pp. 630-636.

24. Sutton, K.: Coupled Nongrey Radiating Flow About Ablating
    Planetary Entry Bodies. AIAA, Vol. 12, No. 8, Aug. 1974,
    pp. 1099-1105.

25. Sutton, K.: Radiative Heating About Outer Planetary Entry Probes.
    AIAA Paper No. 75-183, Jan. 1975.

26. Sutton, K.; Jones, J.J.; and Powell, R.W.: Effects of Probe
    Configuration on Radiative Heating During Jovian Entry. AIAA
    Paper No. 76-471, July 1976.

27. Walberg, G.D.; Jones, J.J.; Olstad, W.B.; Sutton, K.; Moss, J.N.;
    and Powell, R.W.: Mass Loss Shape Change and Real-Gas Aero-
    dynamic Effects on a Jovian Atmospheric Probe. Acta Astro-
    nautica, Vol. 4, May 1977, pp. 555-575.

28. Hughes, W.F.; and Gaylord, E.W.: Basic Equations of Engineering
    Science, Schaum Publishing Company (N.Y.), 1964.

29. Sutton, K.: Characteristics of Coupled Nongray Radiating Gas Flows
    with Ablation Product Effects About Blunt Bodies During Planetary

Entries. Ph.D. Thesis, North Carolina State Univ. at Raleigh, 1973. (Available as NASA TM X-72078.)

30. Moss, J.N.: Radiative Viscous-Shock-Layer Solutions with Coupled Ablation Injection. AIAA, Vol. 14, No. 9, Sept. 1976, pp. 1311-1316.

31. Blottner, F.G.: Finite Difference Methods of Solution of the Boundary-Layer Equation. AIAA, Vol. 8, No. 2, Feb. 1970, pp. 193-205.

32. Davis, R.T.: Numerical Solution of the Hypersonic Viscous Shock-Layer Equations. AIAA, Vol. 8, No. 5, May 1970, pp. 843-851.

33. Zoby, E.V.; Gnoffo, P.A.; and Graves, R.A.: Correlations for Determining Thermodynamic Properties of Hydrogen-Helium Gas Mixtures at Temperatures from 7,000 to 35,000 K. NASA TN D-8262, Aug. 1976.

34. Sutton, K.; Jones, J.J.; and Powell, R.W.: Effects of Atmospheric Structure on Radiative Heating for Jupiter Entry Probe. AIAA Paper No. 78-185, Jan. 1978.

35. Szema, K.Y.: Effect of Precursor Heating on Radiating and Chemically Reaching Viscous Flow Around a Jovian Entry Body. Ph.D. Dissertation, Old Dominion Univ. (Norfolk, Va.), Nov. 1979; also NASA CR-3186, Oct. 1979.

36. Moss, J.N.; Anderson, E.C.; and Boltz, C.W.: Viscous-Shock-Layer Solutions with Radiation and Ablation Injection for Jovian Entry. AIAA Paper No. 75-671, May 1975.

37. Moss, J.N.; Anderson, E.C.; and Boltz, C.W.: Aerothermal Environment for Jovian Entry Probes. AIAA Paper No. 76-469, July 1976.

38. Sutton, K.; and Moss, J.N.: Radiation Absorption by C_2 Band Systems for the Jupiter Entry Conditions. AIAA Paper No. 76-0033, Jan. 1979.

39. Moss, J.N.: A Study of the Aerothermal Entry Environment for the Galileo Probe. AIAA Paper No. 79-1081, June 1979.

40. Kenneth, H.; and Strack, S.L.: Stagnation Point Radiative Heat Transfer. Amer. Rocket Soc. J., Vol. 31, No. 3, 1961, pp. 370-372.

41. Hoshizaki, H.; and Lasher, L.E.: Convective and Radiative Heat Transfer to an Ablating Body. AIAA, Vol. 6, No. 8, Aug. 1968, pp. 1441-1449.

42. Chien, Kuei-Yuan: Application of the S_n Method of Spherically Symmetric Radiative-Transfer Problems. AIAA Paper No. 71-466, Apr. 1971.

43. Wilson, K.H.: Evaluation of One-Dimensional Approximations for Radiative Transport in Blunt Body Shock Layers. NASA-CR-1990, Mar. 1972.

44. Pai, S.I.: Radiation Gas Dynamics. Springer-Verlag (N.Y.), 1966.

45. Kulander, J.L.: Curves of Growth for Nonequilibrium Gases. J. Quant. Spectrosc. Radiat. Transfer, Vol. 8, June 1968, pp. 1319-1340.

46. Tiwari, S.N.; and Subramanian, S.V.: Nonequilibrium Radiative Heating of a Jovian Entry Body. AIAA Paper No. 79-0035, Jan. 1979; also in Progress in Astronautics and Aeronautics: Entry Heating and Thermal Protection, Vol. 69, edited by Walter B. Olstad, AIAA (N.Y.), 1980, pp. 83-103.

47. Tiwari, S.N.; and Subramanian, S.V.: Influence of Nonequilibrium Radiation on Heating of an Ablating Jovian Entry Probe. AIAA Paper No. 80-0356, Jan. 1980.

48. Armstrong, B.H.; Johnston, R.R.; and Kelly, P.S.: Opacity of High-Temperature Air. AFWL-TR 65-17, U.S. Air Force, June 1965. (Available from DTIC as AD 618399.)

49. Nicolet, W.E.: Advanced Methods for Calculating Radiation Transport in Ablation Product Contaminated Boundary Layers. NASA CR-1656, Sept. 1970.

50. Nicolet, W.E.: Rapid Methods for Calculating Radiation Transport in the Entry Environment. NASA CR-2528, April 1975.

51. Patch, R.W.; Shackleford, W.L.; and Penner, S.S.: Approximate Spectral Absorption Coefficient Calculations for Electronic Band Systems Belonging to Diatomic Molecules. J. Quant. Spectrosc. Radiat. Transfer, Vol. 2, July 1962, pp. 263-271.

52. Sutton, K.; Moss, J.N.; and Anderson, E.C.: Radiation Absorption by the C_2 Band Systems for the Jupiter Entry Conditions. AIAA Paper No. 79-0033, Jan. 1979.

53. Heitler, W.: The Quantum Theory of Radiation (Third Edition), Oxford Univ. Press (London), 1954.

54. Goody, R.M.: Atmospheric Radiation I, Theoretical Basis. Oxford Univ. Press (London), 1964.

55. Gaydon, A.G.: Dissociation Energies. Chapman and Hall Ltd. (London), 1953.

56. Cooper, D.M.; and Nicholls, R.W.: Measurements of the Electronic Transition Moments of C_2 Band Systems. J. Quant. Spectrosc. Radiat. Transfer, Vol. 15, Feb. 1975, pp. 139-150.

57. Schadee, A.: The Relation Between the Electronic Oscillator Strength and the Wavelength for Diatomic Molecules. J. Quant. Spectrosc. Radiat. Transfer, Vol. 7, Feb. 1967, pp. 169-183.

58. Herzberg, G.: Atomic Spectra and Atomic Structure. Dover Publications (N.Y.), 1944.

59. Massey, M.S.W.; and Burhop, E.H.S.: Electronic and Ionic Impact Phenomena, Oxford Univ. Press (London), 1956.

60. Schwartz, R.N.; Slawsky, Z.I.; and Herzfeld, K.F.: Calculation of Vibrational Relaxation Times in Gases. J. Chem. Phys., Vol. 20, No. 10, Oct. 1952.

61. Spitzer, L.: Physics of Fully Ionized Gases. John Wiley and Sons (N.Y.), 1962.

62. McBridge, B.J.; Heimel, S.; Ehlers, J.G.; and Gordon, S.: Thermo-
    dynamic Properties to 6000 K for 210 Substances Involving the
    First 18 Elements. NASA Report SP-3001, 1963.

63. Babu, S.G.: Approximate Thermochemical Tables for Some C-H and
    C-H-O Species. NASA CR-2187, Mar. 1973.

64. Wilke, C.R.: A Viscosity Equation for Gas Mixtures. J. Chem.
    Phys., Vol. 18, No. 4, April 1950, pp. 517-519.

65. Hall, N.A.: Thermodynamics of Fluid Flow. Prentice Hall, Inc.
    (N.J.), 1957.

66. Esch, D.D.; Pike, R.W.; Engle, C.D.; Farmer, R.C.; and Balhoff,
    J.F.: Stagnation Region Heating of a Phenolic Nylon Ablator
    During Return from Planetary Mission. NASA CR-112026, Sept.
    1971.

1. Report No. NASA CR-3432	2. Government Accession No.	3. Recipient's Catalog No.
4. Title and Subtitle INFLUENCE OF NONEQUILIBRIUM RADIATION AND SHAPE CHANGE ON AEROTHERMAL ENVIRONMENT OF A JOVIAN ENTRY BODY		5. Report Date May 1981
		6. Performing Organization Code
7. Author(s) S. N. Tiwari and S. V. Subramanian		8. Performing Organization Report No.
		10. Work Unit No.
9. Performing Organization Name and Address Old Dominion University Research Foundation P.O. Box 6369 Norfolk, VA 23508		11. Contract or Grant No. NSG-1500
		13. Type of Report and Period Covered Contractor Report 8/1/79 – 2/29/80
12. Sponsoring Agency Name and Address National Aeronautics and Space Administration Washington, DC 20546		
		14. Sponsoring Agency Code

15. Supplementary Notes

Langley Technical Monitor: Kenneth Sutton
Final Report

16. Abstract

The influence of nonequilibrium radiative energy transfer and the effect of probe configuration changes on the flow phenomena around a Jovian entry body is investigated. The radiating shock-layer flow is assumed to be axisymmetric, viscous, laminar and in chemical equilibrium. The radiative transfer equations are derived under nonequilibrium conditions which include multilevel energy transitions. The equilibrium radiative transfer analysis is performed with an existing nongray radiation model which accounts for molecular band, atomic line, and continuum transitions. The nonequilibrium results are obtained with and without ablation injection in the shock layer. The nonequilibrium results are found to be greatly influenced by the temperature distribution in the shock layer. In the absence of ablative products, the convective and radiative heating to the entry body are reduced significantly under nonequilibrium conditions. The influence of nonequilibrium is found to be greater at higher entry altitudes. With coupled ablation and carbon phenolic injection, 16 chemical species are used in the ablation layer for radiation absorption. Equilibrium and nonequilibrium results are compared under peak heating conditions. For the study of the probe shape change effects, the initial body shapes considered are 45-degree sphere cone, 35-degree hyperboloid, and 45-degree ellipsoid. In all three cases, the results indicate that the shock-layer flow field and heat transfer to the body are influenced significantly by the probe shape change. The effect of shape change on radiative heating of the afterbodies is found to be considerably larger for the sphere cone and ellipsoid than for the hyperboloid.

17. Key Words (Suggested by Author(s)) Radiating shock-layer flow Heating of entry bodies Nonequilibrium radiative heating Nonequilibrium radiation with ablation	18. Distribution Statement Unclassified - Unlimited Subject Category 34	
19. Security Classif. (of this report) Unclassified	20. Security Classif. (of this page) Unclassified	21. No. of Pages 173

22. Price*
A08